Study on Heat and Mass Transfer Enhancement for Desiccant Dehumidification System

インドリ，ヤニンクシ

https://doi.org/10.15017/2534481

出版情報：Kyushu University, 2019, 博士（工学），課程博士
バージョン：
権利関係：

Study on Heat and Mass Transfer Enhancement for Desiccant Dehumidification System

Indri Yaningsih

May 2019

Department of Energy and Environmental Engineering
Interdisciplinary Graduate School of Engineering Sciences

KYUSHU UNIVERSITY
JAPAN

Study on Heat and Mass Transfer Enhancement for Desiccant Dehumidification System

A THESIS SUBMITTED IN PARTIAL FULFILLMENT OF THE REQUIREMENTS FOR THE AWARD OF THE DEGREE OF

DOCTOR OF ENGINEERING (Dr. Eng.)

By

Indri Yaningsih

May 2019

Supervisor
Prof. Takahiko Miyazaki

Department of Energy and Environmental Engineering
Interdisciplinary Graduate School of Engineering Sciences

KYUSHU UNIVERSITY

JAPAN

DECLARATION

I hereby declare that the work, which is being presented in the thesis entitled *"***Study on Heat and Mass Transfer Enhancement for Desiccant Dehumidification System***"* submitted in partial fulfillment of the requirements for the award of the degree of Doctor of Engineering (Dr. Eng.), Interdisciplinary Graduate School of Engineering Sciences, Kyushu University, Japan is an authentic record of my own research work.

The research work presented in the thesis has not been submitted by me for the award of any other degree in this or any other university.

Indri Yaningsih

May 2019

CONTENTS

Appendix A. Visualization and Analysis of Adsorption Isotherm and Kinetics by using Digital Image Processing

SUMMARY

Controlling the temperature and humidity is essential to achieve a comfortable space for occupants. Adjusting the temperature and humidity are corresponding to handle the latent and sensible heat, respectively. Considering the energy and environmental issues, one of the most challenging technology is called desiccant dehumidification system since it has high potency to increase the energy utilization efficiency by employing renewable energy and waste heat. However, heat and mass transfer inside the dehumidification system are small which leads to low performance of the system.

Recently, there are so many considerable efforts have been made to improve the performance of the desiccant dehumidification system through experimental and numerical study. Most research is concerning in the desiccant heat exchanger where the heat and mass transfer occurs between the adsorbent and adsorbate. The key driving force of enhancing the heat and mass transfer of the system is that the desiccant heat exchanger should provide a large contact between the adsorbent and adsorbate to provide good heat and mass transfer. However, none of these two combinations yet to be perfectly resolved. Therefore, from this motivation, the current study is focused on the research on heat and mass transfer enhancement of the desiccant dehumidification system. This study also focused on the low desorption temperature utilization by employing the desorption temperature system less than 70 ºC. There are two main parts of the study: (1) the enhancement of the heat transfer by conducting an experimental study on enhanced heat transfer of the direct contact heat exchanger by using passive heat transfer, (2) the enhancement of the mass transfer by conducting the experimental study on adsorption characterization including adsorption isotherm and adsorption kinetics of the adsorbent material by using volumetric methods.

Based on the descriptions, the main objectives of the present study are: (1) to investigate experimentally heat and mass transfer characteristics of the desiccant dehumidification system, (2) to evaluate performance of the desiccant dehumidification system, (3) to estimate heat transfer augmentation in the air and air heat exchanger by using passive heat transfer enhancement method, (4) to provide a new method of the adsorption isotherm and kinetics of the desiccant material by using a digital image analyzing method.

Heat and mass transfer characteristics of the desiccant dehumidification system were evaluated in terms of Nusselt number (*Nu*) for heat transfer and Sherwood number (*Sh*) for mass transfer. As the beginning of the study, the validation of the heat and mass balance of the desiccant dehumidification system was experimentally investigated to ensure that the experimental methods are reliable to conduct a further experiment. The experimental study was conducted under various adsorption temperature and switching time. The evaluation was done by comparing the heat and mass balance between the adsorption and desorption processes. Within the parameter studied the discrepancy of the heat and mass balance of the system was less than 8%, which proves the reliability of the system.

The most challenging problem for analyzing the heat and mass transfer characteristics inside the desiccant dehumidification system is determining the properties of the interface area between the desiccant material and process air flow where the heat and moisture transport takes place. To overcome this problem, an approached by using the thermal and mass resistance concept is provided. By using the solution of the equation of heat and mass transfer, the heat transfer and mass transfer coefficients can be predicted. Under the parameter studied, the highest average *Nu* was 38.65 for T_{ads} of 20 ºC, t_c of 120 min. For the *Sh*, the highest average value was 36.39 for T_{ads} of 20 ºC, t_c of 120 min. Empirical correlations for predicting heat and mass transfer characteristics of the desiccant dehumidification system were also developed. The empirical correlations in terms of *Nu* and *Sh* are in good agreement with measurement, with a deviation of less than 10% for each. The calculation of adsorption rate is also done, which represents the adsorption behavior in the system. It is found that the highest adsorption rate was 0.00809 kg/kg.s for T_{ads} of 20 ºC, t_c of 210 min.

For heat and mass transfer enhancement consideration, an evaluation of the performance of desiccant dehumidification system is also given. The performance evaluation was analyzed in terms of dehumidification ability, latent heat ratio, and latent heat effectiveness. The highest latent heat ratio was found in the value of 0.61 at the desorption temperature of 35 ºC, while the highest latent effectiveness was obtained at a desorption temperature of 65 ºC. Referring to the results, an appropriate desorption temperature to obtain proper performance was found at 55 ºC. Since the performance of the system has a potency to be improved, the heat transfer enhancement for the desiccant heat exchanger is presented in this study. Enhanced heat transfer was done by employing passive heat transfer methods in the form of delta wing/winglet vortex generators. The presence of the delta wing/winglet vortex generators could enhance the heat transfer by 177% as compared to those without vortex generator. Finally, considering the importance of the desiccant material characteristic, the development of the methods for calculating adsorption isotherm and adsorption rate is provided. A new method by using an image processing algorithm is utilized to calculate the liquid level changes, which represent the amount of vapor adsorbed. Algorithm for image analysis could semantically segment the adsorption process by creating images which represented the dataset for water level changes inside the evaporator. The results show that the proposed system and method has the ability to determine the water level changes and provide dataset for analyzing the kinetic rate of the adsorption process.

Finally, based on the results of the present study, it is possible to improve the performance of the desiccant dehumidification system. Providing a large area by using passive heat transfer methods could improve the heat transfer, which corresponds to the increase of the performance of the system.

LIST OF FIGURES

Chapter 1

Chapter 2

Chapter 3

Chapter 4

Chapter 5

Appendix A

LIST OF TABLES

Chapter 2

Chapter 3

Chapter 5

Appendix A

CHAPTER 1

Chapter 1

INTRODUCTION

Providing thermal comfort involves the efforts on how to control proper parameters, including humidity, temperature, and quality of the air such as hygiene, air-speed and the pressure difference between the conditioned space with the surroundings. Combining these parameters, indeed, becomes high challenges for the air conditioning engineers. Nowadays, the development of the air conditioning system moving towards a high-performance system with a low energy requirement. Because the air conditioner consumes a huge amount of energy, especially in a hot and humid area (Kinsara, A. A., et al., 1995). However, when the air conditioning load can be handled separately, the energy consumption for providing thermal comfort can be reduced. The desiccant system in the form of solid or liquid can remove the water vapor, which offers the advantage of handling the latent load. When the supply air in contact with the desiccant material, because of the differences of the pressure between the surface of desiccant material and the process air, the moisture from the air can be transferred so that the excess moisture can be reduced. The desiccant system could keep the water vapor until the partial pressure of the desiccant material and the surrounding air reached equilibrium.

From these advantages, the desiccant material offers huge potential as an air conditioning system. However, when it is compared to the traditional vapor compression system, the performance of the desiccant system still could not compete. Inside the dehumidification system, there is a couple of heat and mass transfer processes which is determined the performance of the system (Sun et al., 2018; Shamin et al., 2019). In case of the solid desiccant material, the heat and mass transfer between the surface of the desiccant material and air stream is very low, so that is not sufficient for achieving the dehumidification load (Zhang, L., 2014). Therefore, this study provides an experimental and theoretical for heat and mass transfer enhancement of desiccant dehumidification system which is expected for achieving a high-performance of dehumidifier system.

1.1 Literature Review

1.1.1. Heat and Mass Transfer of the Desiccant Dehumidification System

Isetti et al. (1997) provided the performance of the air handling unit by using hydrophobic membrane vapor contactor. The direct contact heat exchanger for the liquid desiccant flow and hollow fiber membrane is presented in Fig. 1.1.

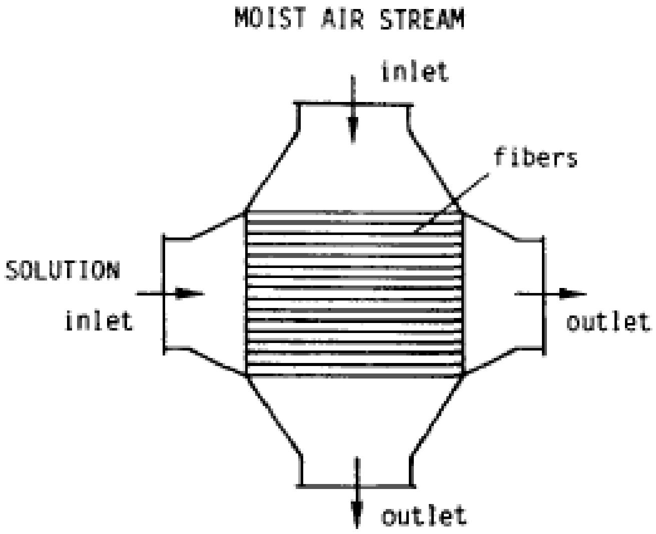

Figure 1.1. Membrane module for liquid desiccant and air stream (Isetti et al., 1997).

The membrane module with direct contact design was developed by considering some factors; (1) friction loss was small because the low velocity of the air stream; (2) contact area remains constant, however; (3) it provides a high mass-transfer surface per unit volume. Two different materials (PE and PTFE) were employed to evaluate the performance of the system. The performance of the system was assessed by considering mass transfer inside the module. Figure 1.2 depicts a schematic diagram of the concentration profiles in the membrane interface.

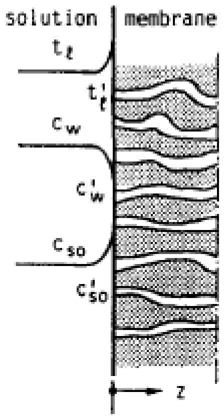

Figure 1.2. Temperature and water-solute concentration profiles (Isetti, et al., 1997).

The vapor mass transfer was calculated by considering the vapor mass transfer through the membrane and vapor mass transfer in the gas phase. They found that mass transfer of the system depends on the solution strength, vapor pressure in the air, mass transfer coefficient and temperature gradient along the membrane. They stated that there is a strong correlation between the heat and mass transfer to improve the performance. The heat transfer coefficient increments between the air side and liquid side of the membrane will boost the performance of the system. Their results also revealed that the system could reduce energy consumption because the regeneration temperature was only 310-330K.

Zhang and Jiang (1999) modeled heat and mass transfer of a membrane-based energy ventilator for dehumidification through the finite difference simulation. Porous hydrophilic membrane core was used as the membrane with the permeability of 2.5×10^{-5} kg/m^2s. The temperature and humidity fields along the unit were investigated. Figure 1.3 shows the design of cross-flow membrane-based energy ventilator. The design of the heat exchanger was the direct contact heat exchanger which consist of two streams. Feed stream was the fresh air intake while the sweep stream was exhaust stream to the outside.

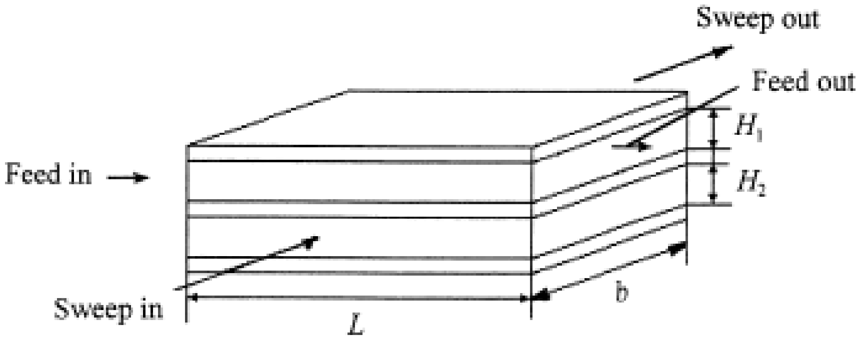

Figure 1.3. The air-to-air heat exchanger of membrane-based energy ventilator (Zhang and Jiang, 1999).

The calculation of heat and mass transfer was based on the Nusselt number (*Nu*) for heat transfer and Sherwood number (*Sh*) for mass transfer. Their results show that, for the mass transfer in the membrane area, the most effective zone was near the inlet which shows the high differences in the humidity. Additionally, for the heat transfer, the trends were also similar to the mass transfer. The reason behind the problem was due to the flow arrangement which was the counter flow arrangement. The distribution of the heat and moisture exchange was not effective due to the permeability of the membrane was only high near the inlet.

Zhang and Liu (2002) provided a performance comparison between the desiccant wheels for air dehumidification and enthalpy recovery. The desiccant wheel was made from composite material. The influence of the rotary speed, the number of the heat transfer unit, and the specific area on the performance of the system for both situations were investigated. The model was developed based on two-dimensional, dual-diffusion transient heat and mass transfer. The heat and mass resistance in the axial and thickness directions of the solid were considered. The performance indexes of the system were investigated in the form of sensible effectiveness, latent effectiveness, dehumidification effectiveness, and specific dehumidification power. The calculation of the heat and mass transfer inside the system was provided and described clearly. Their results show that the better performance of the enthalpy recovery can be achieved when the slope of the water content towards the humidity ratio is higher. While for the air dehumidification, the high performance of the system could be achieved if the relative humidity is higher. Also, for enthalpy recovery, the temperature and humidity field were found more homogeneous as compared to the desiccant dehumidification wheel.

Zhang and Wang (2003) conducted a simulation study on the heat and mass transfer in a honeycombed rotary desiccant dehumidifier. A one-dimensional theoretical model was developed to solve the equation of heat and mass transfer within the system. Validation was done by comparing using a real desiccant wheel. The effect of the regeneration and process air velocity inlet were investigated to evaluate the performance of the system. The profile temperature and humidity ratio were presented based on the simulation results. For the mass transfer which corresponds to the humidity exchange, the results show that the behavior between the regeneration and dehumidification process towards the humidity ratio and temperature was different. For the regeneration process, the monotone increasing function of the air humidity ratio was shown along the channel, however, for the dehumidification process, it shows a monotone decreasing. For heat transfer, because the increase of the temperature in regeneration process was slow, and the vapor pressure was also low, therefore the water content reduces. However, the reverse situation existed in the dehumidification process. The importance result from their research is the high effectiveness of the dehumidification could be achieved if the regeneration air velocity is high.

Jeong et al. (2011) investigated numerically the performance of the desiccant dehumidification systems driven by a low-grade heat source. The study was aimed to determine the minimum heat source temperature to drive the system. Four different systems namely, conventional dehumidification system, dehumidification system with precooler, double-stage-type system, and batch-type system with an internal heat exchanger could be driven by the lowest heated air temperature. Based on the simulation results, a batch-type system with an internal heat exchanger offers the highest heat transfer rate among the others. Figure 1.4 shows the schematic diagram flow of the dehumidification system with internal heat exchanger.

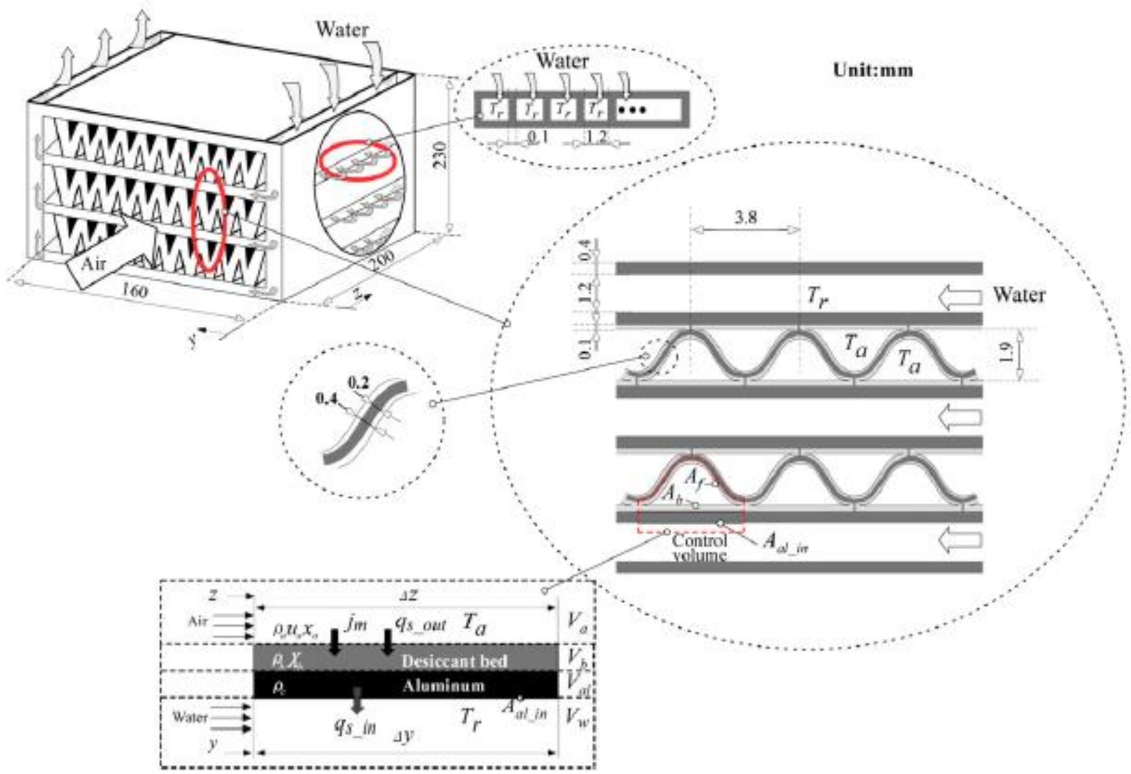

Figure 1.4. Schematic diagram of the batch-type dehumidification system with an internal heat exchanger (Jeong et al., 2011).

The high heat transfer rate is revealed due to the high thermal capacity of the aluminum part. The internal heat exchanger was made of aluminum material which has the density and specific heat of 2700 kg/m^3 and 900 J/kg.K, respectively. Moreover, under the same switching time, a batch-type system with an internal heat exchanger almost provides constant switching time because of the thermal capacity of the water flow rate. They found that the lowest regeneration temperature of 33^{o}C could drive a batch-type system with an internal heat exchanger.

Kubota et al. (2017) investigated the performance of the cross-flow heat exchange type adsorbed for controlling the humidity. The heat exchanger was coated with the aluminophosphate (AIPO) zeolite for improving the dehumidification performance. Figure 1.5 shows the schematic diagram of the cross-flow heat exchanger of the experimental apparatus.

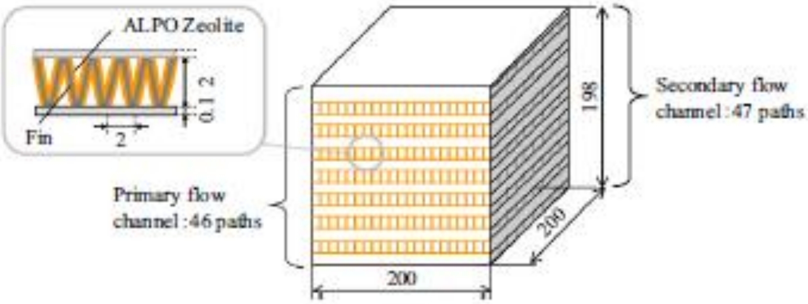

Figure 1.5. Schematic diagram of the cross-flow heat exchanger type absorber (Kubota et al., 2017).

The effect of the regeneration temperature and cooling air velocity was investigated to evaluate the performance of the system. The results show with the increase of the regeneration temperature; the dehumidified water was decreased. Increasing the cooling air velocity will increase the adsorption ratio. Another design of the coated heat exchanger was also investigated by Erkek et al., 2018. Silica gel and aluminum fumarate were employed as the desiccant coating materials. Figure 1.6 shows the design of the desiccant-coated heat exchanger.

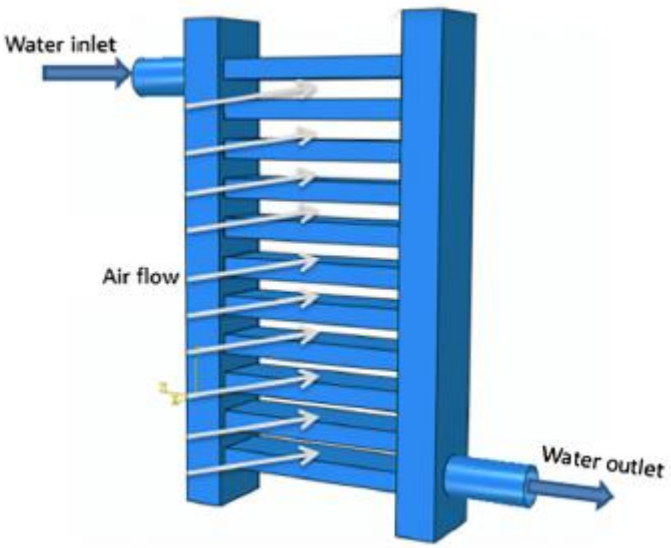

Figure 1.6. Schematic diagram of desiccant coated heat exchanger (Erkek et al., 2018).

The performance of the system was evaluated based on the humidity ratio, heat, and mass transfer coefficient, dehumidification, and regeneration capacity. Their found that the silica gel offers 8% higher dehumidification capacity and 11% regeneration capacity as compared to the aluminum fumarate.

1.1.2. Heat Transfer Enhancement by Using Delta Wing/ Winglets Vortex Generators

Vortex generators (VGs) have received extensive attention by researchers (Torii and Yanagihara, 1989; Yanagihara and Torii, 1992; Fiebig et al., 1994; Jacobi and Shah, 1995; Fiebig, 1998) as devices for obtaining high thermal performance by enhancing the heat-transfer coefficients of a tube heat exchanger. VGs are also regarded as potential heat-transfer augmentation devices because they create vortices that lead to high heat-transfer rates (Fiebig, 1998). VGs are used to induce secondary flow, which disturbs or cuts off the thermal boundary layer developed along the wall and removes heat from the wall to the core of the flow by means of large-scale turbulence (Ferrouillat et al, 2006). VGs that form longitudinal vortices are extremely attractive because they experience only a small pressure drop penalty. These longitudinal vortices can be generated by using wing or winglet type VGs, which create flow separation at the leading edge of the wing (Biswas et al., 2012). Generally, wing/winglet type VGs function like a fin and are fabricated by punching out or mounting onto a strip/base fin. Considerable improvements in convective heat transfer using the wing/winglet VGs have been demonstrated. Wu and Tao (2012) conducted an experimental and numerical study on a rectangular channel fitted with a delta-winglet vortex generator. The attack angles were varied (15°, 30°, 45°, and 60°) to obtain an optimum heat-transfer profile for the channel. A large attack angle was found to exhibit a high heat-transfer rate, which was due to a disruption of the air flow in the lower channel by the transverse flow through the punched holes. Figure 1.7 shows the design of delta winglet pair on the tested plate. The highest heat transfer rate improvement was 34% as compared to the plate without delta winglet.

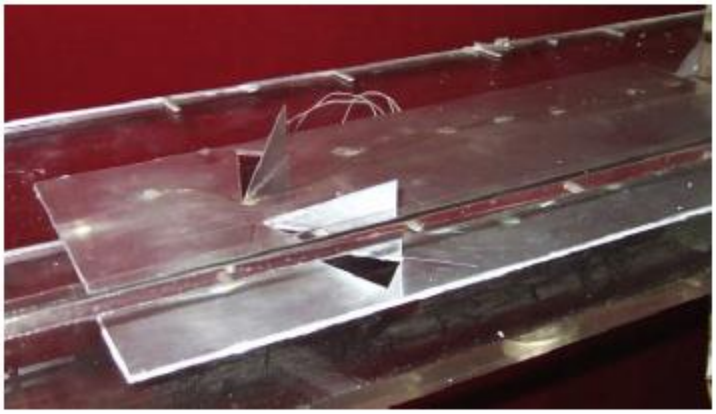

Figure 1.7. Delta winglet pairs on the tested plate (Wu and Tao, 2012).

He et al. (2013) also conducted a numerical study on heat-transfer augmentation by investigating the mechanism of the flow structure. Variation in the attack angle, row number, and placement of rectangular winglet pairs was discussed in detail. They found that by altering the position of the winglet, pressure drop could be reduced without decreasing heat transfer. Compared to the heat exchanger without the delta winglets, the heat transfer was improved up to 105.1%. Figure 1.8 shows the design of the delta winglet in the fin and tube heat exchanger.

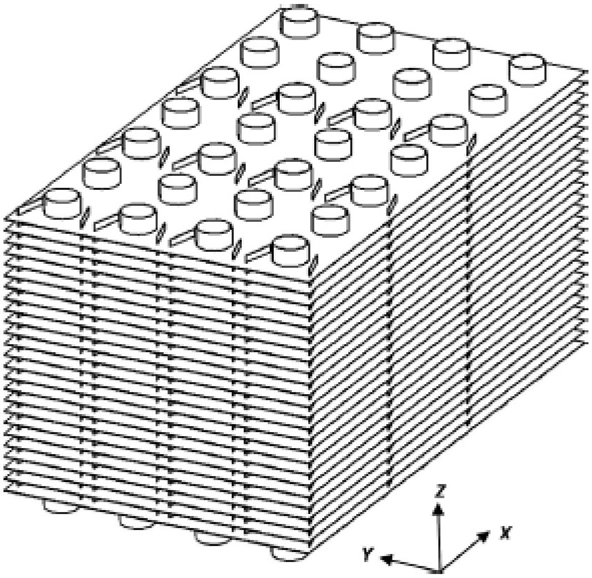

Figure 1.8. Schematic diagram of the delta winglet vortex generator in the fin and tube heat exchanger (He et al., 2013).

Gholami et al. (2014) numerically investigated the effect of variations in the profile of rectangular winglets (i.e., wavy-up and wavy-down) on the heat-transfer performance of a fin-and-tube heat exchanger and compared with that of a conventional rectangular channel without a winglet. The wavy-up and wavy-down rectangular winglets were found to exhibit better heat-transfer performance. Moreover, the effect of the wavy-up configuration was more significant than the wavy-down configuration. Figure 1.9 shows the design of the wavy rectangular winglet-type vortex generators.

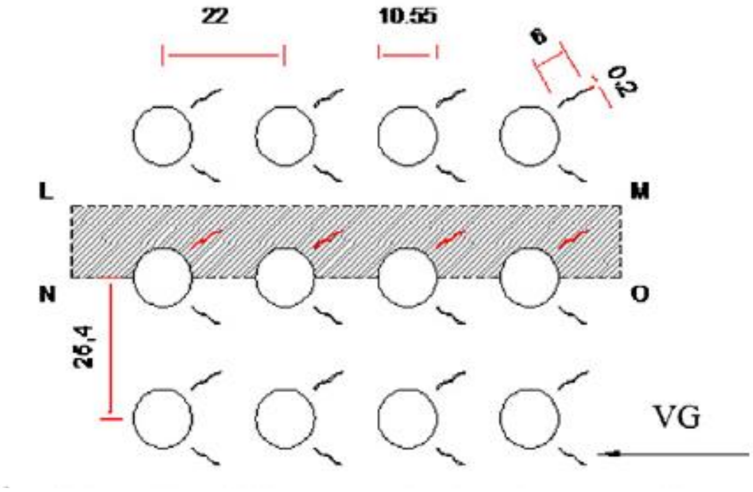

Figure 1.9. Schematic diagram of a 2D compact heat exchanger with wavy delta winglet (Gholami et al., 2014).

Khoshvaght-Aliabadi et al. (2015) experimentally studied the influence of various delta-winglet arrangements (one side cut with one delta-winglet, one side cut with two delta winglets, two sides cut with two delta winglets, and two sides cut with four delta winglets) on the heat-transfer augmentation of a tube and compared that to the performance of a plain tube. The results showed that a tube with delta winglets had better thermal performance than a plain tube and that the arrangements of two sides cut with four delta winglets outperformed all other arrangements.

A combined winglet pair (a rectangular wing and a trapezoidal wing) proposed as a novel longitudinal vortex generator was numerically investigated by Wang et al., 2015. Compared with a rectangular winglet pair, the combined winglet pair showed considerable improvement in heat transfer with a moderate pressure drop penalty. Abdollahi and Shams (2015) numerically studied the optimization parameters (shape and attack angle) of a winglet vortex generator. They showed that at low Reynolds number, attack angle modification did not significantly improve performance; in contrast, for a high Reynolds number, variation in the attack angle considerably influenced performance because the angle could increase drag. Moreover, among the different vortex generator shapes (traditional vortex generator, delta vortex generator, rectangular vortex generator, and trapezoidal vortex generator), the rectangular vortex generator was found to provide the best heat-transfer performance because it had a large facing flow area. The effect of a combined wavy-groove and delta-winglet vortex generator on the thermal performance of a solar air heater channel was experimentally investigated by Skullong et al., 2016. Experiments were conducted at a constant wing attack angle with three different wing porosity area ratios and four groove-wing distance to channel-height ratios. The different parametric combinations exhibited different behaviors in the thermal performance of the system. Sarangi and Mishra (2017) numerically examined the influence of the winglet position on the heat-transfer characteristics of a fin-and-tube heat exchanger. They found that an increase in the number of winglets enhanced the heat-transfer rate. In addition, the position of the delta winglet at the center of the tube showed more efficient heat transference than delta winglet in inlet and exit of heat exchanger.

1.2 Objectives

Several works on heat and mass transfer analysis of the desiccant dehumidification system have been carried out. The development of heat and mass transfer enhancement through the numerical and experimental study is also developed. However, there are scarce works on enhancement of desiccant dehumidification system by using passive heat transfer methods. Therefore, it is important for this study to provide the work on enhanced heat and mass transfer of the desiccant dehumidification system by using passive heat transfer. The main objectives of the present study are as follows:

1. To investigate experimentally heat and mass transfer characteristics of the desiccant dehumidification system in the term of Nusselt number (*Nu*) for heat transfer and Sherwood number (*Sh*) for mass transfer.

2. To estimate the performance of the desiccant dehumidification system in the term of dehumidification index, latent heat ratio and latent heat effectiveness.
3. To provide a design of the heat transfer enhancement of the desiccant heat exchanger by employing the passive heat transfer in the form of delta wing/ delta winglet vortex generators.
4. To provide a new method of the adsorption isotherm and kinetics of the desiccant material by using a digital image analyzing method.

1.3 Outline of the thesis

This thesis consists of six chapters. The following is a brief description of each chapter.

Chapter 1 describes work relating to the heat and mass transfer characteristics of the desiccant dehumidification system. Several works on heat and mass transfer enhancement of desiccant dehumidification system are provided and briefly described. Some important parameters which affected the performance of the heat and mass transfer inside the system are presented. The objectives of this study and thesis content are included.

Chapter 2 encompasses work on experimental description and validation on heat and mass balance of the desiccant dehumidification system. This chapter evaluates the potency of the desiccant dehumidification system by investigating the experimental study under various adsorption temperature and switching time. Experimental set up for conducting heat and mass transfer of the desiccant dehumidification system is provided. The potency of the system is evaluated by analyzing the relative humidity and humidity ratio changes during the adsorption and desorption processes. In addition, some parameters were employed to involve the proper parameter which could give a better performance overall the experiment. Heat and mass balance of the system is evaluated by comparing the adsorption and desorption process.

Chapter 3 involves research on heat and mass transfer characteristics of the desiccant dehumidification system. Nusselt number (Nu) and Sherwood number (Sh) are employed to express the heat and mass transfer characteristics, respectively. Heat and mass transfer of the system is evaluated under three different adsorption temperatures and four different switching times. Calculating the heat and mass transfer characteristics is done based on the thermal resistance analysis to simplify the calculation. The analogy between the *Nu* and *Sh* is used, which called Lewis number (*Le*), to calculate the mass transfer coefficient. Empirical correlation to predict the heat and mass transfer is provided.

Chapter 4 deals with the experimental study on the performance of the desiccant dehumidification system. To investigate the performance of the system under low-temperature operation, four different desorption temperatures (35ºC, 45ºC, 55ºC, and 65ºC) are employed. The performance of the system was investigated in terms of dehumidification index, latent heat ratio, and latent effectiveness. Based on the results, by considering the system as the dehumidifier, the appropriate desorption temperature to obtain proper performance was found at 55ºC.

Chapter 5 includes work on the heat transfer enhancement of desiccant dehumidification system, particularly on desiccant heat exchanger by using passive heat transfer method. Passive heat transfer method in the form of delta wing/ winglets is a promising technique to enhance the heat transfer within the heat exchanger by providing a large surface area which could improve the contact between the adsorbent and adsorbate. The evaluation of the enhanced heat transfer is done by comparing the heat exchanger with and without delta wing/ winglets vortex generators. Generally, improving heat transfer will also increase the friction factor inside the system. Evaluation of the friction factor which corresponds to the pressure drop is presented. Additionally, empirical correlations for predicting the heat transfer and friction factor characteristics are provided.

In the last chapter (Chapter 6), the general conclusions of this study are summarized. Based on the results of the work within this study, it is found that it is possible to enhance the heat and mass transfer of the desiccant dehumidification system to improve the performance. Heat and mass transfer are the main criteria when designing the desiccant dehumidification system to get a satisfying performance.

References

Abdollahi, A., Shams, M. Optimization of shape and angle of attack of winglet vortex generator in a rectangular channel for heat transfer enhancement. Appl. Therm. Eng. 2015, 81, 376-387.

Biswas, G., Chattopadhyay, H., Sinha, A, Augmentation of heat transfer by creation of streamwise longitudinal vortices using vortex generators, Heat Transfer Eng. 33 (2012) 406-424.

Erkek, T.U., Gungor, A., Fugmann, H., Morgestern, A., Bongs, C., Performance evaluation of a desiccant coated heat exchanger with two desiccant materials, Apll. Ther. Eng. 143 (2018) 701-710.

Ferrouillat, S., Tochon, P., Garnier, C., Peerhossaini, H., Intensification of heat transfer and mixing in multifunctional heat exchangers by artificially generated streamwise vorticity, Appl. Therm. Eng. 26 (2006) 1820–1829.

Fiebig, M, Vortices, generators, and heat transfer, Trans. IChemE. 76 (1998) 108-123.

Fiebig, M., Valencia, A., Mitra, N.K, Local heat transfer and flow losses in fin-and-tube heat exchangers with vortex generators: a comparison of round and flat tubes, Exp. Therm. Fluid Sci. 8 (1994) 35-45.

Gholami, A.A., Wahid, M.A., Mohammed, H.A., Heat transfer enhancement and pressure drop for fin-and-tube compact heat exchangers with wavy rectangular winglet-type vortex generators, Int. Commun. Heat Mass Transf. 33 (2014) 132-140.

He, Y., Chu, P., Tao, W., Zhang, Y., Xie, T., Analysis of heat transfer and pressure drop for fin-and-tube heat exchangers with rectangular winglet-type vortex generators, Appl. Therm. Eng. 61 (2013) 770-783.

Isetti, C., Nannei, E., Magrini, A., On the application of a membrane air-liquid contactor for air dehumidification, Energy and Buildings 25 (1997) 185-193.

Jacobi, A.M., Shah, R.K, Heat transfer surface enhancement through the use of longitudinal vortices: a review of recent progress, Exp. Therm. Fluid Sci. 11 (1995) 294-309.

Jeong, J., Yamaguchi, S., Saito, K., Kawai, S., Performance analysis of desiccant dehumidification systems driven by low-grade heat source, Int J Refrig. 34 (2011) 928-945.

Khoshvaght-Aliabadi, M., Sartipzadeh, O., Alizadeh, A., An experimental study on vortex-generator insert with different arrangements of delta-winglets, Energy 82 (2015) 629-639.

Kinsara, A.A., Elsayed, M. M., Al-Rabghi, O. M., Proposed energy-efficient air-conditioning system using liquid desiccant, Appl. Therm. Eng. 16 (10) (1996) 791-806.

Kubota, M., Hanaoka, N., Matsuda, H, Kodama, A., Dehumidification behavior of cross-flow heat exchanger type adsorber coated with aluminophosphate zeolite for desiccant humidity control system, Appl. Therm. Eng 122 (2017) 618-625.

Sarangi, S.K., Mishra, D.P., Effect of winglet location on heat transfer of a fin-and-tube heat exchanger, Appl. Therm. Eng. 116 (2017) 528-540.

Skullong, S., Promvonge, P., Thianpong, C., Pimsarn, M., Thermal performance in solar air heater channel with combined wavy-groove and perforated-delta wing vortex generators, Appl. Therm. Eng. 100 (2016) 611-620.

Shamim, J. A., Paul, S., Kitaoka, K., Hsu, W., Daiguji, H., Experimental evaluation of transient heat and mass transfer during regeneration in multilayer fixed-bed binder-free desiccant dehumidifier, Int. J. Heat Mass Transf., 128 (2019) 623-633.

Sun, X. Y., Dai, Y. J., Ge, T. S., Zhao, Y., Wang, R. Z., Experimental and comparison study on heat and moisture transfer characteristics of desiccant coated heat exchanger with variable structure sizes, Appl. Therm. Eng., 137 (2018) 32-46.

Torii, K., Yanagihara, J.I, The effect of longitudinal vortices on heat transfer of laminar boundary layers, JSME Int. J. 32 (1989) 395-402.

Wu, J.M., Tao, W.Q., Effect of longitudinal vortex generator on heat transfer in rectangular channels, Appl. Therm. Eng. 37 (2012) 67-72.

Wang, W., Bao, Y., Wang, Y., Numerical investigation of a finned-tube heat exchanger with novel longitudinal vortex generators, Appl. Therm. Eng. 86 (2015) 27-34.

Yanagihara, J.I, Torii, K, Enhancement of laminar boundary layer heat transfer by a vortex generator, JSME Int. J. 35 (1992) 400-405.

Zhang, L., Conjugate heat and mass transfer in heat mass exchanger ducts, Elsevier, UK, 2014.

Zhang, L. Z., Jiang, Y., Heat and mass transfer in a membrane-based energy recovery ventilator, Journal of Membrane Science 163 (1999) 29-38.

Zhang, L. Z, Niu, J.L., Performance comparisons of desiccant wheels for air dehumidification and enthalpy rcover, Appl. Therm. Eng. 22 (2002) 1347-1367.

Zhang, X. J., Dai., Y. J., Wang, R. Z., A simulation of heat and mass transfer in a honeycombed rotary desiccant dehumidifier, Appl. Therm. Eng. 23 (2003) 989-1003.

CHAPTER 2

Chapter 2

EXPERIMENTAL DESCRIPTION AND VALIDATION

This chapter highlights the experimental description and validation for investigating the heat and mass transfer of desiccant dehumidification system. The potency of the system as an air conditioner is provided. The dehumidification capacity represents it. The system consists of desiccant block units, dehumidification and regeneration air sources, air flow control valves, and a set of heat exchanger. Desiccant blocks are made of a hydrophilic polymer with honeycomb shaped. The present study is focused on heat and mass transfer characteristics to enhance the performance of the system. In this chapter, three different process air temperatures are investigated at 20 ^{o}C, 25 ^{o}C, and 35 ^{o}C under constant regeneration air temperature of 55 ^{o}C and inlet air velocity of 0.1 kg/s. For each process air temperature, four different switching time ratios are also introduced. The results revealed that the dehumidification capacity of the desiccant system has great potential as an air conditioning device. The current system has the highest dehumidification index of 4.7 g/kg. Moreover, the heat and mass transfer balance of the system show the discrepancy of less than 8%, and those the experimental methods are reliable to conduct a further experiment.

2.1 Introduction

Air conditioning to achieve the human thermal comfort is an essential role in human life, especially in humid and hot climates area. Traditional vapor-compression systems are a widely used method to accomplish this condition. However, this system is primarily driven by using a refrigerant as working fluids which has high potential on the ozone depletion layer. High-grade energy is also required. A significant amount of energy, that used to achieve this air, is mostly coming from conventional energy resources. Due to some drawbacks of the vapor-compression system, alternative technology should be proposed.

A desiccant dehumidification system has been proposed as an alternative technology and practical solution to provide the air conditioning due to the main merits of low initial energy consumption, no required refrigerant, and low-cost air conditioning system. The desiccant dehumidification system could provide the same effect with traditional vapor-compression by controlling the humidity using its own temperature. This technology also reduces the energy consumption largely by employing some waste heat from the industrial processes or power plant and utilizing renewable energy sources. If the desiccant dehumidification system is appropriately applied, it could save more energy than the traditional system.

Nowadays, the development of desiccant dehumidification technology has been paid considerable attention from researchers. Majumdar and Worek (1989) studied desiccant cooling system by using advanced desiccant matrices. The parameters related to indoor and outdoor conditions were numerically studied to evaluate the performance of the system. They proposed a detail mathematical model for calculating the moisture diffusion and heat conduction of the desiccant dehumidifier. They found that regeneration and indoor air temperature and outdoor humidity ratio were significantly affected by the performance of the system. Dhar and Singh (2001) investigated a hybrid air-conditioning system using a solid desiccant. They investigated the performance of the hybrid air-conditioning system by considering the energy consumption and initial cost. Hybrid air conditioning is defined as the combination between the vapor compression machine and desiccant system. The results were compared with the conventional system using refrigerated cooling coils. A hybrid air-conditioning system with desiccant-based could achieve high energy saving as compared to the traditional system, especially in hot and dry weather condition. Cui et al. (2005) developed new adsorbent for the desiccant cooling system. The adsorption isotherm of the zeolite 13X, silica gel, DH-5, and D-H7 were also investigated. For cooling cycle, DH-5 and DH-7 were suitable because their ability to provide higher cooling capacity of 2.2 and 1.3 times as compared to silica gel and zeolite 13X. Numerical study of desiccant wheel air conditioning was studied by Nia et al, 2006. They developed the simulation by using MATLAB Simulink to evaluate the performance of adiabatic rotary dehumidifier. The prediction of the temperature and humidity of the outlet air was calculated by using the heat and mass transfer model. The results showed that the simulation and published experimental data were agreed well with the maximum difference of 2%. Stabat and Marchio (2008) numerically studied rotary desiccant dehumidifiers. The model also included the heat and mass transfer inside the desiccant wheel system. They simplified the model by assuming some parameters such as thermal capacity ratio, effectiveness and purge section. Considering the experimental data and manufacture's data, their model offers a better result.

As aforementioned in the literature, study for developing a desiccant dehumidification system was experimentally and numerically studied by modifying essential parameters. The important process of the system was related to the contact between the air and surface of the desiccant material which considered as a variable in many types of air conditioning system research. Fundamental principal work of the desiccant dehumidification system is made up of three steps. First, the desiccant is removing the water from the process air. Since the migration of the water vapor occurs, the humidity of the desiccant will be increased. Second, to make the system can be repeated the desiccant must be regenerated. Thus, the desiccant is heated by a different airflow (regeneration air) to remove the water vapor. The desiccant should be dried enough to ensure the ability for adsorbing water vapor for the next process. After that, the desiccant material needs to be cooled to the initial temperature so that the process can be continuous.

Considering the low performance of the desiccant system, an effort to enhance the performance of the system becomes necessary at present. For the adsorption/ desorption process, the heat and mass transfer performance of the adsorbents is a critical factor which is affecting the desiccant system process (Wang et al., 2014). In this regard, several studies were performed on heat and mass transfer analysis through experimental and analytical to upgrade the performance of the desiccant system. Majumdar (1998) conducted a heat and mass transfer investigation by using the composite desiccant material pore structure for dehumidification. The composites were made of the silica gel particles and inert particles. The results show the increase of the capacitance ratio is improving the cooling capacity. Conversely, the cooling capacity tends to decrease with an increase of a fraction of the inert material. Sphaier and Worek (2004) performed the developing of a mathematical model for the transfer process. The transport phenomena inside the porous sorbent bed were described in detail to explain the heat and mass transfer on the desiccant system. It is found that new dimensionless formulation is successfully validated with the previous study including the experimental data. It is also observed that the performance could be improved by reducing the felt thickness. Inaba et al. (2008) proposed the experimental study on the heat and mass transfer characteristics of the organic sorbent coated on a heat exchanger. They have concluded that mass transport behavior depends on the mass transfer resistance of the organic sorbent. Furthermore, they have also obtained that the non-dimensional average mass transfer coefficient is a function of Reynolds number and temperature.

Nobrega and Brum (2012) proposed a comparative study of heat and mass transfer on passive and active desiccant wheels. The characteristics of the desiccant were developed by using the mathematical model. The results show the different behaviors between two desiccant wheels. For the passive dehumidification, the heat and mass transfer influence the enthalpy recovery while the active dehumidification heat and mass transfer has an impact on the regeneration temperature and adsorption capacity of the system. Li et al. (2015) investigated the heat and mass transfer characteristics for a desiccant-coated fin-tube heat exchanger during the adsorption and desorption process. They found that the parameters which affect the mass-transfer coefficient are the air flow rate, the temperature and humidity of the desiccant felt. They also developed an average overall mass-transfer coefficient and compared to the experimental values. Their results show that the deviation values fall within ±20%. In characterizing the heat and mass transfer in polymer desiccant wheels, an experimental investigation has been carried out by Kang and Lee, 2017. Three different polymers and wall thicknesses have been tested under various conditions of air velocity and rotation speed to investigate the performance of the system. It is revealed that higher dehumidification performance is achieved due to the smaller increase in sensible temperature. Based on the review of the previous study, the behavior of the desiccant system can be determined by some combined parameters. Most of them are observed the temperature and humidity variations on the performance of the system, intensively in the desiccant block. However, another critical operating condition that is called switching time is rarely reported. Switching time is defined as the required time to complete the dehumidification and regeneration process which also determines the performance of the desiccant system. Some efforts have been performed with experimental and numerical approaches by modifying the switching time to change the period of the dehumidification and regeneration time. Chang et al. (2017) investigated the dehumidification effect by using a two-desiccant-coated heat exchanger. It is found that if the switching time is appropriately considered and applied to the system, it could enhance the performance significantly. Sultan et al. (2017) reported that switching time could control the dehumidification capacity of the system, however, it depends on the application of the system. Thus, in this present study, we also consider varying the switching time with the ratio that provides the best performance of the system.

Consequently, from the above literature, the heat and mass transfer analysis have great importance on the performance of the system. Most of the works were provided the equation to predict the heat and mass transfer behaviors of the desiccant dehumidification system. However, few studies validated the heat and mass transfer balance from the experimental data. From this reason, it becomes our motivation to investigate the heat and mass transfer balance of desiccant dehumidification system by using the honeycomb block. Moreover, the present work is conducted under a wide range of temperature of the process air.

2.2 Experimental Methods

2.3.1. Experimental Facility

The design and construction of the desiccant dehumidification system, which provides good air flow regulation through the test apparatus, are illustrated schematically in Figs. 2.1 (a) and (b). The system was designed with air circulators to supply the desorption and adsorption sections, a desiccant material, and a set of control instruments. Two separate air circulators, namely APSITE: PAU-AZ1800SE (accuracy of T = ± 0.05–0.1 °C) and APSITE: PAU-H3200-6KHC (accuracy of T = ± 0.5 °C and RH = ± 2%), were operated alternately to provide the air corresponding to the adsorption and desorption processes.

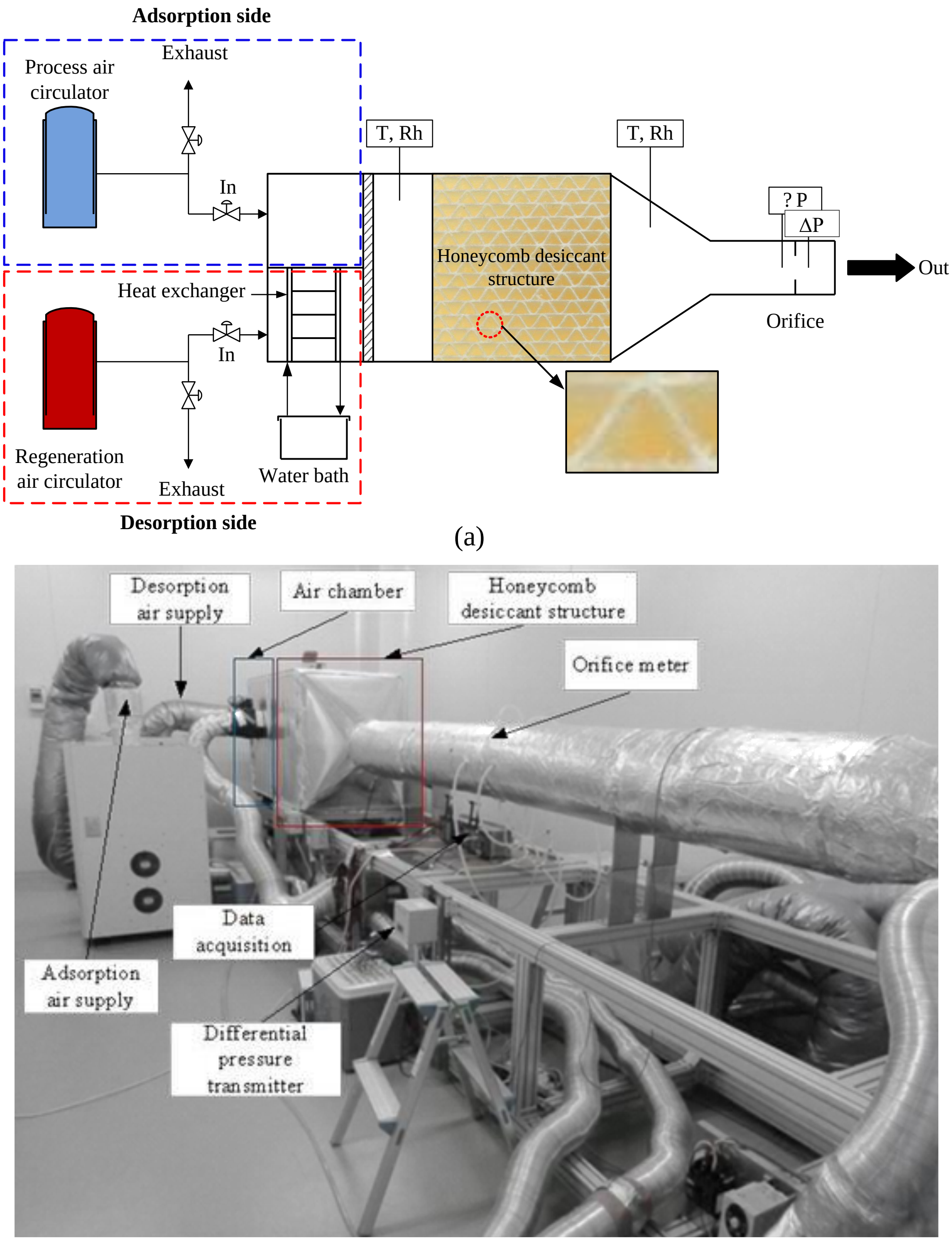

(b)

Figure 2.1. Experimental setup of the desiccant dehumidification system (a) schematic diagram; (b) photograph.

During a run of the experiment, the desorption side was set to the constant temperature (T_{des}) of 55 ºC and the relative humidity (RH) of 5%. This temperature, in addition to ensuring the use of low-grade heat sources, permits utilization of renewable energy or waste heat supplies. However, when desiccant dehumidification requires a high desorption temperature (more than 55 ºC), a flat plate heat exchanger with a circulating water bath needs to be operated. The desorption air circulator has limitations of supply of temperature and RH of maximum values of 55 °C and 85%, respectively. In the present study, the adsorption temperatures (T_{ads}) of 20º C, 25 ºC, and 35 ºC were utilized to observe the effects of various temperature on the heat and mass transfer characteristics of the desiccant dehumidification system. In order to drive an effective system, a consideration of the allocation time for the adsorption/desorption process, called the switching time, was also investigated. For each adsorption temperature, the heat and mass transfer behaviors were examined under switching time (τ) lengths of 60:60 min, 60:90 min, 60:120 min, and 90:120 min. When the adsorption and desorption processes had completed for one cycle, the total time was determined as the cycle time (t_c). Using this definition, the switching time of 60:60 min was also identified as the cycle time of 120 min, which was followed by cycle times of 150 min, 180 min, and 210 min for the switching times of 60:90 min, 60:120 min, and 90:120 min, respectively. Based on the varying parameters, a total of 12 experiments was conducted under the constant mass flow rate of 0.1 kg/s.

The characteristics of the desiccant dehumidification system are determined not only by the operating parameters but also by the design of the desiccant structure intended to improve the ability of adsorbing/desorbing moisture. For this reason, the configuration of the desiccant was designed as a honeycomb structure made of a polymer material as shown in Fig. 2.2. The details of the parameter values and properties of the honeycomb desiccant structure are provided in Table 2.1.

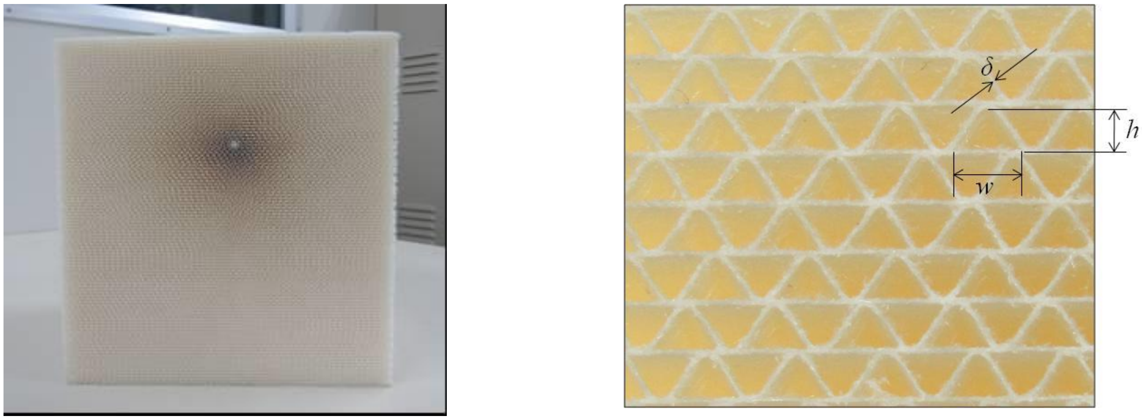

(a) (b)

Figure 2.2. Honeycomb structure of the desiccant (a) desiccant block material, (b) magnification of honeycomb structure.

Table 2.1. Parameters of polymer honeycomb desiccant structure.

Parameter	Symbol	Value	Unit
Width	W	0.2	m
Length	L	0.2	m
Height	H	0.2	m
Thickness of sorbent	δ	3 x 10^{-4}	m
Channel height (air layer)	h	1.7 x 10^{-3}	m
Fin spacing	p	3.6 x 10^{-3}	m
Heat of adsorption	q_{st}	2500	kJ/kg
Density	ρ_b	1500	kg/m^3
Specific heat capacity of the bed	$c_{p,b}$	805	kJ/kg.K
Thermal conductivity of sorbent	k_d	0.33	W/m.K
Porosity	ε	0.9	-
Radius of the adsorbent particle	R	1.29 x 10^{-6}	m

The honeycomb structure was installed inside a rectangular channel and equipped with a temperature and relative humidity sensor at the inlet and outlet. This sensor, VAISALA: HMT 333 (accuracies of T = ± 0.2–0.3 °C and RH = ± 1–1.7%), was utilized to control the air flow conditions inside the system. The desiccant dehumidification system was also instrumented with an orifice meter to allow measurements of the flow velocity of the air. The pressure differences obtained from the orifice meter were displayed by a differential pressure transmitter (TESTO: 6349; the accuracy of P = 0.35 Pa + 0.6% of full scale). Measurement values of the experimental data were collected by reading the data acquisition unit (DAQMASTER: MX 100; accuracy = ± 0.01%).

The basic working process of a desiccant dehumidification system is described below:

- The process within the desiccant dehumidification system began with the desorption mode to remove water vapor from the desiccant material, which improved the ability of the desiccant material to adsorb moisture.
- When the desorption phase was finished, and the process was switched to adsorption, the desiccant dehumidification system required a few seconds for balancing the pressure and cooling the desiccant material.
- During the adsorption process, the desiccant material adsorbed the water vapor from the moist air, leading to an increase of the air temperature at the outlet.
- Once the adsorption process was finished, the whole process of adsorption and desorption was referred to as one cycle.
- For each variation, the experiment was conducted for at least three cycles to ensure and verify the results. Thus, we could generate acceptable data. The data of the second and third cycles were considered the source data for analyzing the heat and mass transfer characteristics.

2.3.2. Experimental Data Analysis

The schematic diagram of the heat and mass transfer process between the air and desiccant wall is represented in Fig. 2.3.

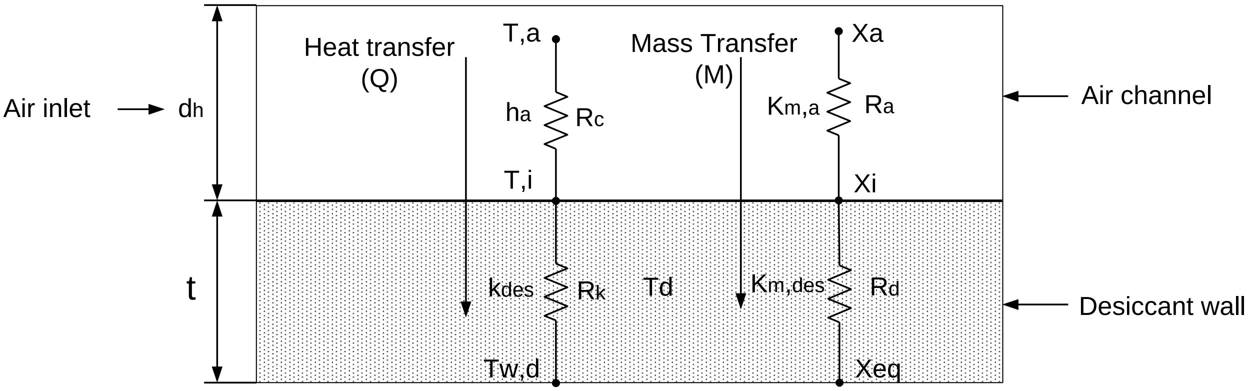

Figure 2.3. Schematic diagram of the heat and mass transfer process between air and desiccant wall.

During the dehumidification and regeneration process, the heat and mass transfer occurs between the air and desiccant material. Heat transfer (Q) process consists of two modes; latent heat transfer (Q, $_{\text{latent}}$) referring the phase change of the adsorbed molecules and sensible heat transfer (Q, $_{\text{sensible}}$) associating with the temperature difference of the air. Also, mass transfer (M) is composed of moisture transport and latent heat transport as the phase change of the adsorbed molecules. It is depicted also the thermal and mass resistance on Fig. 2.3. There are two thermal resistances for the heat transfer: convection on the air area (R_c) and conduction in the desiccant wall (R_k). Furthermore, Fig. 2.3 shows two mass transport resistances: resistance of the bulk air (R_a) and resistance of the desiccant side (R_d). The thermal and mass resistance are evaluated to determine the overall heat and mass transfer coefficient. Moreover, the overall heat and mass transfer coefficient are used to calculate the convective heat transfer (h) and mass transfer (k_t) coefficient.

The mass transport rate on the desiccant side (M_d) is evaluated based on the humidity and mass transfer coefficient (Li et al., 2015) in the following expression:

$$M_{\mathrm{d}} = k_{\mathrm{m,des}} A_{\mathrm{a}} (X_{\mathrm{i}} - X_{\mathrm{eq}}) \tag{1}$$

where $k_{\mathrm{m,\ des}}$ is the mass transfer coefficient of the desiccant side (kg(m^{2}s^{-1})). A_{a} is the area of the air side (m^2). X_{i} is the humidity ratio of the air- desiccant interface (kg/kg). X_{eq} is the humidity ratio of the desiccant side (kg/kg).

On the other hand, the mass transfer rate on the air side (M_{a}) can be evaluated by:

$$M_{\mathrm{a}} = k_{\mathrm{m,a}} A_{\mathrm{a}} (X_{\mathrm{a}} - X_{\mathrm{i}}) \tag{2}$$

where $k_{\mathrm{m,\ a}}$ is the mass transfer coefficient of the air side (kg(m^{2}s^{-1})), A_{a} is the area of the air side (m^2), and X_{a} is the humidity ratio of the air side (kg/kg).

Hence, the total mass transfer (M) is defined by:

$$M = k_{\mathrm{tot}} A_{\mathrm{a}} (X_{\mathrm{a}} - X_{\mathrm{eq}}) \tag{3}$$

Considering the mass transfer coefficient of the desiccant side and airside, total mass transfer coefficient (k_{tot}) is expressed as follows:

$$\frac{1}{k_{\mathrm{tot}}} = \frac{1}{k_{\mathrm{m,des}}} + \frac{1}{k_{\mathrm{m,a}}} \tag{4}$$

The heat transfer between the air and desiccant side consists of $Q,_{\mathrm{latent}}$ and $Q,_{\mathrm{sensible}}$. The total heat transfer rate (Q) is analyzed by the following equation:

$$Q = h_{\mathrm{a}} A_{\mathrm{a}} (T_{\mathrm{a}} - T_{\mathrm{i}}) + M.q_{\mathrm{st}} \tag{5}$$

where h_{a} is the air side heat transfer coefficient (kW(m^{2}K)$^{-1}$), T_{a} is the air temperature (K), T_{i} is the temperature of the interface between the air and desiccant surface, and q_{st} is the adsorption heat (2500 kJkg^{-1}).

2.3 Results and Discussion

Clarifying the reliability of the system, the heat and mass transfer balance under the different inlet air conditions is provided in this present work. The heat and mass balance is evaluated by calculating the difference between the dehumidification and regeneration process for each variation.

2.3.1. Humidity Ratio and Relative Humidity of Desiccant Dehumidification System

The influence of the three different process air temperatures (20 °C, 25°C and 35°C) on the humidity ratio (*X*) and relative humidity (RH) of the inlet and outlet air of the desiccant dehumidification are depicted on the Figs. 2.4 and 2.5, respectively. Based on the psychometric background, the humidity ratio and RH are closely linked with the moisture content of the air. Hence, it can be assumed that the ability of the desiccant material to adsorb the moisture from the moist air is defined as a function of the partial pressure of moist air divided by the saturation pressure or RH. This saturation vapor pressure is only the function of the temperature (ASHRAE Handbook, 2013). In general, the regeneration air has a high temperature (80 ºC - 120ºC) with low RH. However, the present study is investigated in low regeneration temperature (T_{reg}) of 55 ºC to allow the use of low-grade waste heat and solar energy (Sultan et al., 2014). This temperature is also selected to achieve the optimum dehumidification performance of the system (Mahmood et al., 2016).

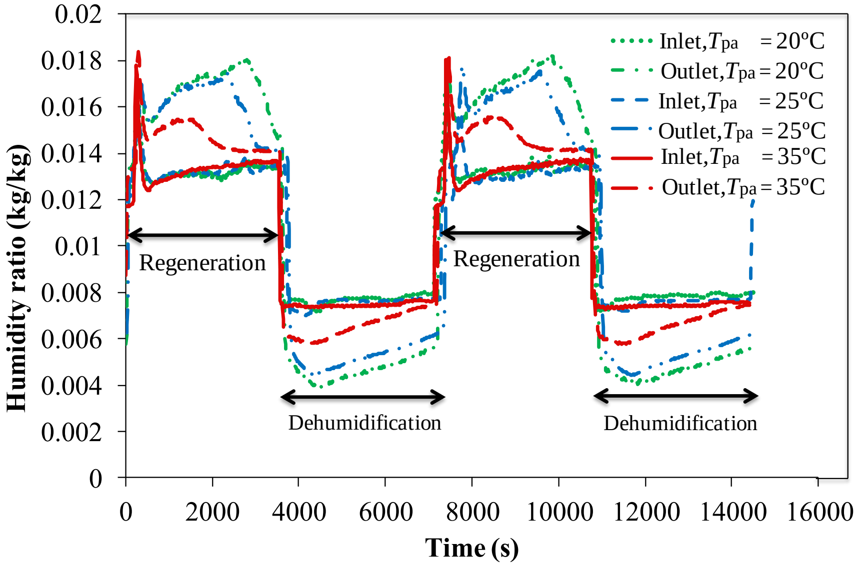

Figure 2.4. Humidity ratio (*X*) of the inlet air at switching time (t_s) of 60 min: 60 min.

In the regeneration process, the water movement takes place from the desiccant material towards the airstream. Hence, the desiccant moisture content decreases but the temperature and surface water vapor of the desiccant increases. In the other hand, the moisture of the regeneration air stream rises while the temperature decreases. As expressed in Figs. 2.4 and 2.5, during the regeneration process, the humidity ratio and RH of the outlet air are higher than those of the inlet. For all cases, humidity ratio and RH of the outlet air tend to decrease over time and show a similar value with the outlet at the end of the process. Conversely, the humidity ratio and RH of the outlet air are lower than the inlet during the dehumidification process. The process air with higher relative humidity ratio is exposed to the dry desiccant material. This process is allowed the heat of adsorption released from the desiccant material, which has a high temperature, towards the airstream. During the contact with desiccant material, the process air is dehumidified, and the temperature of the air is nearly constant (Li et al., 2015).

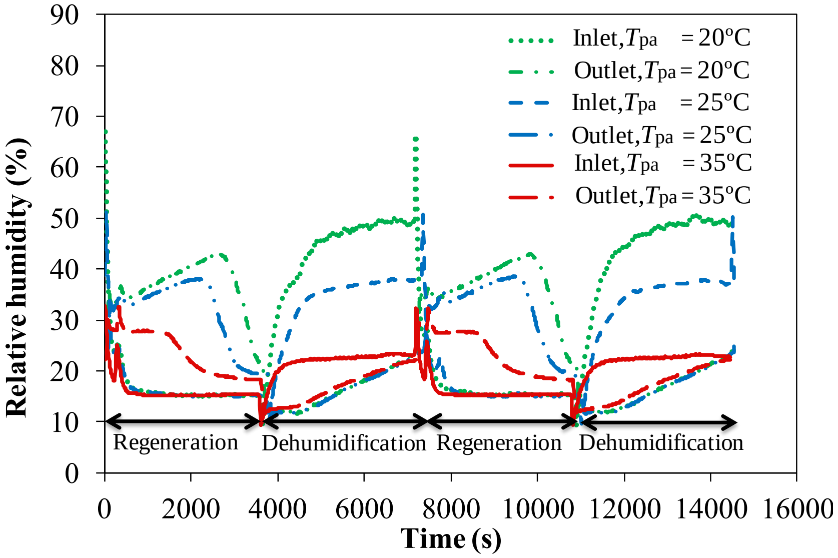

Figure 2.5. Relative humidity (RH) of the outlet air at switching time (t_s) 60 min: 60 min.

In addition, it is also shown in Figs. 2.4 and 2.5 that the low temperature of the process air has a high potential to remove the amount of the moisture. It can be explained, when the temperature increases the RH, humidity ratio decreases. Consequently, the water content also decreases. This phenomenon indicates that the water vapor pressure increases with the increase of humidity ratio. As a result, the potency of mass transfer also increases (Moon et al., 2009).

2.3.2. Dehumidification Index

Dehumidification index is defined as the differences between the humidity ratio inlet and outlet of the air during the dehumidification and regeneration process. It shows the capability of the desiccant material to adsorb/desorb the water vapor from the air. A contour plot for dehumidification index with three different process air temperatures is plotted on Fig. 2.6. In general, the dehumidification and regeneration processes play an essential role in the shape contour of the cycle. Regarding Figs. 2.4 and 2.5, during the dehumidification process, the heat of adsorption is released so that the temperature of the air increases and its humidity decreases. Thus, the vapor difference as a driving force for dehumidification reduces. Moreover, the dehumidification ability is also limited (La et al., 2010). It also can be observed from Fig. 2.6 that the different process air temperatures give different potential dehumidification capacity.

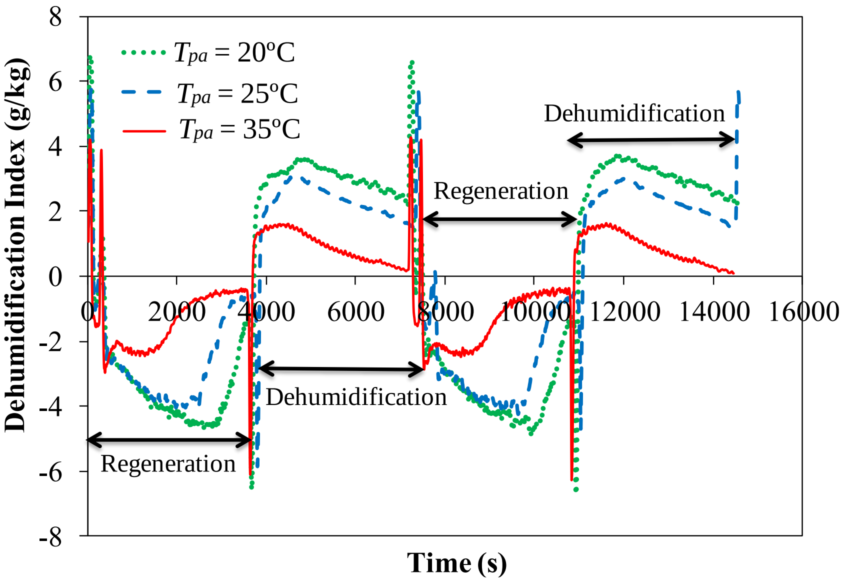

Figure 2.6. Dehumidification index at a switching time of 60 min: 60 min.

The increase of the dehumidification capacity is due to the improvement of the convective mass transport between the air and the desiccant. The dehumidification index for each variation (T_{pa} = 20 °C, 25 °C and 35 °C) are found in the value of 4.7 g/kg, 2.7 g/kg, and 0.5 g/kg, respectively.

2.3.3. Heat and Mass Balance

The effect of the process air temperature (T_{pa}) and switching time (t_s) on heat and mass transfer characteristics was evaluated by using the Eqs. (1) – (5). However, due to the complexities to measure the properties of interface between the air and desiccant wall, Eqs. (1) – (3) were simplified. The total mass transfer rate was calculated by:

$$M = \dot{m}_a \left| X_{a,in} - X_{a,out} \right| \tag{6}$$

where $\dot{m}_a$ was the mass flow rate of the process air during dehumidification and regeneration, $X_{a,in}$ and $X_{a,out}$ were the humidity inlet and outlet of the air. While for the heat transfer rate in Eq. (5), sensible heat ($Q_{,sensible}$) was calculated by:

$$Q_{,sensible} = \dot{m}_a (T_{a,in} - T_{a,out}) \tag{7}$$

where $T_{a,in}$ and $T_{a,out}$ were the temperature inlet and outlet of the air. The mass flow rate and face velocity of the process air during the dehumidification and regeneration were constant in the value of 0.1 kg/s and 0.094 m/s, respectively. From the Eqs. (1) - (7), it shows that the heat and mass transfer characteristics were mainly affected by the changing of temperature and humidity ratio of the air.

The plotting of mass transfer rate with time for dehumidification and regeneration process for the process air temperature of 20 °C and switching time (t_s) ratio of 60 min: 60 min is shown in Fig. 2.7. It can be observed that the mass transfer rate of the regeneration process generally is higher than the dehumidification process. The mass transfer of the regeneration and dehumidification process mainly depends on the humidity ratio of the process. Since the difference of the humidity ratio of the regeneration process is higher than that of the dehumidification process, the mass transfer of the regeneration process is also higher than dehumidification process. Furthermore, the hot and dry air at the regeneration process has a higher air vapor pressure consequently the mass transfer is also higher than the dehumidification process. The differences between both processes decrease with the increase of the time. However, for cyclic operation the mass adsorbed must be the same as that of regenerated

(Hamed, 2003). Hence, a proper selecting period (switching time) for each operation becomes crucial.

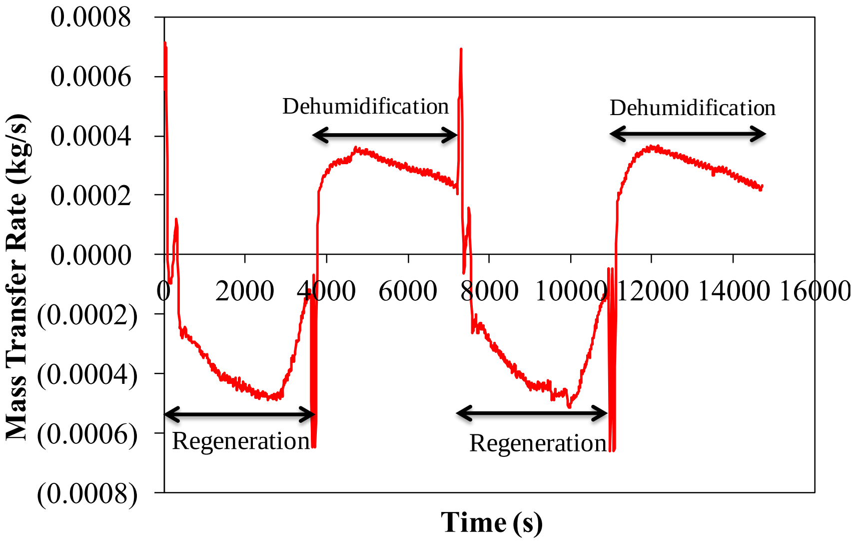

Figure 2.7. The variation of mass transfer rate with time at process air temperature of 20°C and switching time of 60 min: 60 min.

The mass transfer balance for the different inlet air temperatures is represented in Fig. 2.8. For all cases, the mass balance offers a similar tendency.

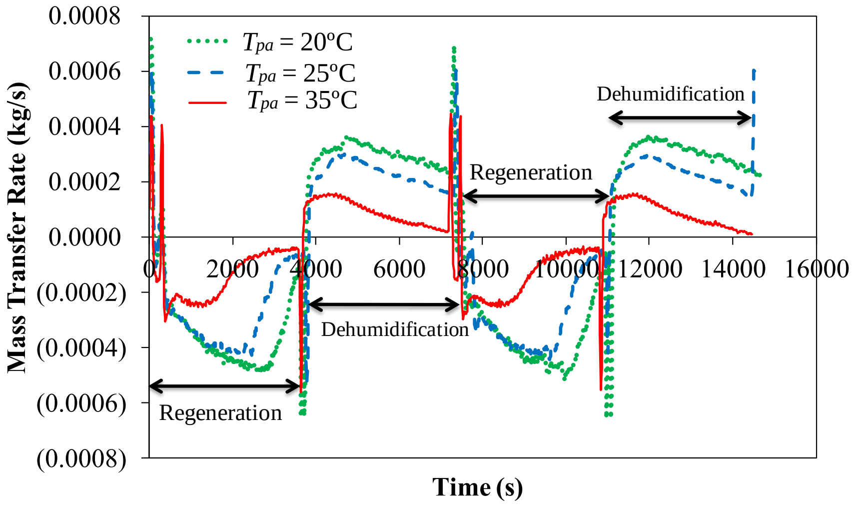

Figure 2.8. The mass transfer rate for three different inlet air temperatures at switching time 60 min: 60 min.

As shown in Fig 2.8, the increase of process air temperature will decrease the mass transfer rate of desiccant dehumidification system. The air-vapor pressure and adsorption potency will decrease when the inlet air temperature rises. It can also be justified from Fig. 2.4 that the increase of inlet air temperature will decrease the humidity ratio which is considerably affected the reduction of the moisture removal capacity. Based on the Eq. 3, the mass transfer of the desiccant dehumidification system is determined by the humidity ratio which is positively correlated with the moisture removal capacity. However, the humidity gradient in the air stream that has adsorbed/desorbed makes an important role to drive the migration of the water molecule. In other words, mass transport occurs due to the difference in mass concentration (Bird et al., 1960). In the dehumidification process, the surface of the desiccant material has higher water concentration than the center. It causes the water to diffuse inward. Additionally, as the mass flow rate and face velocity were constant, the dehumidification process was longer than the regeneration process.

Figure 2.9 shows that $Q,_{total}$, $Q,_{sensible}$ and $Q,_{latent}$ at process air temperature and switching time for 20°C and (60 min: 60 min), respectively. In the regeneration process, the DSC material has lower humidity and temperature than the airstream. Hence, the heat is transferred from the hot air to the DSC material. The total heat transfer rate for the regeneration process can be defined as the differences between the $Q,_{sensible}$ and $Q,_{latent}$. Thus, in the regeneration process, the $Q,_{total}$ can be lowered than $Q,_{sensible}$. Whereas, in the dehumidification process, when the humid air meets the DSC material the heat is transferred from the DSC material to the air stream. $Q,_{total}$ for the dehumidification process is calculated by summing the $Q,_{latent}$ and $Q,_{sensible}$. From Fig. 2.9, the $Q,_{total}$ for both processes offers the same trend. The $Q,_{total}$ tends to decrease with the increase of time because of the decrease in mass transfer (Li et al., 2015). Further, the effect of the temperature difference is more prominent than the phase change of the adsorbed moisture. It can be shown from the Fig. 2.9 that the $Q,_{sensible}$ is higher than $Q,_{latent}$. The similar trend appears for all cases.

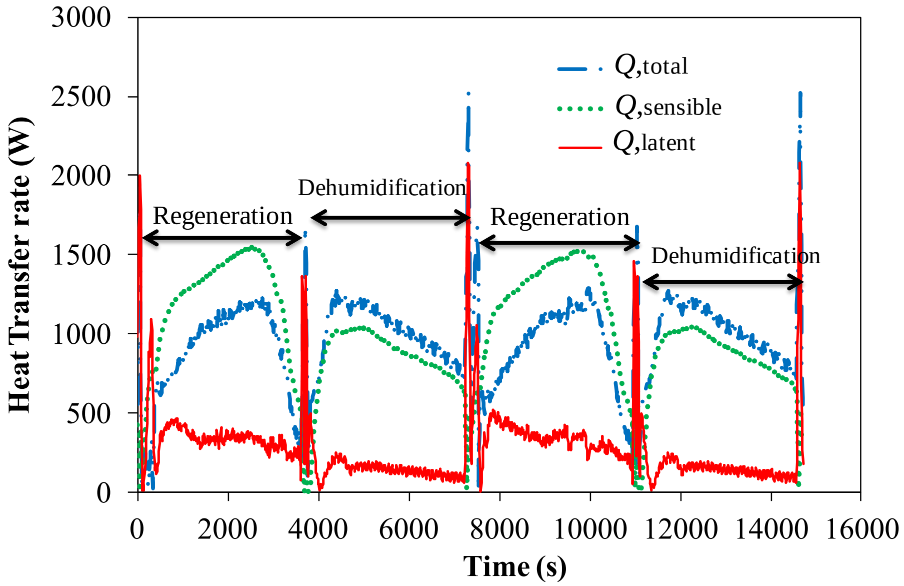

Figure 2.9. The variation of heat transfer rate with time at process air temperature and switching time for 20 °C and (60 min: 60 min), respectively.

Also, the HMT balance is calculated to clarify the reliability and feasibility of the present experimental data. Based on the thermodynamic principle, the HMT of the dehumidification and regeneration processes must be balanced. In this work, the difference between the HMT of the dehumidification and regeneration process is found less than 8%. The details of HMT for all cases are resumed in Tables 2.2 and 2.3.

Table 2.2. The discrepancy of the heat transfer of desiccant dehumidification system for all cases.

t_s (min:min) T_{pa} (ºC)	60:60	60:90	60:120	90:120
20	7.1%	4.3%	7%	4.4%
25	5.7%	4.4%	4.4%	5.6%
35	4.7%	4.5%	3.7%	7%

Table 2.3. The discrepancy of the mass transfer of the desiccant dehumidification system for all cases.

t_s (min:min) / T_{pa} (°C)	60:60	60:90	60:120	90:120
20	1.04%	2%	2.5%	5.3%
25	1%	2.8%	4.4%	2.2%
35	1.8%	3.6%	6%	4.5%

Additionally, all the data (Figs. 2.4-2.9) shows overshoot at the time between the dehumidification and regeneration. Alternating the process between regeneration and dehumidification was completed by switching the air flow control valves. Due to a sudden change of the pressure and temperature of the air, thus all data is overshoot.

2.4 Conclusions

The experimental study of the desiccant dehumidification system under three different air inlet temperatures and four different switching times has been done. The concluding remarks can be drawn as follows: at higher humidity ratio, the desiccant dehumidification will get higher moisture removal. Moisture removal mass increases with increasing RH, due to the higher mass transfer potential between air and desiccant. Dehumidification capacity of the desiccant system shows that the desiccant dehumidification system has a high potential as air conditioning devices. Heat and mass balance are shown the discrepancy less than 8%, those of the experimental methods are reliable to conduct a further experiment.

Nomenclature

A_a	air channel surface area (m^2)
$c_{p,b}$	specific heat capacity of the bed (kJ/kg.K)
h	channel height for air layer (m)
h_a	convective heat transfer coefficient of the air (W/m^2K)
H	honeycomb height (m)
q_{st}	adsorption heat (kJ/kg)
k_m	average of overall mass transfer coefficient (kg/m^2s)
$k_{m,a}$	mass transfer coefficient of the air (kg/m^2s)
$k_{m,des}$	mass transfer coefficient of the desiccant side (kg/m^2s)
k_{tot}	total mass transfer coefficient (kg/m^2s)
L	honeycomb length (m)
M_v	overall mass transfer rate (kg/s)
$M_{v,a}$	mass transfer rate of the air (kg/s)
M_d	mass transfer rate of the desiccant (kg/s)
Nu	Nusselt number
p	fin spacing (m)
P	pressure (Pa)
Q_d	total heat transfer (W)
$Q,_{\mathrm{latent}}$	latent heat (W)

$Q,_{\text{sensible}}$	Sensible heat (W)
R_c	thermal resistance for convection
R_k	thermal resistance
R_a	mass resistance of the air channel
R_d	mass resistance of the desiccant wall
t_c	cycle time (min)
T_a	air temperature (K)
T_{ads}	adsorption temperature (K)
T_{des}	desorption temperature (K)
T_i	interface temperature (K)
W	honeycomb width (m)
X_a	humidity ratio of the air (kg/kg)
X_{eq}	humidity ratio of the desiccant (kg/kg)
X_i	humidity ratio of interface (kg/kg)

Greek Symbols

τ	switching time (min)
ε	porosity
δ	thickness of sorbent (m)
ρ_b	density of the bed (kg/m^3)

References

ASHRAE Handbook, Fundamentals, Psychrometrics Chapter 1, p. 1.8-1.9, 2013.

Bird, R. B., Stewart, W.E., Lightfoot, E.N., Transport Phenomena, John Wiley & Sons, Inc, London,1960.

Chang, C., Luo, W., Lu, C., Cheng, Y., Tsai, B., Lin, Z., Effects of process air conditions and switching cycle period on dehumidification performance desiccant-coated heat exchangers, Science, and Technology for the Built Environment 23 (2017) 81-90.

Cui, Q., Chen, H., Tao, G., Yao, H., Performance study of new adsorbent for solid desiccant cooling, Energy 30 (2005) 273-279.

Dhar, P.L., Singh, S.K., Studies on solid desiccant based hybrid air-conditioning systems, Appl. Therm. Eng. 21 (2001) 119-134.

Hamed, A.M., Desorption characteristics of desiccant bed for solar dehumidification/ humidification air conditioning systems, Renew. Energy 28 (2003) 2099-2111.

Inaba, H., Komatsu F., Horibe A., Haruki N., Machida A., Heat and mass transfer characteristics of organic sorbent coated on heat transfer surface of a heat exchanger, Heat Mass Transf 44 (2008) 1305-1313.

Kang, H., Lee, D., Experimental investigation and introduction of a similarity parameter for characterizing the heat and mass transfer in polymer desiccant wheels, Energy 120 (2017) 705-717.

La, D., Dai, Y.J., Li, Y., Wang, R.Z., Ge, T.S., Technical development of rotary desiccant dehumidification and air conditioning: a review, Renew Sustainable Energy Rev. 14 (2010) 130-147.

Li, Z., Michiyuki, S., Takhesi, F., Experimental study on heat and mass transfer characteristics for a desiccant-coated fin-tube heat exchanger, Int J Heat Mass Transf 89 (2015) 641-651.

Mahmood, M. H., Sultan, M., Miyazaki, T., Koyama, S., Theoretical and experimental analysis of desiccant air conditioning system for storage of agricultural products, Proc. 16th Int. Refrigeration and Air Conditioning Conference, 2261, 2016, 1-10, USA.

Moon, C.G., Bansal, P.K., Jain, S., New performance data of a cross flow liquid desiccant dehumidification system, Int. J. Refrig 32 (3) (2009) 524-533.

Majumdar, P., Heat and mass transfer in composite desiccant pore structures for dehumidification, Sol Energy 62 (1998) 1-10.

Majumdar, P., Worek, W.M., Performance of an open-cycle desiccant cooling system using advance desiccant matices, Heat Recovery Syst. CHP 9 (1989) 299-311.

Nia, F. E., Paassen, D., Saidi, M.H., Modeling and simulation of desiccant wheel for air conditioning, Energy Build. 38 (2006) 1230-1239.

Nobrega, C.E.L., Brum, N.C.L., An analysis of heat and mass transfer roles in air dehumidification by solids desiccant, Energy Build. 50 (2012) 251-258.

Sphaier, L.A., Worek W.M., Analysis of heat and mass transfer in porous sorbents used in rotary generators, Int J Heat Mass Transf 47 (2004) 3415-3430.

Stabat, P., Marchio, D., Heat and mass transfer modelled for rotary desiccant dehumidifiers, Appl Energy 85 (2008) 128-142.

Sultan, M., Miyazaki, T., Koyama, S., Khan, Z. M., Performance evaluation of hydrophilic organic sorbents for desiccant air-conditioning applications, Adsorpt. Scie. and Technol. 0(0) (2017) 1-16.

Sultan, M., El-Sharkawy, I.I., . Miyazaki, T, Saha, B.B., Koyama, S., Experimental study on carbon based adsorbents for greenhouse dehumidification, Evergreen 01 (2014) 5-11.

Wang, R., Wang, L., Wu, J., Adsorption Refrigeration Technology Theory and Application, John Wiley and Sons, Singapore, 2014.

CHAPTER 3

Chapter 3

HEAT AND MASS TRANSFER CHARACTERISTICS OF DESICCANT DEHUMIDIFICATION SYSTEM

This chapter provides the heat and mass transfer characteristics, in the form of the Nusselt number (*Nu*) and the Sherwood number (*Sh*), of a desiccant dehumidification system. The desiccant dehumidification system was driven by using the honeycomb desiccant configuration, which was constructed from a polymer adsorbent material. The adsorption temperature (T_{ads}) was considered as an adjustable parameter using values of 20 ºC, 25 ºC, and 35 ºC. Each adsorption temperature was evaluated under the time intervals for the desorption and adsorption processes (switching time: τ) of 60:60 min, 60:90 min, 60:120 min, and 90:120 min. For the given parameters, the desorption temperature and mass flow rate of the air were kept unchanged at 55 ºC and 0.1 kg/s, respectively. The results showed that the *Nu* and *Sh* are more evenly responsive to change of adsorption temperature than switching time. Low adsorption temperature results in high values of *Nu* and *Sh*. However, the variation of switching time produces little change in *Nu* and *Sh*. Empirical correlations were also developed in this study. The empirical correlations matched the experimental data well.

3.1 Introduction

The demand for air conditioning (AC) devices has increased almost continuously because of the desire to achieve indoor comfort of occupants and additionally due to climate change. This condition has prompted an increase in efforts to improve AC technology. However, in contrast, most of the technology that modifies the condition of the air, such as by cooling/heating and dehumidification/humidification, consumes a large amount of energy. This issue is crucial when the energy used to drive the systems comes mostly from fossil fuels. Therefore, determining a development strategy of AC technology with a trend toward reducing energy consumption has become essential. Basically, the key aspect of the functioning process of AC is adding/removing heat and moisture. Adapting variable conditions of the AC system could help improve heat and mass transport within the system. In recent years, therefore, studies of the heat and mass transfer of the AC system have been conducted to identify and develop promising devices. These studies have focused on developing systems with enhanced heat transfer coefficient, modified parameter conditions, and modeled performance limitations to achieve ideal conditions (Criptoph et al.,1996; Zalewski and Gryglaszewki, 1997; Sommers and Jacobi, 2005; Miyazaki and Akisawa, 2009; Naphon, 2010; Kim et al., 2010; Wang et al.,2011; Zhang et al., 2012).

Adsorption technology has been proposed as a potential AC system that could provide an almost ideal condition. Considering its ability to reduce the humidity of air by using an adsorbent material, the most important application of adsorption technology is a dehumidifier system. A desiccant dehumidifier consumes less energy because of the possibility of coupling it with renewable energy or waste heat. However, even if the desiccant dehumidifier can provide great advantages, the performance of this system is still not satisfying. It is highly variable with the properties of the desiccant material and the air during the adsorption and desorption process. For the adsorption/desorption process, the desiccant material must be capable of releasing water vapor easily and also capturing water molecules when the process changes to the adsorption phase. Understanding the behaviors of both processes is very important to achieving an effective and efficient desiccant dehumidifier system. Currently, the influenced parameters, such as temperature and humidity of the air, the characteristics, and the structures of desiccant materials are being investigated widely both experimentally and numerically to improve the performance of the adsorption system.

A simulation model of adsorption cycles using a carbon–ammonia pair to enhance the heat transfer by forced convection was studied by Criptoph, 1994. A counter-flow heat exchanger was utilized to improve the coefficient of performance (COP) of the system by regenerative heating. The parameters considered were grain heat transfer coefficient, bed length, inlet gas velocity, and desorption gas inlet temperature. They found that the adsorption cycles offered a COP of about 1.3 within the range of cases modeled. They also stated that the results of the model were not sensitive when assuming the grain heat transfer coefficient. Yanagi and Ino (1997) investigated the heat and mass transfer characteristics of refrigeration cycles, particularly in the adsorption heat exchanger, by using consolidated silica gel. The results were compared to results with the granular heat exchanger. The heat and mass transfer characteristics of the consolidated bed were determined by varying the mass of desorption and the adsorption temperature. They found that the increased packing density of the consolidated bed configuration decreased the mass transfer rate. Also, compared with a granular bed, the consolidated bed reached a higher value of overall heat transfer coefficient. A heat and mass transfer model of the adsorption and desorption processes for the composite desiccant dehumidifier using silica gel and inert material was developed by Majumdar, 1998. Heat and mass transport resistances for the gas and solid sides were also considered when developing the model. Gas-phase diffusion and surface diffusion were included for calculation of the mass resistance of the solid side. The model was developed by varying the fraction of the inert material and the thermal capacitance ratio. They observed that a high value of capacitance ratio increases the cooling capacity. The adsorption rate was also increased by increasing the fraction of the inert material. Both aspects affected the heat and mass transfer characteristics of the composite desiccant dehumidifier. The surface phenomena of the adsorption/desorption process and the heat/mass transfer on the flat walls of a honeycomb adsorption column were reported by Fedorov and Viskanta, 1999. The system was modeled by a two-dimensional analysis with a transient condition. However, the model was also compared with experimental data. They found good agreement between the numerical simulation and the experimental data. The mass flux of the channel walls was significantly affected by the adsorption/desorption processes. Moreover, the adsorption and desorption processes had an opposite behavior. For adsorption, the sensible heat fluxes decreased due to the high increase of the local heat transfer coefficient rather than a decrease of the bulk-to-wall temperature difference, and vice versa for desorption temperature.

The performance of a cooling system using graphite/silica-gel blocks was studied experimentally by Eun at al., 2000 and the results were compared with those of the silica-gel packed bed. They found that the mass transfer affected the axial profile temperature of the composite blocks, while the radial distribution of the temperature was influenced by heat transfer. Compared with the silica gel, the composite blocks presented higher heat and mass transfer, which enhanced the performance of the cooling system. Restuccia et al. (2002) modeled heat and mass transfer of sorption air-conditioning systems by using a zeolite-coated adsorbent bed. The model also allowed the calculation of exchanged energies, cycle time, and specific power. A new configuration consisting of an adsorbent coating with a zeolite base was proposed and compared with the traditional bed. The zeolite was firmly bound to the metal heat exchanger. An optimization study was also conducted. The model only considered heat and mass transfer resistances inside the cylindrical adsorber, while axial gradient pressure and temperature were neglected. They observed that the new configuration of the bed showed the highest specific cooling power. From the model, they also found that the competitiveness of the adsorption air-conditioning system could be enhanced by designing the shape of the adsorbent material. This was also expected to affect its thermo-physical properties. Sphaier and Worek (2004) analyzed the heat and mass transfer of rotary regenerators using a porous sorbent. The simulation included all parameters affecting the heat and mass transfer within the system: sorbent felt, felt and process stream properties. The results showed that the performance of the system increases with the variation of mass fraction of the sorbent inside the felt and decreases with time. Nóbrega and Brum (2012) presented a comparative study of the heat and mass in passive and active adsorptive air dehumidification systems. A mathematical model was developed to simulate the dynamic behavior of the desiccant wheel. Their study focused mainly on the effectiveness of the active and passive desiccant wheels. As a result, they observed that the heat and mass transfer of passive dehumidification were affected by the enthalpy recovery of the system, whereas the heat and mass transfer of active dehumidification were associated with the dehumidification capacity.

Li et al. (2015) conducted an experimental study characterizing the heat and mass transfer of the desiccant-coated fin-tube heat exchanger (DCHE). The influences of air velocity, desiccant temperature, and desiccant moisture content on the mass-transfer coefficient were also evaluated separately for the adsorption and desorption processes. They found that increases in air velocity and moisture content of the desiccant led to an increase in the overall mass-transfer coefficient. Conversely, higher temperature resulted in a lower overall mass-transfer coefficient. A calculation model for heat transfer rate was evaluated based on the sensible heat and latent heat inside the DCHE. Additionally, the model was verified with the experimental results, and good agreement was obtained. Zhao et al. (2015) investigated the heat and moisture transport characteristics of a dehumidification unit in the form of a fin-tube heat exchanger with a silica-gel coating. They provided empirical correlations for the Nusselt number and Sherwood number on the air side of the unit. Under given Reynolds number, they found that the empirical correlations agreed well with the experimental data. In addition, they also stated that the empirical correlations were capable of predicting the performance of the system. A detailed study of transient heat transfer phenomena of powdered adsorbent embedded onto fin heat exchangers was presented by Li et al., 2016. The adsorption temperature was varied to measure the heat transfer, and the influence of the thermal mass effect was evaluated to determine the transient overall and local adsorption heat transfer coefficients. A correlation was also developed and compared with the experimental data. From the results, they concluded that the thermal mass effect of the adsorbent–adsorbate interaction layer significantly influenced the local adsorption heat transfer coefficient, causing it to be higher than the average value. Fu et al. (2017) predicted the cyclic behaviors of desiccant wheels by using a heat and mass transfer transient model. The performance of various desiccant wall materials was investigated under different rotary speeds and inlet velocities of the process air and exhaust air, and the parameters considered significantly influenced the performance of the system.

Many reports of experiments and predictive analytical models for the heat and mass transfer characteristics of an adsorption system have been published. However, if these reports describe models, they do not explain observed details of the calculations to examine the heat and mass transfer phenomena of a desiccant system. In this study, we provide a detailed data assessment for calculating the heat and mass transfer analysis of a desiccant dehumidifier system using a honeycomb structure. A brief method for calculating the temperature profile during the adsorption process is also provided. Considering literature review for the parameter which affected the heat and mass transfer characteristics, the influence of the adsorption temperature and switching time is investigated in the present study. Nusselt number (Nu) and Sherwood number (Sh) are chosen to represent the heat and mass transfer characteristics, respectively.

Finally, the present study also proposes correlations for predicting the heat and mass transfer behaviors in terms of the Nusselt and Sherwood numbers.

3.2 Experimental Methods

3.3.1. Experimental Facility

The experimental setup for heat and mass transfer investigation was described in detail in Chapter 2.

3.3.2. Experimental Data Analysis

The heat and mass transfer behaviors of the desiccant dehumidification system were examined as a function of the Nusselt number (*Nu*) and the Sherwood number (*Sh*), respectively. The procedure to analyze both the heat and mass transfers of the desiccant dehumidification system involved all the properties of the air and desiccant material. The inputs of the heat and mass transfer analysis are shown in Fig. 3.1.

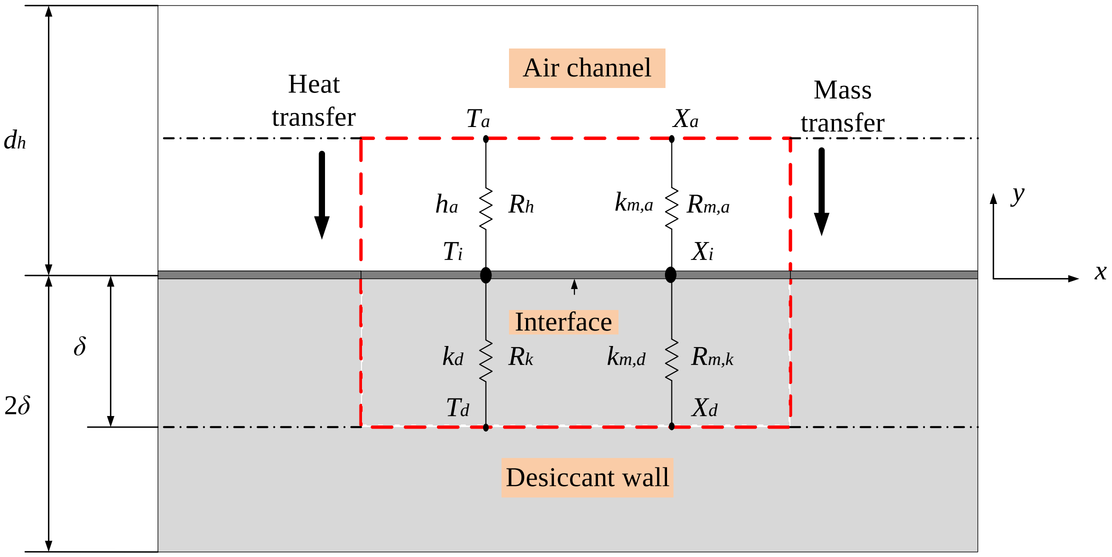

Figure 3.1. Heat and mass transfer between the air and the desiccant material.

Determination of heat and mass transfers was evaluated by using the contact resistance concept. As shown in Fig. 3.1, the contact resistance between the air flow and desiccant material can be subdivided into thermal resistance for heat transfer and mass resistance for mass transfer. Basically, the heat transfer and mass transfer occur due to the temperature and phase exchange between the desiccant material and air flow, respectively. The complete details of the procedures for calculating the heat and mass transfer characteristics will be described individually.

1) Heat Transfer Characteristic

As shown in Fig. 3.1, the calculation of heat transfer rate was conducted by considering the thermal resistances for convection (R_h) and conduction (R_k) in series. R_h and R_k were defined as follows:

$$R_h = \frac{1}{h_a A_a} \quad \text{and} \quad R_k = \frac{\delta}{k_d A_d} \tag{1}$$

From Eq. 1, the heat transfers for the air channel (Q_a) and desiccant (Q_d) sides were obtained as

$$Q_a = Q_{conv,air} = h_a A_a (T_a - T_i) = \frac{1}{R_h}(T_a - T_i) \tag{2}$$

$$Q_d = Q_{cond,des} + Q_{ads} \tag{3}$$

$$Q_d = \frac{k_d A_d (T_i - T_d)}{\delta} + \Delta H_{ads} k_{m,d} A_d (X_i - X_d) = \frac{1}{R_k}(T_i - T_d) + M_v \Delta H_{ads} \tag{4}$$

where h_a is the convective heat transfer coefficient of the air; k_d is the thermal conductivity of the desiccant material; A_a and A_d are air channel and desiccant surface area, respectively; T_a, T_i, and T_d are bulk air, interface, and desiccant wall temperature, respectively; M_v is mass transfer rate; $k_{m,d}$ is the mass transfer coefficient of the desiccant; X_i is the humidity of the interface, X_d is the humidity of desiccant, ΔH_{ads} is the adsorption heat, and δ is the half-thickness of the desiccant wall.

Designating equations (2) and (4), the energy balance can be written as follows:

$$h_a A_a (T_a - T_i) = \frac{k_d A_d (T_i - T_d)}{\delta} + M_v \Delta H_{ads} \tag{5}$$

From Eq. 5, the convective heat transfer coefficient (h_a) can be expressed as

$$h_a = \frac{\left[\frac{k_d A_d (T_i - T_d)}{\delta}\right] + M_v \Delta H_{ads}}{A_a (T_a - T_i)} \tag{6}$$

Therefore, the Nusselt number can be defined as

$$Nu = \frac{h_a D_h}{k} \tag{7}$$

where D_h is the hydraulic diameter of the air channel and k is the thermal conductivity of the air.

2) Mass Transfer Characteristic

Consider two mass resistances, one for the air channel ($R_{m,a}$) and one for the desiccant wall ($R_{m,k}$), as shown in Fig. 3.1 then the mass transport characteristic for desiccant dehumidification system can be determined by the following step:

Utilizing the mass transfer coefficients on both sides, the mass transfer rates for air ($M_{v,a}$) and desiccant ($M_{v,d}$) are given as follows:

$$M_{v,a} = k_{m,a} A (X_a - X_i) \tag{8}$$

$$M_{v,d} = k_{m,d} A (X_i - X_d) \tag{9}$$

where $k_{m,a}$ and $k_{m,d}$ are the mass transfer coefficient on the air and desiccant side; A is the area of adsorption; and X_a, X_i, and X_d are the humidity ratio of the air, interface, and desiccant, respectively.

The overall mass transfer rate (M_v) obtained from the experimental results was examined by

$$M_v = \dot{m}_a \left(X_{a,in} - X_{a,out}\right) \tag{10}$$

where $\dot{m}$ is the mass flow rate of the air and $X_{a,in}$ and $X_{a,out}$ are the humidity ratio of the air inlet and outlet, respectively.

Applying the mass balance, Eqs. (7), (8), and (9) can be rearranged and the mass transfer rate can be written as follows:

$$M_v = M_{v,a} = M_{v,d} \tag{11}$$

$$M_v = k_m A(X_a - X_d) \tag{12}$$

where k_m is the average overall mass transfer coefficient, which is given as

$$\frac{1}{k_m} = \frac{1}{k_{m,a}} + \frac{1}{k_{m,d}} \tag{13}$$

By using the analogy between the non-dimensional parameters for heat and mass transfer, the mass transfer coefficient of the air side was obtained according to the following procedure:

The parameter used for characterizing the mass transfer was the Sherwood number (*Sh*), which is defined as follows:

$$S_h = \frac{k_{m,a} D_h}{D_{va}} \tag{14}$$

where D_{va} is the coefficient of mass diffusion for water vapor. The *Nu* and *Sh* can also be defined as functions of the Reynolds number (*Re*) and the Prandtl number (*Pr*) for *Nu* or the Schmidt number (*Sc*) for *Sh* as follows:

$$Sh = \mathrm{f}\,(Re, Sc) \tag{15}$$

$$Nu = \mathrm{f}\,(Re, Pr) \tag{16}$$

To simplify the relation between heat and mass transfer, a ratio between *Pr* and *Sc*, referred to as the Lewis number (*Le*) (Eckert and Drake, 1972), was also considered. It is a non-dimensional parameter given by the following expression:

$$Le = \frac{Pr}{Sc} = \frac{D_{va}}{\alpha} = \frac{\rho c_p D_{va}}{k_a} \tag{17}$$

Taking advantage of considering the value of *Le* = 1, Eq. 14 was rewritten as

$$D_{va} = \frac{k_a}{\rho c_p} \tag{18}$$

Thus, the consequence of the analogy between *Nu* and *Sh* resulting in a correlation by which the mass transfer coefficient can be obtained is given by

$$\frac{h_a D_h}{k_a} = \frac{k_{m,a} D_h}{D_{va}} \tag{19}$$

$$k_{m,a} = \frac{h_a}{\rho c_{p,a}} \tag{20}$$

where α is the thermal-diffusion coefficient; ρ is the density of the air; and $c_{p,a}$ is the specific heat capacity of the air.

3) Adsorption rate

To evaluate the adsorption characteristics, the adsorption rate based on the Linear Driving Force (LDF) Model was examined in this study. It was calculated by (Glueckauf and Coates, 1947):

$$\frac{dW}{dt} = \frac{F_o D_e}{R^2}\left(W_{eq} - w\right) \tag{21}$$

where $\frac{dW}{dt}$ is the adsorption rate; F_o is the geometric parameter for adsorbent particle shape, D_e is the surface diffusion coefficient; R is the radius of the adsorbent particle; W_{eq} is the equilibrium adsorption uptake; and w is the instantaneous adsorption uptake. In the calculation, F_o is equal to 15 (Sultan et al., 2016). The W_{eq} was calculated by using Guggenheim, Anderson, De Boer (GAB) Model as written by:

$$W_{eq} = \frac{w_m CK\left(\frac{P}{P_o}\right)}{\left((1 - K\left(\frac{P}{P_o}\right)\right)\left(1 - (1 - K\left(\frac{P}{P_o}\right) + CK\left(\frac{P}{P_o}\right)\right)} \tag{22}$$

$$w_m = w_{mo}\,exp\left(\frac{q_m}{RT_{ads}}\right) \tag{23}$$

$$C = C_o\,exp\left(\frac{\Delta H_c}{RT_{ads}}\right) \tag{24}$$

$$K = K_o\,exp\left(\frac{\Delta H_k}{RT_{ads}}\right) \tag{25}$$

Where P is the pressure, P_o is the saturation pressure, R is the specific gas constant for water vapor; w_{mo}, q_m, K, C, K_o, and C_o are variable constant related to the heat; ΔH_c, ΔH_k are the water vapor sorption heat. The values of the constant were provided in Table 3.1 (Sultan et al., 2018).

Table 3.1. The parameters of the GAB Model (Sultan et al., 2018).

Parameters	Value
w_{mo} (kg/kg)	0.05
C_o (-)	0.26
K_o (-)	1.16
q_m (kJ/kg)	202.38
ΔH_c (kJ/kg)	433.41
ΔH_k (kJ/kg)	-60.48

4) Uncertainty Analysis

Uncertainty analysis for the non-dimensionless parameter was also conducted by calculating the individual uncertainties of the sources. The process for each parameter is described hereafter.

- Uncertainty for Reynolds number

The Reynolds number (*Re*) and its uncertainty were calculated from Eqs. 26 and 27, respectively:

$$Re = \frac{\rho V D_h}{\mu} \tag{26}$$

$$u(Re) = \sqrt{\left(\frac{\partial Re}{\partial \rho}\right)^2 u^2(\rho) + \left(\frac{\partial Re}{\partial u}\right)^2 u^2(u) + \left(\frac{\partial Re}{\partial D_h}\right)^2 u^2(D_h) + \left(\frac{\partial Re}{\partial \mu}\right)^2 u^2(\mu)} \tag{27}$$

where *V* is the air velocity and μ is the dynamic viscosity of the air.

- Uncertainty analysis for Nusselt number

From Eq. (7), the Nusselt number (*Nu*) was calculated in terms of the convective heat transfer coefficient, hydraulic diameter of the air channel, and thermal conductivity of the fluid. Thus, the uncertainty of the *Nu* can be estimated as follows:

$$u(Nu) = \sqrt{\left(\frac{\partial Nu}{\partial h_a}\right)^2 u^2(h_a) + \left(\frac{\partial Nu}{\partial D_h}\right)^2 u^2(D_h) + \left(\frac{\partial Nu}{\partial k}\right)^2 u^2(k)} \tag{28}$$

- Uncertainty analysis for Sherwood number

As written in Eq. (14), the Sherwood number (*Sh*) was obtained in terms of the mass transfer coefficient of the air, the hydraulic diameter, and the coefficient of mass diffusion of the water vapor. The uncertainty of *Sh* was calculated by the following equation:

$$u(S_h) = \sqrt{\left(\frac{\partial S_h}{\partial k_{m,a}}\right)^2 u^2(k_{m,a}) + \left(\frac{\partial S_h}{\partial D_h}\right)^2 u^2(D_h) + \left(\frac{\partial S_h}{\partial D_{va}}\right)^2 u^2(D_{va})} \tag{29}$$

- Uncertainty analysis for humidity ratio

The humidity ratio (*X*) and its uncertainty were estimated as follows:

$$X = 0.62198\,\frac{\varphi P_s}{P - \varphi P_s} \tag{30}$$

$$u(X) = \sqrt{\left(\frac{\partial X}{\partial \varphi}\right)^2 u^2(\varphi) + \left(\frac{\partial X}{\partial P}\right)^2 u^2(P) + \left(\frac{\partial X}{\partial P_s}\right)^2 u^2(P_s)} \tag{31}$$

where φ is the relative humidity of the air, P is the atmospheric pressure, and P_s is the saturation water vapor pressure. The values of the uncertainty measurements for each parameter are listed in Table 3.2.

Table 3.2. Uncertainty analysis of non-dimensional parameters.

Parameter	Symbol	Value
Reynolds number	*Re*	1.95%
Nusselt number	*Nu*	2.55%
Sherwood number	*Sh*	2.7%
Humidity ratio	*X*	1.83%

3.3 Results and Discussion

3.3.1. Effect of Adsorption Temperature on Heat and Mass Transfer Characteristics

The heat and mass transfer characteristics of desiccant dehumidification system for each adsorption temperature have the appearances shown in Figs. 3.2 (a) and (b) for Nusselt number (*Nu*) and Sherwood number (*Sh*), respectively. For all cases, the illustrations show that the values of *Nu* and *Sh* have similar trends. Under a constant adsorption temperature, when investigated for various switching times, *Nu* and *Sh* also showed consistency in the trend line.

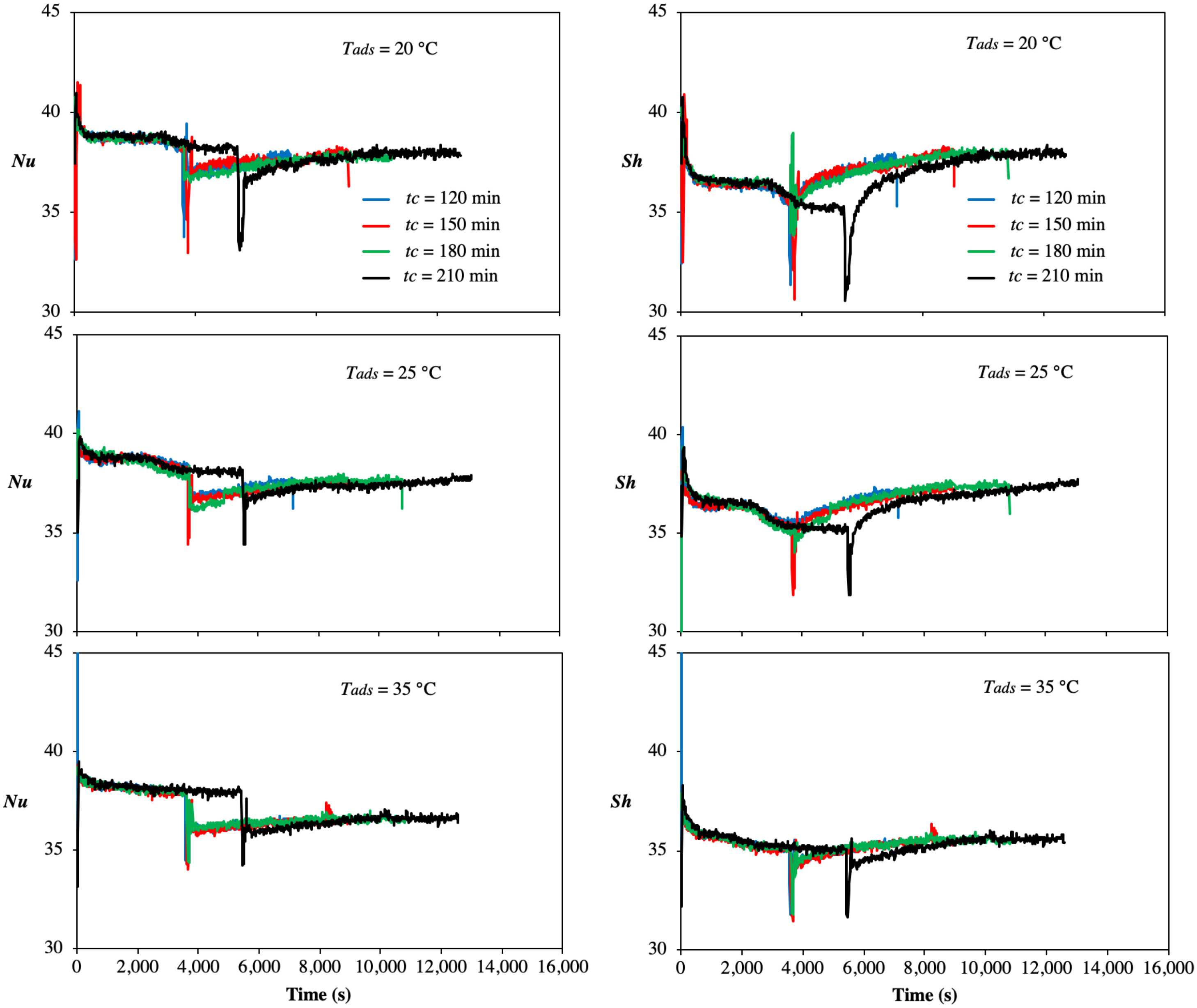

(a) (b)

Figure 3.2. Characteristics of the desiccant dehumidification system at various adsorption temperatures (a) *Nu*; (b) *Sh*.

Figure 3.2 (a) shows that the difference between *Nu* of the desorption and adsorption processes increases with increasing adsorption temperature (T_{ads}) from 20 ºC to 35 ºC. The reason behind this behavior is that the heat released from the hot air to the desiccant material under the constant desorption temperature (T_{des} of 55 ºC) was nearly constant during the experiment. However, when the adsorption temperature (T_{ads}) is increased from 20 ºC to 35 ºC, the temperature difference between the adsorption and desorption processes is reduced, leading to an increase of the gap between the *Nu* of adsorption and desorption processes. The mass transfer characteristics in Fig. 3.2 (b) show that the *Sh* has similar behavior to that of the *Nu*. The value of *Sh* depends on the mass diffusion of water vapor. With increasing air temperature at the adsorption process, the mass diffusivity also increases, leading to a decrease of the *Sh*. Regarding the temperature profiles of the air, interface, and desiccant wall, as depicted in Figs. 3.3 (a), (b), (c), and (d), higher adsorption temperature provides a lower temperature difference between the air and interface temperature, which yields a low value of *Nu*. Hence, the gap of the *Nu* between the adsorption and desorption processes is higher at high adsorption temperature. In the case of the *Sh*, increasing the air temperature leads to an increase of the relative humidity because the saturation vapor pressure of the gas interface increases with the temperature (Zhang et al.). However, when exposing the cold and humid air in the desiccant material, a high temperature gives a low humidity ratio, which results in low water content. Finally, high adsorption temperature yields a low *Sh*, as shown in Fig. 3.2 (b).

Finding the temperature profile directly from the experimental data was very difficult. The properties were solved by using an iteration method. All the properties during the adsorption and desorption processes were considered. The details of the iteration methods follow:

The temperature profile was evaluated based on the thermal resistance between the air and desiccant, as shown in Fig. 3.1. The heat transfer rate of the air side (Q_a) also can be calculated based on the air inlet ($T_{a,in}$) and outlet ($T_{a,out}$) temperatures:

$$Q_a = \dot{m}_a c_{p,a} (T_{a,in} - T_{a,out}) \tag{32}$$

From Fig. 3.1, the energy balance between the air and the adsorbent can be rewritten as follows:

$$Q_{conv,air} = Q_{cond,des} + Q_{ads} \tag{33}$$

$$h_a A \Delta T_a = \frac{k_d A}{\delta} \Delta T_d + M_v \Delta H_{ads} \tag{34}$$

By using the boundary condition of the system indicated by the red line in Fig. 3.1, Eq. 34 can be solved as below:

For the air side:

For the desorption process: $T_i < T_a$ and vice-versa for adsorption process

For the desiccant side:

For the desorption process: $T_i > T_d$ and vice-versa for adsorption process

The half thickness of desiccant material: $0 \le y \le \delta$

Additionally, these general modeling carries their own limitations by the properties of the working fluid and desiccant material. The model can depend sensitively on the convective heat transfer coefficient of the fluid (h), the thermal conductivity of the material (k_d) and heat of adsorption (ΔH_{ads}).

The validity of the value obtained from the iteration was verified by the following expression:

$$\left[h_a (T_a - T_i) - \frac{k_d}{\delta} (T_i - T_d) \right] A_{tot} = M_v \Delta H_{ads} \tag{35}$$

We found that the differences between the heat transfer rates of the air and the desiccant were less than 5%, thus the temperature values obtained from the iteration were valid. The temperature obtained from the iteration was used to evaluate the heat and mass transfer characteristics of the desiccant dehumidification system.

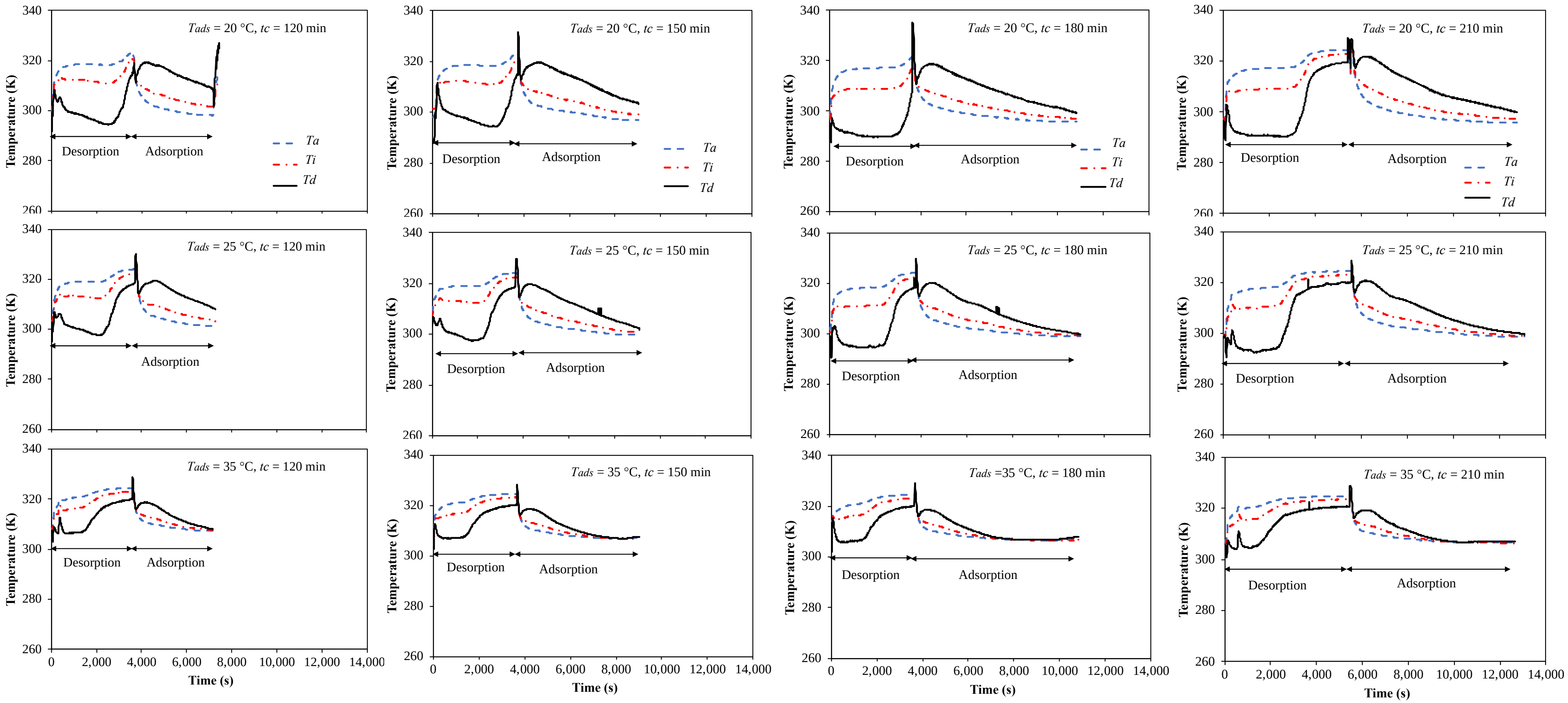

(a) (b) (c) (d)

Figure 3.3. Temperature profiles during the experiments at various desorption temperatures under similar cycle times (t_c) (a) 120; (b) 150; (c) 180; (d) 210.

Figures 3.3 (a), (b), (c), and (d) also clearly illustrate the reason behind the tendencies of *Nu* and *Sh*. As shown in Figs. 3.3 (a), (b), (c), and (d), each adsorption temperature has a similar temperature difference during the experiment, although it was investigated under different switching times. Thus, for each adsorption temperature, the values of *Nu* and *Sh* for different switching times were nearly constants. The highest average *Nu* was 38.02 for T_{ads} of 20 ºC, t_c of 120 min. For the *Sh*, the highest average value was 36.61 for T_{ads} of 20 ºC, t_c of 120 min.

3.3.2. Effect of Switching Time on the Heat and Mass Transfer Characteristics

Figures 3.4 (a) and (b) show the heat and mass transfer characteristics of the desiccant dehumidification system with respect to switching time. The figures show that the Nusselt number (*Nu*) and Sherwood number (*Sh*) have similar trends for all cases. Based on Fig. 3.4 (a), under constant switching time, it is clear that the values of *Nu* were significantly changed for different adsorption temperature. The potential of heat transfer during the adsorption process was higher when the air temperature of the adsorption was low, and the desorption air temperature remained constant. Sensible heat played an important role for controlling the heat transfer rate between the air and desiccant material. From Fig. 3.4 (a), it can also be observed, that in the desorption process, the *Nu* lines are nearly constant. However, when the desorption process is almost finished, the value of *Nu* is decreased until the adsorption process starts. This phenomenon always occurs when the time is switched from the desorption to the adsorption process. The temperature and pressure of the surface of the material suddenly change within this period. Thus, proper selection of switching time is very important to avoid the temperature decrease and overload pressure (Hong et al., 2016).

Figure 3.4 (b) shows the values of *Sh* with a variation of switching time for the adsorption temperatures of 20 ºC, 25 ºC, and 35 ºC. The value of *Sh* does not vary with the change of switching time. However, under constant switching time, the *Sh* changes considerably with the temperature variation. For mass transport, the key point is that the mass adsorbed during the adsorption phase must be equal to the mass desorbed during desorption phase (Hamed, 2003). The characteristics pertaining to the variation of the switching time can be explained further by the temperature profiles shown in Figs. 3.5 (a), (b), and (c). These figures show that the time for completing the desorption process was similar for each adsorption temperature.

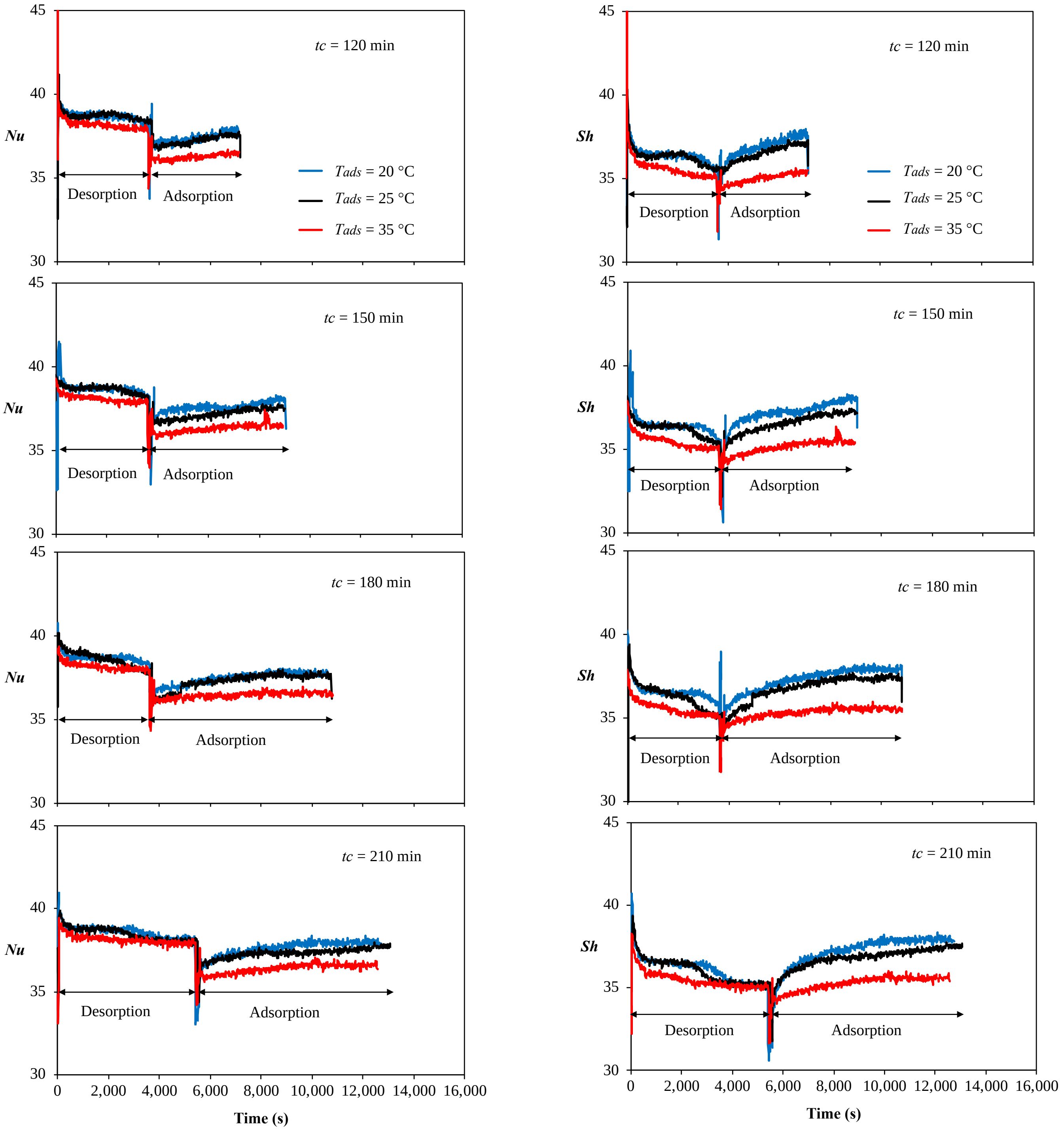

(a) (b)

Figure 3.4. Characteristics of the desiccant dehumidification system at various switching times (a) *Nu*; (b) *Sh*.

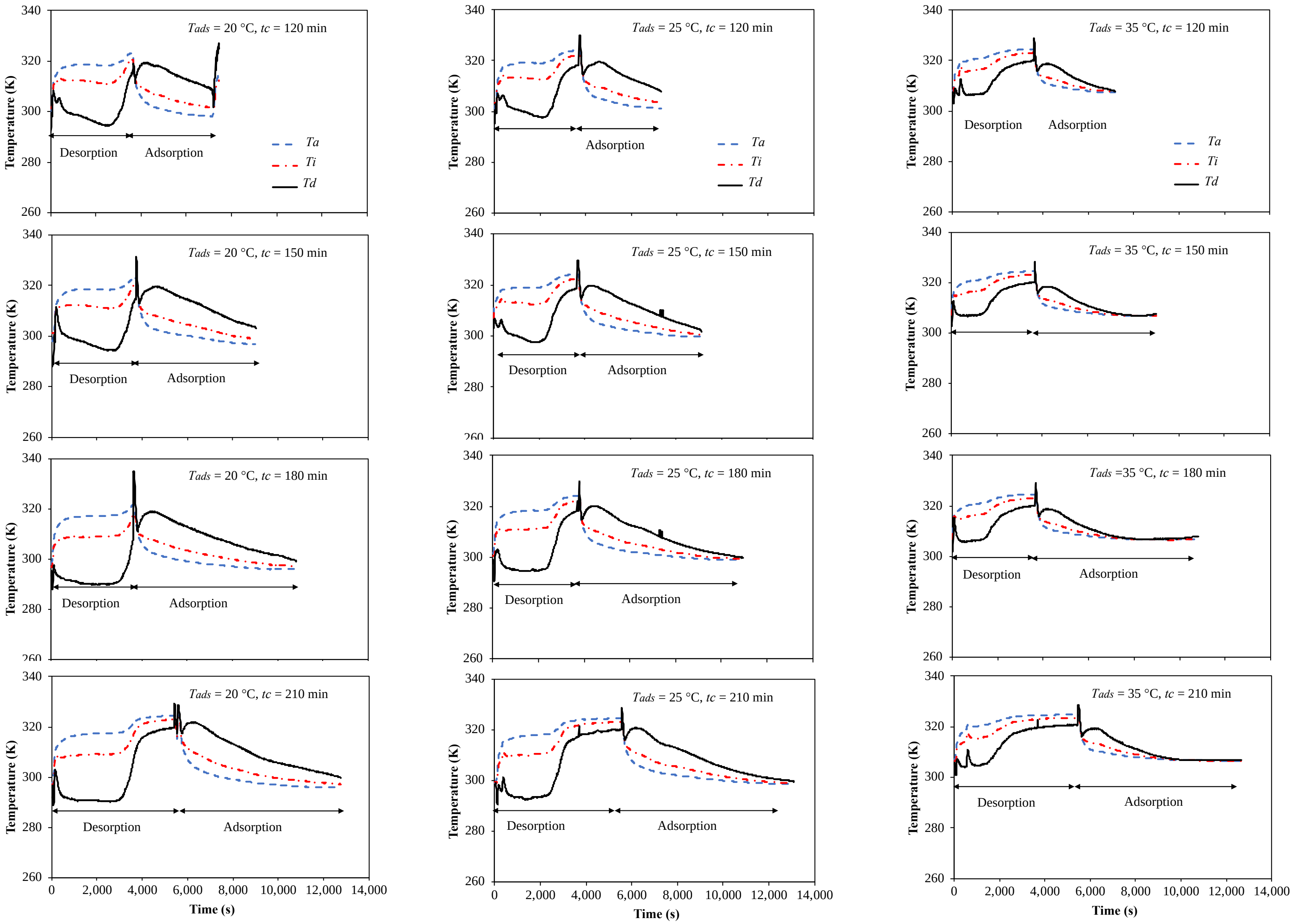

(a) (b) (c)

Figure 3.5. Temperature profiles during the experiments at various cycle times under similar adsorption temperature (T_{ads}) (a) 20 ºC; (b) 25 ºC; (c) 35 ºC.

When comparing Figs. 3.5 (a), (b), and (c), it is apparent that the highest adsorption temperature provides the advantage that the desorption process can finish earlier than for the other variations. Consequently, it can reduce the energy required for heating the adsorption material. Based on the results of the study, we can define the adsorption time as the time required for the desiccant block to adsorb the water vapor from the process air, whereas desorption time is the time needed for the desiccant block to release the water vapor concentration. Both the processes allow heat and mass transfer between the process air and the surface of the desiccant material. Additionally, completion of adsorption/desorption is revealed when the capability of the desiccant material to adsorb/desorb the water vapor concentration approaches a limit (humidity ratio inlet is equal to humidity ratio outlet). Different from the case of the desiccant wheel, the switching time for the honeycomb desiccant block is a significantly important parameter for ensuring continuous functioning of the system. Thus, selecting a proper switching time is very important for estimating the time when each process will finish.

3.3.3. Adsorption rate

Figures 3.6 and 3.7 show the adsorption rate with respect to adsorption temperature and switching time, respectively. In all cases, the adsorption characteristic shows a similar trend of adsorption rate. Figure 3.6 shows that the adsorption rate varied slightly with variation of switching time when the adsorption temperature (T_{ads}) was 20 ºC, whereas for the others, the adsorption values were nearly constant. As shown in Fig. 3.7, the adsorption rate is higher when the adsorption temperature is lower. This clearly shows that the influence of the adsorption temperature is more prominent than the influence of the switching time. The adsorption rate depends mainly on the adsorption uptake as shown in Eq. 21. While the adsorption uptake is showing the function of the pressure and temperature. When the desiccant material and water vapor was in contact, not only the temperature and pressure but also mass will change during the process. The pressure change causing the rapid rate of the adsorption uptake of the water vapor, because the desiccant material was at conditions far from the equilibrium. This pressure change affected the mass transfer of the water vapor through the pores of the desiccant material. When it reaches the equilibrium state, no more water vapor was desorbed or adsorbed by the desiccant material. Thus, the adsorption rate becomes low in the end of the desorption or adsorption process as shown in Figs 3.6 and 3.7. Besides the change of the temperature and pressure, the adsorption rate also depends on the isosteric heat of the adsorption which is the function of the temperature, pressure and pore size (Sun and Chakraborty, 2004; 2014). The highest adsorption rate was 0.00809 kg/kg.s for T_{ads} of 20 ºC, t_c of 210 min.

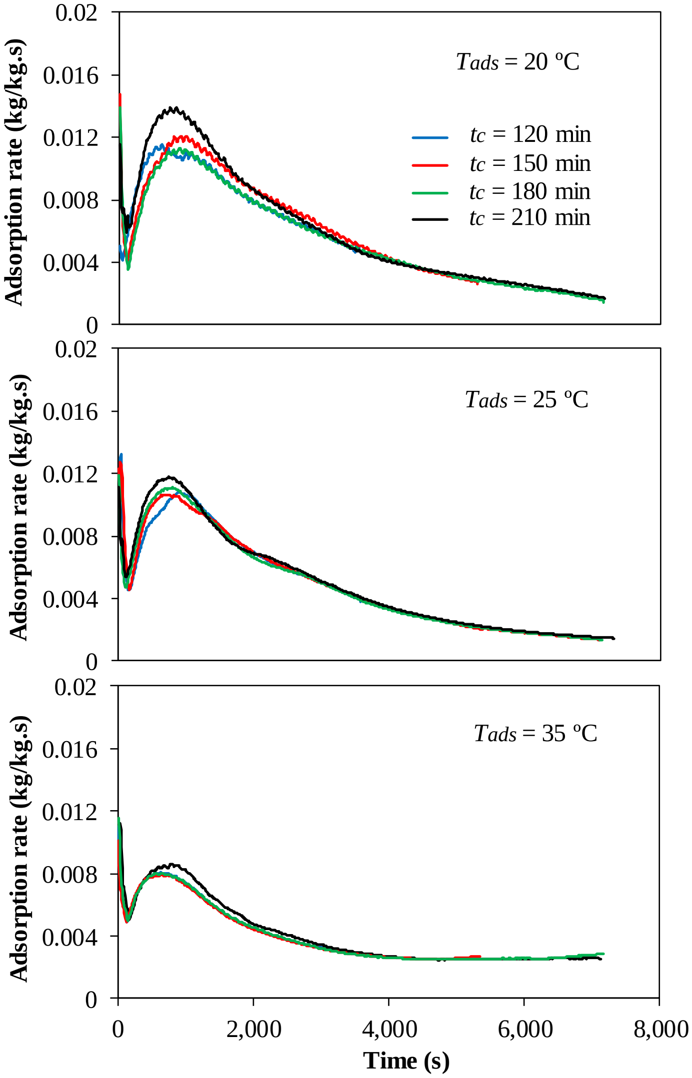

Figure 3.6. Adsorption rate of the desiccant dehumidification system at various adsorption temperatures.

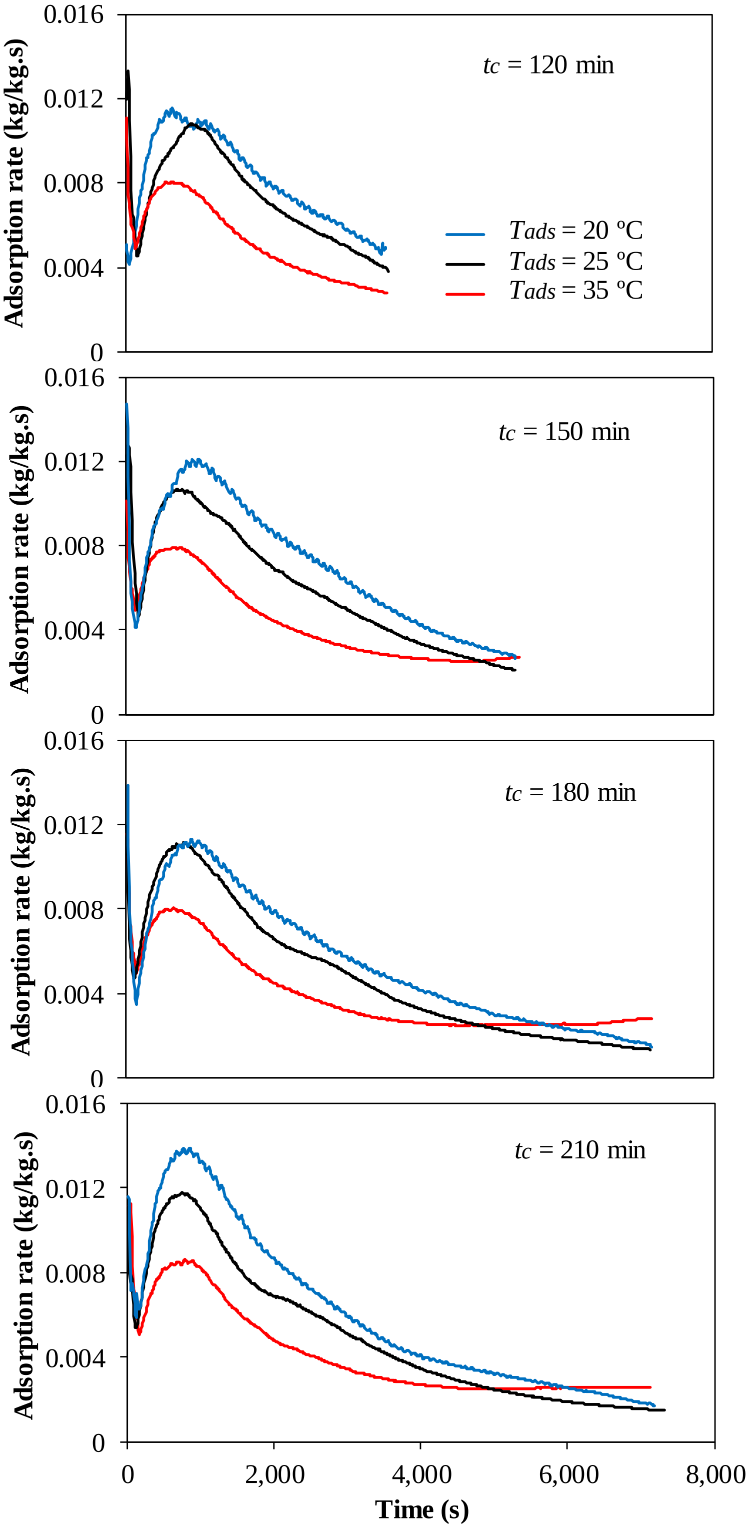

Figure 3.7. Adsorption rate of the desiccant dehumidification system at various switching times.

3.3.4. Empirical Correlation for Heat and Mass Transfer

The empirical correlations for the non-dimensional parameters were developed using the independent variables of Reynolds number (*Re*) and Prandtl number (*Pr*) for Nusselt number (*Nu*) and *Re* and Schmidt number (*Sc*) for Sherwood number (*Sh*). It is developed by the experimental data obtained for the adsorption temperature (T_{ads}) of 20 ºC, 25 ºC, and 35 ºC with switching time (τ) variation of 60:60 min, 60:90 min, 60:120 min, and 90:120 min. The proposed empirical correlations follow:

$$Nu = 0.147\ Re^{0.98} Pr^{0.3} \tag{36}$$

$$Sh = 0.611\ Re^{1.323} Sc^{0.3} \tag{37}$$

for Re < 600

The predicted data derived from the empirical correlations are compared with the experimental results in Figs. 3.8 (a) and (b). For all conditions, the relative deviation between the experimental data and the predictive data was ±12.17% for the Nusselt number (*Nu*) and ±12.2% for the Sherwood number (*Sh*). It was found that the predicted values were not very different from the experimental data. From these results, we can suggest that the correlation can also be used for other desiccant systems.

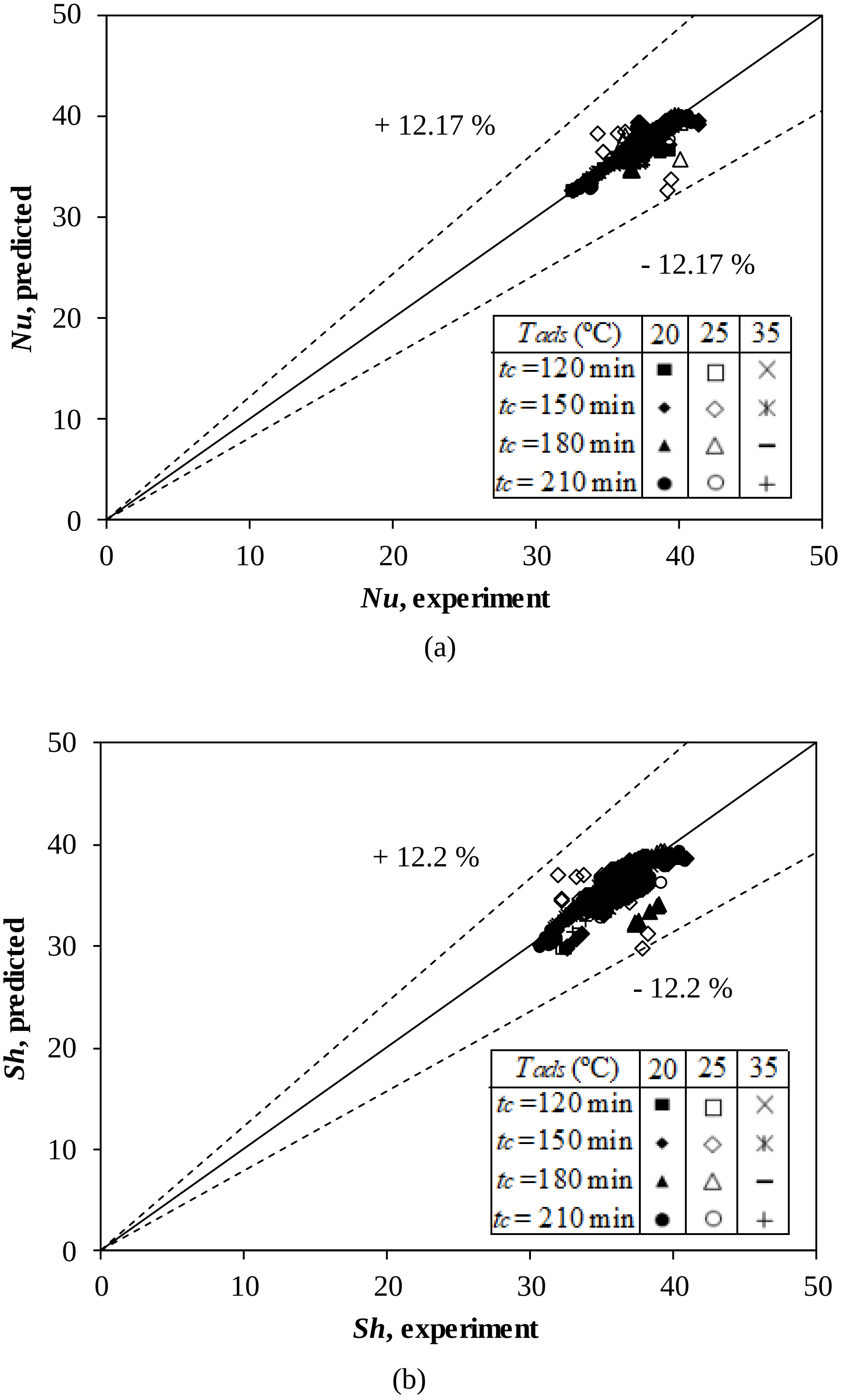

Figure 3.8. Comparison of the experimental and predicted data (a) *Nu*; (b) *Sh*.

3.4 Conclusions

Heat and mass transfer characteristics of the desiccant dehumidification system were investigated experimentally. Three different adsorption temperatures (T_{ads}), 20 ºC, 25 ºC, and 35 ºC, were investigated under the various switching time (τ) values of 60:60 min, 60:90 min, 60:120 min, and 90:120 min, respectively. Correlations for predicting the heat and mass transfer characteristics of the system were also developed based on the experimental data results. Several conclusions can be drawn based on the experimental results. The Nusselt number (*Nu*) and Sherwood number (*Sh*) of the desiccant dehumidification system did not vary with the variation of switching time. However, the temperature variation showed a significant effect on *Nu* and *Sh*. *Nu* and *Sh* tended to decrease with the increase of adsorption temperature. From the details of the calculation, there is a close relation between the *Nu* and *Sh* inside the desiccant system. It must be ensured that the calculation of the heat transfer (*Nu*) includes the change of the humidity ratio as latent heat. The change of the humidity ratio also takes part in the calculation of the mass transfer (*Sh*). Additionally, switching time is very important to ensure the continuous functioning of the system, even though it does not give very different results for *Nu* and *Sh* under the parameters investigated. Properly selecting the time for each mode can improve the effectiveness of the system. Considering application for a dehumidifier, high switching time, which gives a high desorption rate, is better. High desorption rate is important for the system to have high ability for removing moisture. The empirical correlations in terms of *Nu* and *Sh* are in good agreement with measurement, with a deviation of less than 15% for each.

Nomenclature

A	area of adsorption (m^2)
A_a	air channel surface area (m^2)
A_d	desiccant surface area (m^2)
$c_{p,a}$	specific heat capacity of the air (kJ/kg.K)
$c_{p,b}$	specific heat capacity of the bed (kJ/kg.K)

C	GAB model constant related to heat
C_o	adjustable constant GAB model for temperature effect (kJ/kg)
D_h	hydraulic diameter of the air channel (m)
D_e	surface diffusion coefficient (m^2/s)
D_{va}	coefficient of mass diffusion for water vapor (kg/m^2s)
$\frac{dW}{dt}$	adsorption rate (kg/kg.s)
h	channel height for air layer (m)
h_a	convective heat transfer coefficient of the air (W/m^2K)
H	honeycomb height (m)
ΔH_{ads}	adsorption heat (kJ/kg)
ΔH_c	function related to water sorption heat (kJ/kg)
ΔH_k	function related to water sorption heat (kJ/kg)
k	thermal conductivity of the air (W/mK)
k_d	thermal conductivity of the desiccant material (W/mK)
k_m	average of overall mass transfer coefficient (kg/m^2s)
$k_{m,a}$	mass transfer coefficient of the air (kg/m^2s)
$k_{m,d}$	mass transfer coefficient of the desiccant side (kg/m^2s)
L	honeycomb length (m)
Le	Lewis number
M_v	overall mass transfer rate (kg/s)

$M_{v,a}$	mass transfer rate of the air (kg/s)
$M_{v,d}$	mass transfer rate of the desiccant (kg/s)
Nu	Nusselt number
p	fin spacing (m)
P	atmospheric pressure (Pa)
Pr	Prandtl number
P_s	saturation water vapor pressure (Pa)
P/P_o	relative pressure
Q_a	heat transfer for air channel (W)
Q_{ads}	heat transfer due to heat of adsorption (W)
$Q_{conv,air}$	convective heat transfer of the air (W)
$Q_{cond,des}$	conductive heat transfer of the desiccant wall (W)
Q_d	heat transfer for desiccant side (W)
R	radius of the adsorbent particle (m)
R_g	specific gas constant for water (kJ/kg.K)
Re	Reynolds number
R_h	thermal resistance for convection
R_k	thermal resistance
$R_{m,a}$	mass resistance of the air channel
$R_{m,k}$	mass resistance of the desiccant wall

Sc	Schmidt number
Sh	Sherwood number
V	air velocity (m/s)
W	honeycomb width (m)
W_{eq}	equilibrium adsorption uptake (kg/kg)
w	instantaneous adsorption uptake (kg/kg)
X_a	humidity ratio of the air (kg/kg)
$X_{a,o}$	outlet humidity of the air (kg/kg)
X_d	humidity ratio of the desiccant (kg/kg)
X_i	humidity ratio of interface (kg/kg)
X_{max}	maximum humidity (kg/kg)
X_{min}	minimum humidity (kg/kg)
T_a	bulk air temperature (K)
T_d	desiccant wall temperature (K)
T_i	interface temperature (K)

Greek Symbols

α	thermal-diffusion coefficient (m^2/s)
ε	porosity
δ	half-thickness of desiccant wall (m)

ρ_a	density of the air (kg/m^3)
ρ_b	density of the bed (kg/m^3)
μ	dynamic viscosity of the air (kg/m.s)
φ	relative humidity (%)

References

Criptoph, R. E., Forced convection enhancement of adsorption cycles, Heat Recov Syst CHP. 14 (1994) 343-350.

Criptoph, R. E., Holland, M. K., Turner, L., Contact resistance in air-cooled plate fin-tube air-conditioning condensers, Int. J. Refrig. 19 (1996) 400-406.

Eun, T., Song, H., Han, J. H., Lee, K., Kim, K., Enhancement of heat and mass transfer in silica-expanded graphite composite blocks for adsorption heat pumps. Part II. Cooling system using the composite blocks, Int. J. Refrig. 23 (2000) 74-81. Eckert, E. R. G., Drake, R. M., Analysis of heat and mass transfer, McGraw-Hill, New York, 1972.

Fedorov, A. G., Viskanta, R., Analysis of transient heat/ mass transfer and adsorption/desorption interactions, Int. J. Heat Mass Trans. 42 (1999) 803-819.

Fu, H., Yang, Q., Zhang, L., Effects of material properties on heat and mass transfer in honeycomb-type adsorbent wheels for total heat recovery, Appl. Therm. Eng. 118 (2017) 345-356.

Glueckauf, E., Coates, J. I., Theory of chromatography. Part IV. The influence of incomplete equilibrium on the front boundary of chromatograms and on the effectiveness of separation, J. Chem. Soc. (1947) 1315.

Hamed, A. M., Desorption characteristics of desiccant bed for solar dehumidification/ humidification air conditioning system, Renew. Energ. 28 (2003) 2099-2111.

Hong, S. W., Kwon, O. K., Chung, J. D., Effect of the switching time on the performance of an adsorption chiller, J. Mech. Sci. Technol. 30 (5) (2016) 2387-2395.

Kim, D., Koyama, S., Kuwahara, K., Kwon, J., Park, B., Study on heat and mass transfer characteristics of humid air-flow in a fin bundle, Int. J. Refrig. 33 (2010) 1434-1443.

Li, A., Thu, K., Ismail, A. B., Ng, K. C., A heat transfer correlation for transient vapor uptake of powdered adsorbent embedded onto the fins heat exchangers, Appl. Therm. Eng. 93 (2016) 668-677.

Li, Z., Michiyuki, S., Takeshi, F., Experimental study on heat and mass transfer characteristics for a desiccant-coated fin-tube heat exchanger, Int. J. Heat Mass Trans. 89 (2015) 641-651.

Majumdar, P., Heat and mass transfer in composite desiccant pore structure for dehumidification, Sol. Energy. 62 (1998) 1-10.

Miyazaki, T., Akisawa, A., The influence of heat exchanger parameters on the optimum cycle time of adsorption chillers, Appl. Therm. Eng. 29 (2009) 2708-2712.

Naphon, P., On the performance of air conditioner with heat pipe for cooling air in the condenser, Energy Convers. Manag. 51 (2010) 2362-2366.

Nóbrega, C.E.L., Brum, N.C.L., An analysis of the heat and mass transfer roles in air dehumidification by solid desiccants, Energy and Buildings 50 (2012) 251-258.

Restuccia, G., Freni, A., Maggio, G., A zeolite-coated bed for air conditioning adsorption systems: parametric study of heat and mass transfer by dynamic simulation, Appl. Therm. Eng. 22 (2002) 619-630.

Sphaier, L.A., Worek, W. M., Analysis of heat and mass transfer in porous sorbents used in rotary generators, Int. J. Heat Mass Trans. 47 (2004) 3415-3430.

Sultan, M., El-Sharkawy, I. I., Miyazaki, T., Saha, B. B., Koyama, S., Maruyama, T., Maeda, S., Nakamura T., Water vapor sorption kinetics of polymer based sorbent: Theory and experiments, Appl. Therm. Eng. 106 (2016) 192-202.

Sultan, M., Miyazaki, T., Koyama, S., Zahid, M. K., Performance evaluation of hydrophilic organic sorbents for desiccant air-conditioning applications, Adsorption Science and Technology 0 (0) (2017) 1-16.

Sun, B., Chakraborty, A., Thermodynamics frameworks of adsorption kinetics modelling: Dynamic water uptakes on silica gel for adsorption cooling applications, Energy 84 (2004) 296-302.

Sun, B., Chakraborty, A., Thermodynamic formalism of water uptakes on solid porous adsorbents for adsorption cooling applications, Appl. Phys. Lett. 104 201901 (2014).

Sommers, A. D., Jacobi, A. M., Air-side heat transfer enhancement of a refrigerator evaporator using vortex generation, Int. J. Refrig. 28 (2005) 1006-1017.

Wang, R. Z., Xia, Z. Z., Wang, L. W., Lu, Z. S., Li, S. L., Li, T. X., Wu, J. Y., He, S., Heat transfer design in adsorption refrigeration systems for efficient use of low-grade thermal energy, Energy. 36 (2011) 5425-5439.

Yanagi, H., Ino, N., Heat and mass transfer characteristics in consolidated silica gel/ water adsorption-cooling system, ASME ASIA Congress and Exhibition (1997) 1-7.

Zalewski, W., Gryglaszewski, P. A., Mathematical model of heat and mass transfer processes in evaporative fluid coolers, Chem. Eng. Process. 36 (1997) 271-280.

Zhang, T., Liu, X., Zhang, L., Jiang, Y., Match properties of heat transfer and coupled heat and mass transfer processes in air conditioning system, Energy Convers. Manag. 59 (2012) 103-113.

Zhang, Z., Kim, C. S., Kleinstreuer, C. Water vapor transport and its effects on the deposition of hygroscopic droplets in a human upper airway model, Aerosol Science and Technology 40 (1) (2006) 1-16.

Zhao, Y., Dai, Y. J., Ge, T. S., Sun, X.Y., Wang, R. Z., On heat and moisture transfer characteristics of a desiccant dehumidification unit using fin tube heat exchanger with silica gel coating, Appl. Therm. Eng. 91 (2015) 308-317.

CHAPTER 4

Chapter 4

PERFORMANCE OF DESICCANT DEHUMIDIFICATION SYSTEM

This chapter highlights the performance of the desiccant dehumidification system. Low desorption air temperatures were given at 35 ºC, 45 ºC, 55 ºC, and 65 ºC. Their important influence was analyzed in terms of dehumidification ability, latent heat ratio, and latent effectiveness. The investigation was performed under a maintained adsorption temperature and air mass flow rate of 20 ºC and 0.1 kg/s, respectively. The system utilized a polymer desiccant material. The time ratio for desorption and adsorption were remained constant at 60 minutes for desorption and 120 minutes for adsorption. Results show that with the increased desorption temperature the latent heat ratio decreases, whereas the dehumidification ability and latent effectiveness increases. Along with the system, the high desorption air temperature gives an insignificant effect on the system performance, but it is noteworthy on the moisture removal ability. The highest latent heat ratio was found in the value of 0.61 at desorption temperature of 35 ºC, while the highest latent effectiveness was obtained at desorption temperature of 65 ºC. Referring to the results, an appropriate desorption temperature to obtain proper performance was found at 55 ºC.

4.1 Introduction

Adjusting the temperature and humidity, basically, are dealt with the latent and sensible heat. Recently, the rapid development of air conditioning technology is moving towards to handle latent and sensible heat separately. One of the challenges of effective air conditioning system comes from the desiccant air conditioning system. Shelpuk (1993) provided a review in technical challenges using solid desiccant for air conditioning and dehumidification system.

Their potential was described through the environmental and energy concern. The step progress of the solid desiccant including the material and component geometries, improvement of the performance by considering the cost of the system, and the new design of the system for identifying the new concept. Considering the building indoor air quality, the solid desiccant had great potential as an air conditioning device. Which could provide better air quality and also environmentally friendly due to the reduction of using the chlorofluorocarbon and greenhouses gases.

The development of the air dehumidification system by using membrane air-liquid contractor was investigated by Isetti et al., 1997. Microfiber polyethylene membrane was utilized as the porous barrier between the hygroscopic solution and moist air. Based on their results, there was feasibility from their study to employ the membrane as the absorber and desorber unit in the air conditioning unit. The used of moderate temperature (310-330 K) for the desiccant reactivation offered more energy saving for their system. Hamamoto et al. (2008) numerically studied the dehumidification performance of the desiccant rotor by low-grade thermal energy. Low-Grade thermal energy around 60 ^{o}C was applied to the system. Development of the desiccant rotor was conducted to achieve high performance of the system. The changes in the regeneration temperature were evaluated to find the proper temperature. For each design, they found that the required regeneration temperature was different. It depends on the geometry of the rotor. The improvement of the desiccant wheels performance which driven by a low regeneration temperature was also investigated by White et al., 2011. Two different materials, called zeolite and super adsorbent polymer were evaluated and compared with the silica gel. Their results show that each material offered different behavior towards dehumidification ability. For low regeneration temperature (50 ^{o}C) with high relative humidity, the proper material was a super adsorbent polymer. Tsujiguchi et al. (2017) studied the feasibility of the desiccant dehumidification wheel for the simultaneous operation of the heating and dehumidification by humidity swing adsorption. The desiccant wheel was made from a ceramic paper-based honeycomb matrix impregnated with silica gel by 50%wt. Low humidity and temperature of the regeneration were employed to drive the system. By combining the parameters including the rotation speed of the desiccant wheel, air velocity, humidity and temperature of the air, they found that for obtaining the heating effect, the system should be driven by the minimum temperature of the regeneration of 13 °C. They also confirmed that the humidity swing adsorption (only based on the humidity difference) was successfully driven the system. The effect of the main parameters of the desiccant wheel dehumidification system was conducted by Alahmer et al. (2018) to evaluate the performance of the system. Humidity ratio, temperature, flow rate, ratio of the reactivation to process air flow, and rotational speed were considered as the main parameters which affected the moisture removal ability within the system. Two desiccant materials were compared namely wound silica gel and molecular sieve. Under their experiment conditions, with the variation of regeneration temperature by 70 °C, they found that their system offered the moisture removal ability of 2.065 g/kg. They also confirmed that the regeneration temperature significantly affected the performance of the system not only the moisture removal ability but also the coefficient performance of the system (COP). Fong and Lee (2018) investigated the performance of the desiccant wheel under three different desiccant materials. An RD silica gel, AQSOA-Z02, and CECA-3A were utilized to estimate the capability of the system for reducing the humidity ratio. Based on their results, under regeneration temperature of 50 °C, they found that the humidity ratio reduced by 33%, 22.6%, and 18.7% respectively for RD silica gel, AQSOA-Z02, and CECA-3A.

Though the desiccant dehumidification system offers so many advantages, its performance still low as compared to the traditional vapor compression system. From this motivation, we conduct an experimental study on the desiccant dehumidification system to investigate the thermal performance including the latent heat ratio and latent heat effectiveness. In some literature, they have been provided the experimental and numerical study by considering the performance investigation of the desiccant dehumidification system. The effect of the regeneration conditions on the adsorption dehumidification process in packed silica gel beds was conducted by Chang et al., 2004. The regeneration temperature and regeneration time were considered as the parameters to observe the moisture adsorption in packed silica beds. By comparing two kinds of silica gel, they found that the amount of adsorption in an adsorbent was affected by the degree of adsorbent regeneration. Moreover, they stated that high temperature and long process of the regeneration was not compulsory to reach specific moisture uptake. Mass transfer resistance was the important aspect of this behavior. The thinner mass transfer resistance, the good saving energy is. The effect of regeneration mode on the performance of liquid desiccant packed bed regenerator was also conducted by Liu et al., 2009. They have stated that the regeneration side was one of the most important components in liquid desiccant air-conditioning. Other important parameters were also investigated by Chung et al., 2009. The optimization of the desiccant wheel was conducted by considering the wheel speed and area ratio as a function of regeneration temperature. The evaluation was done by calculating the wheel performance by means of its moisture removal capacity (MRC). The effect of the regeneration air temperature and humidity also studied by Zhang et al. (2014). COP, specific dehumidification power (SDP) and dehumidification efficiency were examined for various desiccant materials. They reported that higher regeneration air temperature gives no significant effect on COP. However, in dry condition, COP decrease with increasing regeneration air temperature. Sayilgan et al (2016) was determined the effect of regeneration temperature on adsorption equilibria and mass diffusivity of zeolite 13x-water pair. The adsorption temperature was adjusted in the value of 35 ºC, 45 ºC, and 60 ºC for the desorption temperature of 90 ºC. They found that the adsorption capacity increased from 22% (kg/kg) to 24% (kg/kg) when the desorption temperature was increased from 90 ºC to 150 ºC.

Kabel (2009) evaluated theoretically and experimentally the impact of packed bed length on the performance of the multilayer desiccant packed bed system. The experiment was conducted under different air velocity, humidity, and temperature of the adsorption and desorption process for transient conditions. They found that each parameter performed a different effect on the performance of the system. Air velocity and humidity ratio offer a significant effect on the accumulated adsorbed water, while for the inlet temperature of the desorption process influences more on the desorption rates. They also found that adsorption rates decreased by increasing packed bed length. Zheng et al. (2014) reviewed desiccant materials for desiccant cooling systems. The properties of the material including adsorption isotherm for composite desiccants, Nanoporous inorganic materials, and polymeric desiccants were clarified and compared. They found that the properties of the materials influenced the dehumidification and regeneration capacity. The effect of the switching time on the performance of the fin-tube type adsorption chiller was numerically investigated by Hong et al., 2016. They examined the performance in terms of the COP and the SCP. Switching time parameter was adjusted for heating and cooling phases. Three different switching time parameters (no switching time; optimal switching time and double the optimal switching time) were investigated for different fin pitches, fin heights and heating temperatures. Their results show that the COP decrease with increasing fin pitch and fin height. At the same time, decreasing fin pitch and fin height and increasing heating temperature reveals the decrease of SCP value. Additionally, they also found that the heating phase was completed earlier than the cooling phase. The switching time should be long enough to obtain optimum performance.

Tu et al. (2017) developed desiccant-enhanced direct expansion heat pump (DDX HP) based on water-sorbing heat exchanger (WSHE) for achieving high energy efficiency. Their proposed system can be used for dehumidifying and cooling by handling sensible heat and latent heat separately. It can control the temperature and humidity by adjusting the evaporation temperature, and adsorption/ desorption duration, respectively. Under a considerable parameter, they found that their system has high COP in the value of 6.2 for summer conditions. Their satisfying performance was also shown by their ability to achieve appropriate temperature and humidity into a conditioned space without affecting cost and compactness of the system. Wu et al. (2018) presented a review on the substrate of solid dehumidification system. They compared between the rotary and non-rotary solid desiccant system. They found that besides selecting proper materials, choosing a substrate with high porosity also very important to improve the dehumidification capacity. Additionally, the substrate with high thermal conductivity should be selected for a rotary desiccant wheel. While for non-rotary solid desiccant dehumidification system the proper selection of substrate reduces the difficulties of designing the structure of the dehumidification system. They also found that the best substrate for the rotary desiccant wheel was the porous fiber paper.

In a sharp view, the focus of the aforementioned literature was the parameters which could affect the performance of the desiccant dehumidification system. The effective system can be achieved by adjusting the properties of the air, materials and the system itself. The properties of the air included temperature, humidity ratio, and velocity. The variable of material involved the adsorption isotherm and kinetics of the material while the system emphasized the breakthrough time of the adsorption and desorption processes (switching time). To clearly distinguish the effect of the parameter in the present system, especially for dehumidification, we performed an experimental study on the potency of the polymer as adsorbent material for air conditioning. The main objective of this study is to find the dehumidification ability of the system by calculating the amount of dehumidification, effectiveness factor and latent heat performance of the system.

4.2 Experimental Methods

4.3.1. Experimental Facility

The test apparatus of the desiccant dehumidification system was represented in detail in Chapter 1. The adsorption and desorption air processes were supplied by using two different air supply units. In the case of desorption air supply unit, the device also equipped with the temperature and relative humidity controller which allow adjusting the temperature and humidity ratio of the desorption air inlet. However, the environmental conditions including the relative humidity and temperature were controlled by adjusting the relative humidity and temperature of the chamber. During the experiment, the environmental conditions were kept constant at the temperature and relative humidity of 25 °C and 65%, respectively. The experiment was measured at various desorption temperatures (T_{des}) of 35 °C, 45 °C, and 55 °C with relative humidity inlet of 35%, 20%, 15%, and 9%, respectively for the adjusted desorption temperatures. While the adsorption temperature (T_{ads}) was unchanged in the value of 20 °C. For all variations of the mass flow rate was kept constant in the value of 0.1 kg/s.

The working principle of the desiccant dehumidifier system is as follow:

(1) Firstly, the desiccant material is heated by the hot air which provides by air supply unit for the desorption phase. This process allowed the water vapor molecules which trapped in the desiccant material to evaporate. Therefore, the desiccant material is regenerated and recovered the ability of moisture adsorption.

(2) When the desiccant material reaches the equilibrium, the process is switched into the adsorption process. The desiccant material adsorbs the water vapor molecules. In the same time, in the interface of the desiccant material, the heat of adsorption is released.

(3) Lastly, the process is repeated for three up to four cycles to obtain adequate data.

4.3.2. Experimental data analysis

Data collections were provided in the term of execution for temperature inlet-outlet, relative humidity inlet-outlet and the pressure difference between inlet-outlet of the air stream. All data were collected for every 10 seconds by data logger DAQMASTER: MX 100. Since we have four cycles of data, the last cycle data was applied to evaluate and analyze the results. Performance indices of the system were evaluated by the following terms:

1) Dehumidification index

To characterize the dehumidification index, firstly the calculation of adsorption and desorption amount of the desiccant was examined. The amount is defined as the moisture removal capacity which can be considered as the difference between the humidity ratio inlet and humidity ratio outlet. The moisture removal capacity for each process can be calculated by the following expression:

$$d_{ads} = X_{ads,in} - X_{ads,out} \tag{1}$$

for adsorption

$$d_{des} = X_{des,in} - X_{des,out} \tag{2}$$

for desorption

where d is the moisture removal capacity (kg/kg), X_{in} is the humidity ratio of the inlet air (kg/kg), X_{out} is the humidity ratio of the outlet air (kg/kg). While *ads* and *des* indicate the adsorption and desorption processes. For the desorption process because the hot air brings the water vapor during the running of the system so that the outlet humidity is higher than the inlet and the moisture removal becomes negative.

During the adsorption process, the average dehumidification index (D_i) is defined as:

$$D_i = \frac{1}{t}\int_0^t d_{ads}\,dt \tag{3}$$

where *t* is the dehumidification time (s).

2) Latent heat performance

Desiccant dehumidifier system is responsible for handling the moisture so that the performance is evaluated regarding latent heat ratio and latent effectiveness. The latent effectiveness (ε) is obtained as:

$$\varepsilon = \frac{X_{ads,in} - X_{ads,out}}{X_{ads,in} - X_{ideal}} \tag{4}$$

The performance of the desiccant dehumidification system which shows the energy amount is evaluated by using the latent heat ratio (LHR). LHR can be described as the ratio of the latent heat to the total energy (latent and sensible heat) required by the system (Islam et al., 2018). It is given by the following equation:

$$LHR = \frac{Q_{lat}}{Q_{lat} + Q_{sen}} \tag{5}$$

Latent heat (Q_{lat}) is given by:

$$Q_{lat} = Q_{ads} = \Delta d_{ads}\dot{m}_a\gamma = \dot{m}_a(h_{in} - h_{out}) \tag{6}$$

and Sensible heat (Q_{lat}) is given by:

$$Q_{sen} = Q_{des} = m_a c_p (T_{des,in} - T_{des,out}) \tag{7}$$

where Q_{ads} is the average of enthalpy exchange in adsorption process (W), Q_{des} is the average of heat exchange in the desorption process (W), $\dot{m}_a$ is the air mass flow rate (kg/s), h_{in} is the enthalpy of the air inlet, h_{out} is the enthaphy of the air outlet,$\gamma$is latent heat of vaporization (kJ/s), c_p is the specific heat of the air at bulk temperature (kJ/kg.K), $T_{des,in}$ was air inlet temperature of the desorption process (K) and $T_{des,out}$ is the air outlet temperature of the desorption process (K).

4.3 Results and Discussion

4.3.1. The Effect of the Desorption Temperature on the Adsorption/Desorption Amount of the System

Figure 4.1 represents the adsorption/desorption amount for different low desorption temperature of 35 ºC, 45 ºC, 55 ºC, and 65 ºC.

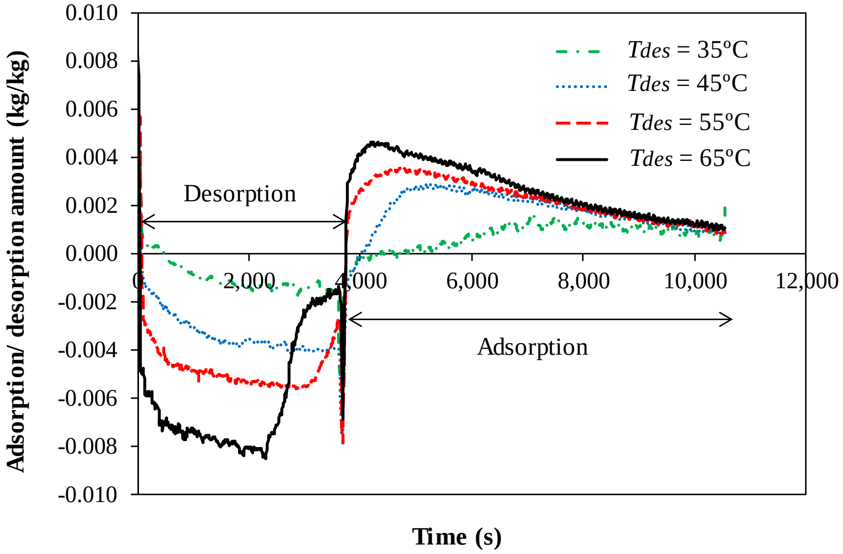

Figure 4.1. Adsorption/desorption amount for different desorption temperature.

In the desorption process, hot and dry air flowing through the desiccant material to capture the moisture from the desiccant material. The recent experiment indicates that the adsorption/desorption amount increases with increasing desorption air temperature. The ability of air to hold the water vapor increases as its temperature increases (Amer et. al, 2009). Consequently, the humidity ratio of the outlet air rises resulting in higher differences between the humidity ratio inlet and outlet. Based on Eqs. (1) and (2), the adsorption/desorption amount will also increase. In Fig. 4.1, both processes show that the rate of adsorption and desorption decreases with the increase of time. In the desorption process, the moisture removal capacity increases rapidly then decrease when the saturation pressure of the process air and the surface of the material becomes equilibrium. The reason for this behavior is that at the beginning of the desorption process, the desiccant material was cooled, and the humidity content was high. Introducing hot and dry airstream into the cool desiccant material reveals high moisture adsorb in the beginning up to a particular time. After that, the gradient of moisture adsorb changes its direction which indicates the conditions nearly reach saturated. For the case of adsorption, the behavior is slightly different from that of the desorption phase. At the beginning of the process, the moisture removal capacity is quite high then gradually decreases and becomes steady. For all cases, the adsorption process finished in a similar point because of the adsorption temperature and switching time unchanging during the process.

Figure 4.1 also shows the different behavior on the desorption side when the temperature increases to the value of 65 ºC. It can be noticed that at high desorption temperature of 65ºC, the desorption phase was completed earlier than the other variation. This behavior is caused by the water vapor sorption kinetics properties of the polymer adsorbent. At high desorption temperature, the water vapor sorption kinetics also high (Sultan et al., 2016), leading to decrease the time required for the desorption phase. It implies that the desorption rate at a high temperature is faster as compared to the low temperature. The high temperature is leading to the faster released of water vapor. The results show that the values of adsorption/desorption amount increase from 0.005 kg/kg, 0.0054 kg/kg, 0.0058 kg/kg and 0.0074 kg/kg, respectively, for desorption temperatures (T_{des}) of 35 ºC, 45 ºC, 55 ºC and 65 ºC.

4.3.2. The Effect of the Desorption Temperature on the Average Dehumidification Index

Figure 4.2 shows the effect of the desorption temperature on the average dehumidification index. In general, the average dehumidification index of the system increases with increasing desorption temperature.

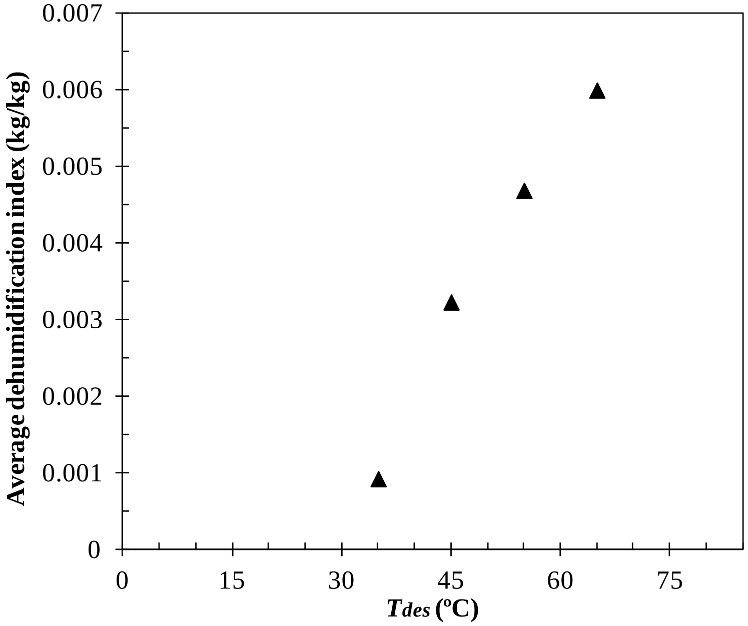

Figure 4.2. Average dehumidification index for various desorption temperature.

The rate of water vapor adsorbed was an important key during the dehumidification process. Water vapor adsorbed is a function of the mass transfer which is driven by the partial pressure of water vapor and its saturation pressure. Higher temperature guiding to higher vapor pressure with more mass transfer occurs. It involves that at high temperature, the hot and dry air could capture most moisture from the desiccant material. High moisture content in the air provides a high driving force for moisture transport, hence increases the dehumidification index (Vivekh et al., 2018). When increasing desorption temperatures from 35 ºC, 45 ºC, 55 ºC and 65 ºC, the average dehumidification indexes increase from 0.001 kg/kg, 0.003 kg/kg, 0.005 kg/kg, 0.006 kg/kg, respectively.

4.3.3. The Effect of the Desorption Temperature on Latent Heat Ratio

Figure 4.3 depicts the effect of the desorption temperature on latent heat performance for the latent heat ratio and latent effectiveness of the desiccant dehumidification system.

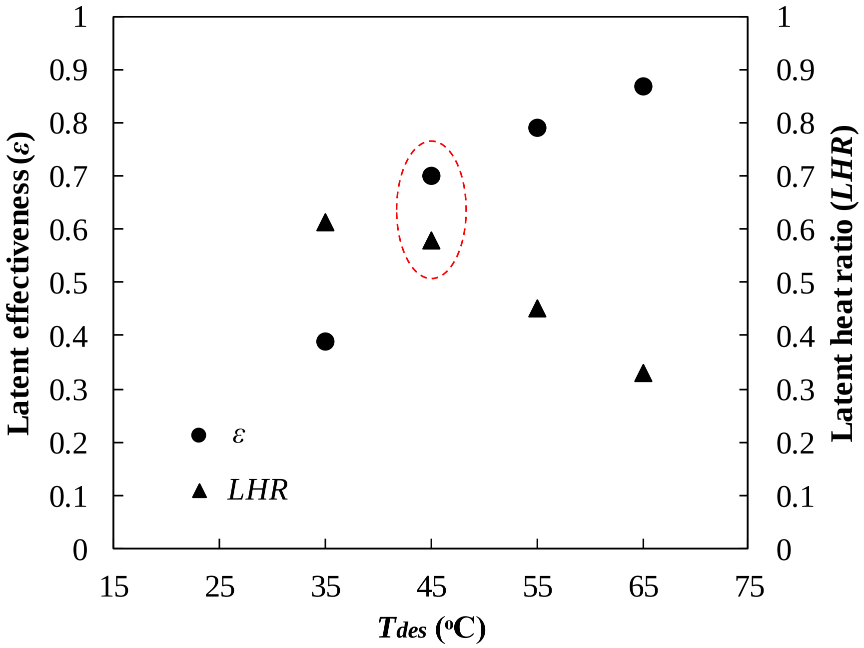

Figure 4.3. Latent heat ratio and effectiveness of desiccant dehumidification system with the variation of the desorption temperature.

The latent heat ratio and effectiveness show different characteristics towards the variation of desorption temperatures. It was shown that the increase of desorption temperature reduced the latent heat ratio, in contrary, it is increased the latent effectiveness. In associate with average dehumidification index on Fig. 4.2, particularly on high temperature, the desiccant dehumidification systems could provide a large difference of water vapor adsorb between the adsorption and desorption processes. However, to achieve a high temperature, its required a high amount of energy input. Energy input was employed to reach high desorption temperature to heat up the polymer. Thus, the polymer becomes dry and could adsorb more moisture for the dehumidification process. Energy consumption to achieve a high temperature directly influences the total heat required for desiccant dehumidification system. Increasing the desorption temperature guided to the increase of sensible heat, therefore reduced the latent heat ratio. For the case of latent effectiveness, at high desorption temperature, the sorption capacity is higher because the humidity of the hot air is lower. Thus, enhancing the moisture uptake followed by increasing the latent effectiveness. Based on the results, we found that if we consider the energy saving, the desorption temperature should be low to achieve high performance of the system. In contrast, if the attention is given to the moisture removal ability, the high desorption temperature is necessary.

But then, in Fig. 4.3 indicates by the circle, a recommendation parameter for optimizing the system performance is proposed. We found that a suitable desorption temperature was 45 ºC for desiccant dehumidification system. It shows that the latent effectiveness and latent heat ratio almost reach a similar value. In this case, the heat requirement for dehumidification is almost equal to the ability of moisture removal. Besides, the results of the present study establish that when the desorption temperatures increase from 35 ºC, 45ºC, 55 ºC, and 65 ºC, the latent heat ratio decrease from 0.61, 0.58, 0.45, and 0.33 respectively. While the latent effectiveness increases from 0.39, 0.7, 0.79, and 0.87 when the desorption temperature increases from 35 ºC, 45 ºC, 55 ºC, and 65 ºC, respectively.

4.4 Conclusions

The latent heat performance and dehumidification ability of the desiccant dehumidification system through four different desorption temperatures of 35 ºC, 45 ºC, 55 ºC, and 65 ºC were experimentally examined. The experimental data and analysis indicate that the reduction of the desorption temperature would increase the latent heat ratio of the desiccant dehumidification system. When adjusting the desorption temperature, the desiccant ability of the system increases with the increase of desorption temperature. It reveals that the highest latent effectiveness and dehumidification ability are found at the highest desorption temperature of 65 ºC. It was 0.87 and 0.006 kg/kg, respectively. The latent heat ratio was found to be maximum when the system driven by the low desorption temperature of 35 ºC. It was found at 0.61. We clarified that even the system is driven by low desorption temperature, still it could give a good performance by showing its ability to remove the moisture with high latent heat ratio.

Nomenclature

c_p : specific heat of air, kJ/(kg.K)

d : moisture removal capacity, kg/kg

D_i : dehumidification index, kg/kg

$\dot{m}$: air mass flow rate, kJ/kg

Q_{ads} : an average of enthalpy exchange, W

Q_{des} : an average of heat exchange, W

Q_{lat} : latent heat, W

Q_{sen} : sensible heat, W

t : dehumidification time, s

T : temperature, K

X : Humidity ratio, kg/kg

Greek symbols

τ : switching time, minutes

ε : latent effectiveness

subscript

a : air

ads : adsorption

des : desorption

eq : equilibrium

in : inlet

out : outlet

References

Alahmer, A., Alsaqoor, S., Borowski, G., Effect of parameters on moisture removal capacity in the desiccant cooling systems, Case Studies in Thermal Engineering 13 (2019) 100364.

Amer, E. H, Kotb, H., Mostafa, G. H. and El-Ghalban, A. R., Theoretical and experimental investigation of humidification-dehumidification desalination unit, Desalination 249 (2009) 949-959.

Chang, K., Wang. H., Chung, T., Effect of regeneration conditions on the adsorption dehumidification process in packed silica gel beds, Appl. Therm. Eng. 24 (2004) 735-742.

Chung, J.D., Lee, D.Y., and Yoon, S.K., Optimization of desiccant wheel speed and area ratio of regeneration to dehumidification as a function of regeneration temperature, Solar Energy 83 (2009) 625-635.

Fong, K. F., Lee, C.K., Impact of adsorbent characteristics on performance of solid desiccant wheel, Energy 144 (2018) 1003-1012.

Hamamoto, Y., Mori, H., Matsuoka, F., Numerical Simulation of a Dehumidification/Humidification Performance of a Desiccant Rotor Using Pore Size Controlled Material Regenerated by Low Grade Thermal Energy, International Refrigeration and Air Conditioning Conference 2008, Paper 863, http://docs.lib.purdue.edu/iracc/863.

Isetti, C., Nannei, E., Magrini, A., On the application of a membrane air—liquid contactor for air dehumidification, Energy and Buildings 25 (1997) 185-193.

Islam, M.R., Alan, S.W.L. and Chua, K.J., Studying the heat and mass transfer process of liquid desiccant for dehumidification and cooling, Applied Energy 221 (2018) 334-347.

Kabeel, A.E., Adsorption-desorption operations of multilayer desiccant packed bed for dehumidification applications, Renewable Energy 34 (2009) 255-265.

Liu, X.H., Jiang, Y., Yi, X.Q., Effect of regeneration mode on the performance of liquid desiccant packed bed regenerator, Renew. Energ. 34 (2009) 209-216.

Sayilgan, S. C., Mobedi, M., Ulku, S., 2016, Effect of regeneration temperature on adsorption equilibria and mass diffusivity of zeolite 13x-water pair, Microporous and Mesoporous Mater 224 (2016) 9-16.

Shelpuk, B., The technical challenges for solid desiccant cooling, Heat Recover Systems & CHP 13 (44) (1993) 321-328.

Sultan, M., El-Sharkawy, I. I., Miyazaki, T., Saha, B. B., Koyama, S., Maruyama, T., Maeda, S. and Nakamura, T., Water vapor sorption kinetics of polymer-based sorbent: Theory and experiments, Appl. Therm. Eng. 106 (2016) 192-202.

Tsujiguchi, T., Osaka, Y., Kodama, A., Feasibility study of simultaneous heating and dehumidification using an adsorbent desiccant wheel with humidity swing, Appl. Therm. Eng. 177 (2017) 437-442.

Vivekh, P., Kumja, M., Bui, D.T. and Chua, K. J., Recent development in solid desiccant coated heat exchangers – A review, Applied Energy 229 (2018) 778-803.

White, S. D., Goldsworthy, M., Reece, R., Spillmann, T., Gorur, A., Lee, D., Characterization of desiccant wheels with alternative materials at low regeneration temperatures, Int. J. Refrigeration 34 (2011) 1786-1791.

X.N. Wu, T. S. Ge, Y. J. Dai, R. Z. Wang, Review on substrate of solid desiccant dehumidification system, Renewable and Sustainable Energy Reviews 82 (2018) 3236-3249.

X. Zheng, T. S. Ge, R. Z. Wang, Recent progress on desiccant materials for solid desiccant cooling systems, Energy 74 (2014) 280-294.

Y.D. Tu, R. Z. Wang, T. S. Ge, X. Zheng, Comfortable, high-efficiency heat pump with desiccant-coated, water-sorbing heat exchangers, Scientific Reports 7 (2017) 1-10.

Zhang, L., Fu, H., Yang, Q., Xu, J., Performance comparisons of honeycomb-type adsorbent beds (wheels) for air dehumidification with various desiccant wall materials, Energy 65 (2014) 430-440.

Hong, S.W., O. Kwon, K., Chung, J. D., Effect of the switching time on the performance of an adsorption chiller, Journal of Mechanical Science and Technology 30 (5) (2016) 387-2395.

CHAPTER 5

Chapter 5

HEAT TRANSFER ENHANCEMENT OF DESICCANT DEHUMIDIFICATION SYSTEM (DIRECT CONTACT HEAT EXCHANGER DESIGN)

This chapter highlights the heat transfer enhancement of the desiccant dehumidification system by using a passive technique. A good configuration of desiccant heat exchanger should provide good contact between air and desiccant material for enhancing the heat and mass transfer coefficient. However, for most of the cases, there is no sufficient contact which reduces their performance due to the limits of heat potential towards the system. An experimental study on heat transfer enhancement in the desiccant dehumidification system by using delta wing/ winglet vortex generators was conducted as an attempt to improve the convective heat transfer inside the system. Double-sided delta-wing (T-W) tape inserts were designed and the effects of the wing-width ratio (0.31, 0.47, and 0.63) on the heat transfer and fluid flow characteristics of the heat exchanger were investigated. The results were compared with those obtained for a plain tube and tube with a longitudinal strip (L-S) insert. The T-W tape insert (wing-width ratio: 0.63) results in the highest average Nusselt number, where the average Nusselt number is higher by 177% relative to that for the plain tube. Despite the significant heat transfer enhancement, the friction factor is 11.6 times higher relative to that for the plain tube, indicating that friction loss is more pronounced due to the presence of T-Ws. The T-W tape insert (wing-width ratio: 0.63) also results in the highest thermal performance factor (1.15). The Nusselt number, thermal performance factor, and friction factor of the heat exchanger increases as the wing-width ratio of the T-Ws increases. Based on the experimental data, empirical correlations were developed to predict the Nusselt number, friction factor, and thermal performance factor of the double-pipe heat exchanger with T-W tape inserts.

5.1 Introduction

The need to develop an air conditioning system with low energy consumption becomes mandatory when the global demand for energy increases due to the rapid population and industrial growth. To overcome the problems involved in the energy issue, an air conditioning system using adsorption is one of the highly challenging technologies for reducing the energy consumption. Typically, a desiccant dehumidification system should have a large contact between the air and desiccant material to provide good heat and mass transfer. At this stage, however, none of these two combinations yet to be perfectly resolved. To date, our considerable efforts have been made to achieve high performance of the heat exchanger by conducting experimental study of convective heat transfer enhancement of enhanced tube heat exchanger.

In general, there are two techniques used to enhance heat transfer of heat exchangers: passive and active techniques. Active techniques require the use of an external power supply for heat transfer augmentation whereas in passive techniques, heat transfer enhancement is achieved by passive means (such as using inserts or extended surfaces), thereby eliminating the need for an external power source. Passive techniques are also advantageous over active techniques because the inserts are relatively easy to fabricate, which reduces installation costs. For this reason, passive techniques are preferable to enhance heat transfer of heat exchangers. Passive techniques do not only involve the use of special inserts or extended surfaces, but also nanofluids, where solid nanoparticles of high thermal conductivity are dispersed into the base fluid (Webb, 1994). Heat transfer enhancement can be achieved by any of the following mechanisms: (a) using a secondary heat transfer surface, (b) disrupting the unenhanced fluid flow, (c) disrupting the laminar sublayer within the turbulent boundary layer, (d) introducing secondary flow, (e) promoting boundary layer separation, (f) promoting flow attachment/reattachment, (g) enhancing the effective thermal conductivity of the fluid under static conditions, (h) enhancing the effective thermal conductivity of the fluid under dynamic conditions, (i) delaying the development of boundary layer, (j) thermal dispersion, (k) increasing the order of fluid molecules, (l) flow redistribution, (m) modifying the radiative properties of the convective medium, (n) increasing the difference between the surface and fluid temperatures, (o) increasing the fluid flow rate, and (p) increasing the thermal conductivity of the solid phase by nanotechnology (Siddique, 2010).

Most of these techniques have been used to enhance the heat transfer of heat exchangers with single-phase flows. Methods (b) and (c) appear to be the promising mechanisms for heat transfer enhancement of heat exchangers among all the aforementioned mechanisms. Special inserts of various geometries are used to disrupt the fluid flow and development of thermal boundary layer as well as generate longitudinal vortices, which enhance the mass transfer of fluid between the centerline of the closed conduit and near-wall regions (Song et al, 2017). Furthermore, these inserts reduce the thermal resistance of the fluid flow, which increases the convective heat transfer coefficient. These special inserts (heat transfer augmenters), which are capable of generating longitudinal vortices in order to enhance heat transfer, are known as vortex generators (VGs) (Xu et al., 2017). Different types of VGs have been used for heat transfer enhancement such as louvered strip inserts (Mohammed et al., 2013; Yaningsih et al., 2018), helical screw inserts (Roy and Saha, 2015; Zade et al, 2017), wire coil inserts (Keklikcioglu and Ozceyhan, 2016; Sundar et al, 2017), twisted tape inserts (Yaningsih et al., 2016; Yaningsih and Wijayanta, 2017; Man et al, 2017), and delta-wing/winglet tape inserts (Fiebig et al, 1993; Gentry et al., 2002; Yakut et al., 2005). Even though it is proven that these VGs can significantly improve the heat transfer of heat exchangers, these VGs may also lead to an increase in pressure drop due to higher frictional losses as the fluid flows through the heat exchanger. This is highly undesirable because a high pressure drop will increase the pumping power required to pump the fluid throughout the system, which somewhat negates the convective heat transfer enhancement provided by the VGs. In this regard, delta-wing/winglet VGs are suitable to enhance heat transfer of heat exchangers while fulfilling the pressure constraints. Many experimental studies have shown the great potential of delta-wing/winglet VGs for heat transfer enhancement. Based on the findings of the studies published to date, delta-wing/winglet VGs increase heat transfer by a factor of 2 with only a minor increase in pressure drop. Delta-wing/winglet VGs of various geometries have been studied extensively where these VGs were used as inserts in ducts/channels or attached to the surface as fins.

Experimental and numerical studies have been conducted over the years to investigate the heat transfer and fluid flow characteristics of delta-wing/winglet VGs. Fiebig et al. (1993) investigated the effect of delta-winglet VGs on heat transfer and fluid flow characteristics of a fin-tube heat exchanger with flat and round tubes. The results showed that the strong longitudinal vortices generated by the delta-winglet VGs increase both the heat transfer and pressure drop of the fin-tube heat exchanger. The results also showed that the heat transfer rate was higher by 20% while the friction factor quadrupled for the fin-round tube heat exchanger compared with those for the fin-flat tube heat exchanger. Gentry and Jacobi (2002) conducted an experimental study to improve heat transfer of an air-side heat exchanger, where delta-wing VGs were used to modify the channel flow. The heat transfer and fluid flow characteristics of the delta-wing VGs were examined for various fin and VG configurations. The results showed that the vortex strength and location of the VGs have significant effects on heat transfer augmentation. In addition, the delta-wing VGs increased heat transfer as much as 300% compared with that for the baseline case. Yakut et al. (2005) performed experiments to examine the heat transfer and vortex characteristics of double-sided delta-winglet VGs. The effects of geometrical parameters (angle of attack: 30, 60, and 90°; winglet height: 8, 12, and 16 mm; pitch arrangement: 25, 50, and 75 mm) and flow parameters (Reynolds number: 3,690, 10,493, and 16,906) were examined using Taguchi experimental design. The results showed that each parameter influenced the heat transfer and vortex characteristics at varying degrees. The Reynolds number had a pronounced effect on the heat transfer characteristics and vortex-shedding frequency whereas the winglet height had a marked effect on the friction factor. The maximum heat transfer rate was achieved at the following parameters: (1) angle of attack: 60°, (2) winglet height: 16 mm, (3) pitch arrangement: 25 mm, and (4) Reynolds number: 16,906. The minimum friction factor was attained at the following parameters: (1) angle of attack: 30°, (2) winglet height: 8 mm, (3) pitch arrangement: 75 mm, and (4) Reynolds number: 16,906.

Eiamsa-ard and Promvonge (2011) used double-sided delta-wing tape (T-W) inserts inside a heat exchanger tube. The convective heat transfer and fluid flow characteristics of the heat exchanger were investigated for two arrangements of T-Ws (forward/backward), T-Ws with alternate axis (T-WA), three wing-width ratios, and three wing-pitch ratios. Air was chosen as the working fluid, which flows through the test section. Numerical simulations were also conducted to examine the flow patterns and temperature fields of the heat exchanger tube in the presence the T-W inserts. Based on the T-W arrangement, the results showed that the forward T-Ws resulted in higher heat transfer rate compared with that for backward T-Ws, with a difference of 7%. The results also showed that heat transfer rate and friction factor were higher for the tube with T-WA insert compared with those for the tube with T-W inserts.

Deshmukh and Vedula (2014) proposed non-conventional inserts in the form of curved delta-wing VGs. The inserts were manufactured using a central rod where the curved delta-wing VGs were attached on opposite sides at specific axial locations. They evaluated the effect of pitch to the projected length ratio, height-to-tube inner diameter ratio, and angle of attack on the heat transfer performance of the system under turbulent flow regime (Reynolds number: 10,000–45,000). The results showed that almost all the configurations for the curved delta-wing VGs had a performance ratio of more than 1. Skullong et al. (2016) investigated the heat transfer and fluid flow characteristics of combined wavy-groove and delta-winglet VGs (WVGs) in a solar air heater channel. They examined the effects of three wing porosity area ratios (porosity ratios) and four wavy-groove winglet distance-to-channel height ratios at a fixed angle of attack. They concluded that the use of perforated WVGs (especially those with large wing porosity area ratios) reduced the flow resistance in the channel. For comparison, they also investigated heat transfer enhancement of the heat exchanger using quadruple perforated delta-winglet pairs inside a heated circular tube with inline arrays (Skullong et al., 2017). To reduce frictional losses, each delta-winglet was formed by punching a triangular-shaped hole through the insert. The delta-winglets were designed based on the relative winglet height (blockage ratio) and relative winglet pitch (pitch ratio). Air was chosen as the working fluid and the Reynolds number was varied from 4,180 to 26,000. The results showed that the Nusselt number increased with an increase in the blockage ratio. In contrast, the Nusselt number decreased with an increase in the pitch ratio. Lei et al. (2017) conducted numerical simulations for delta-winglet VGs of different geometries, pitches, and angles of attack. The field synergy principle was used to analyze the mechanism for heat transfer enhancement. The results showed that the swirling motion created by the VGs enhanced flow mixing, which in turn, enhanced heat transfer with a minor increase in the pressure drop. The results also showed that the Nusselt number increased for delta-winglet VGs with higher angles of attack and lower pitch values.

Previous studies have also shown that the thermal performance of heat exchangers is primarily dependent on the geometrical features of the inserts. Referring to the results of previous studies, modification of the geometrical structure of delta-wing vortex generators i.e. width ratio, pitch ratio, height ratio and angle of attack, shows a great impact on both of heat transfer and friction factor enhancement. Although heat transfer enhancement by special inserts has been studied extensively among the heat transfer and fluid flow community, there is a paucity of studies concerning the effects of wing-width ratio of double-sided delta-wing (T-W) VGs on the thermal-hydraulic performance of a double-pipe heat exchanger, leading to the motivation of this study. Hence, in this study, the geometrical features of T-Ws were first examined and new T-W designs were proposed. Experiments were carried out to investigate the effects of wing-width ratio (w/W) on the Nusselt number, friction factor, and thermal performance factor of a double-pipe heat exchanger installed with the newly designed T-W tape inserts, and the results were compared with those for a plain tube and tube installed with longitudinal strip (L-S) insert. Finally, empirical correlations were developed to predict the Nusselt number, friction factor, and thermal performance factor for the heat exchanger with double-sided delta-wing VGs.

5.2 Experimental Methods

5.3.1. Experimental Facility

The experiments were conducted using the test rig shown in Fig. 5.1. The test rig consists of a forced circulation loop of hot water (working fluid) and cold water (coolant). The test section was constructed to represent a double-pipe heat exchanger fitted with the L-S insert and T-W tape inserts for the test cases considered in this study. Figure 5.2 shows the detail drawing of the test section, which consists of horizontal inner and outer tubes with a circular cross-section. The inner (d_i) and outer (d_o) diameters of the inner tube are 14.3 and 15.8 mm, respectively, and the length of the inner tube (L_i) is 2,500 mm. The outer tube has an inner diameter (D_i), outer diameter (D_o), and overall length (L_o) of 23.4, 25.4, and 1,950 mm, respectively. Fig. 5.2 also shows the arrangement of the T-Ws inside the inner tube. Based on the direction of fluid flow, the T-W tape inserts were installed in a forward arrangement whereas the L-S insert was installed at the center of the inner tube.

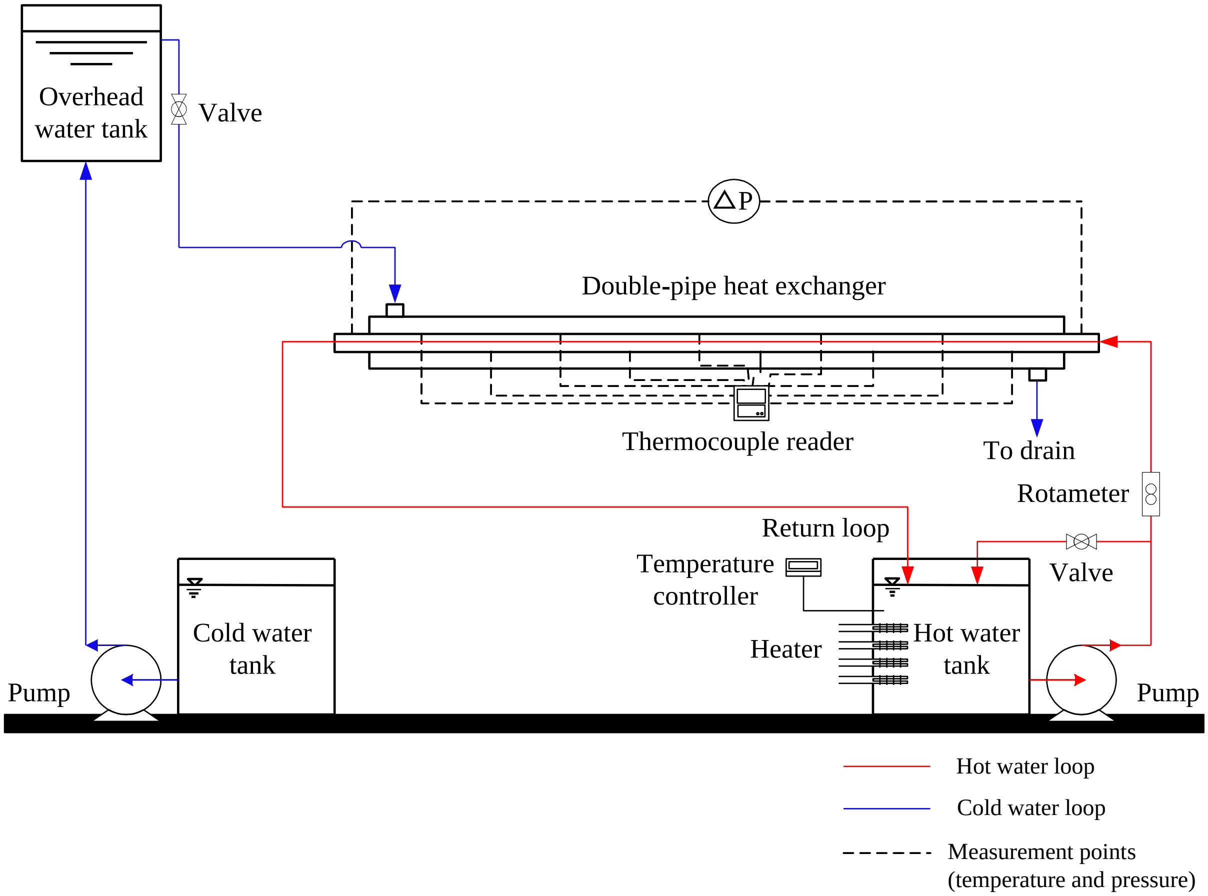

Figure 5.1. Schematic diagram of the test rig.

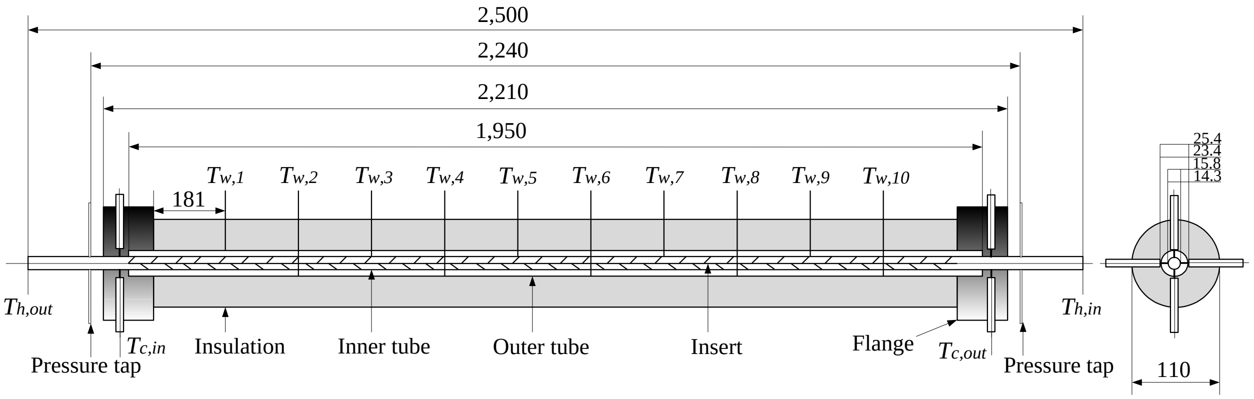

Figure 5.2. Detail drawing of the test section. All dimensions are in millimeters (mm).

To investigate the heat transfer and fluid flow characteristics of the system, hot water was used as the working fluid whereas cold water was used as the coolant. Two centrifugal pumps were used to drive the working fluid into the test section loop. The test section was fitted with sensors to measure the wall temperatures as well as instruments to measure the velocity, pressure, and temperature of the mass fluid flow. It shall be noted that only the temperature of hot water flowing in the inner tube was controlled whereas the cold water flowing in the outer tube was left at room temperature. The mass flow rate of the hot water was controlled by adjusting the ball valve placed upstream of the rotameter, which has a measurement accuracy of ±0.5% of the readings. The mass flow rate of the hot water was varied from 0.033 to 0.082 kg/s, which results in different flow velocities. The Reynolds number was varied from 5,500 to 14,500 and the values were determined based on the flow velocity, fluid properties at the bulk mean temperature, and inner diameter of the inner tube in the test section. A temperature controller with an overall process variable error of ±0.5% was used to control the temperature of the hot water.

The temperature of the hot water at the inlet of the test section was maintained at ±60 °C. After passing through the test section, the hot water flows into the hot water tank, where it was recirculated again through the test section, forming a closed-loop system. In contrast, an open-loop system was used for the cold water stream. The cold water flows through the outer tube at a constant mass flow rate of 0.103 kg/s and room temperature of ±28 °C. In order to provide a steady flow of cold water to the test section, the cold water tank was mounted overhead at a high position from the test section, which provides a steady driving pressure. The thermo-physical properties of the hot and cold water at the inlet of the test section are presented in Table 5.1.

Table 5.1. Thermo-physical properties of the hot and cold water at the inlet of the test section.

Fluid	Temperature [K]	C_p [kJ/kg·K]	ρ [kg/m^3]	μ [kg/m·s]	k [W/m·K]	Pr
Hot water	333.15	4.185	983.3	$4.66(10^{-4})$	0.654	2.98
Cold water	301.15	4.179	995.6	$8.35(10^{-4})$	0.615	3.63

Four calibrated K-type thermocouples with a measurement accuracy of ± 0.1 K (Honda et al., 2005) were installed at the inlet and outlet of the hot and cold water streams in order to measure the water temperature. In addition, 10 thermocouples of the same type were attached along the inner tube at an equal distance of 181 mm to measure the surface temperature of the outer tube wall, as shown in Fig. 5.2. A digital manometer was used to measure the pressure drop across the test section with a measurement accuracy of ±0.5%. Five test cases were investigated in this study: (1) plain tube, (2) tube with L-S insert, (3) tube with T-W tape insert (w/W: 0.31), (4) tube with T-W tape insert (w/W: 0.47), and (5) tube with T-W tape insert (w/W: 0.63). A plain tube was used in the first test case, where there were no inserts installed in the inner tube of the test section. This test case was used as the baseline case in order to validate the test rig. Once the test rig had been validated using the plain tube, experiments were carried out for the other test cases, where the L-S insert and T-W tape inserts were installed in the inner tube of the test section in order to enhance heat transfer of the double-pipe heat exchanger. The results obtained for the five test cases were compared to investigate the heat transfer and fluid flow characteristics of the system.

In this study, the L-S insert and T-W tape inserts were made from aluminum strips. Each aluminum strip has the following dimensions: thickness (t): 0.7 mm, width (W): 12.6 mm, and length (L): 2000 mm. Fig. 5.3(a) shows the geometry of the L-S insert. Since the dimensions (t, W, and L) of the L-S insert and T-W tape inserts are the same, all the inserts have the same aspect ratio (W/t) of 18. Figure 5.3(b) shows the geometry of the T-W tape insert. The T-Ws were created by punching the surface of the aluminum strip with a series of equally-spaced of triangular holes along the centerline of the strip. Three T-W tape inserts were newly designed in this study, where the width (w) of the T-Ws was varied at 4, 6, and 8 mm, resulting in a wing-width ratio (w/W) of 0.31, 0.47, and 0.63, respectively. The chord length (c) of each T-W was fixed at 8 mm. In order to create a double-sided structure, the T-Ws were designed such that they protrude upward and downward alternatingly along the aluminum strip. The axial distance between the adjacent T-Ws, also known as the pitch (p), was fixed at 12 mm and the angle of attack (α) was 45°. Table 5.2 shows the details of experiment characteristic of the system including their dimensions and parameters.

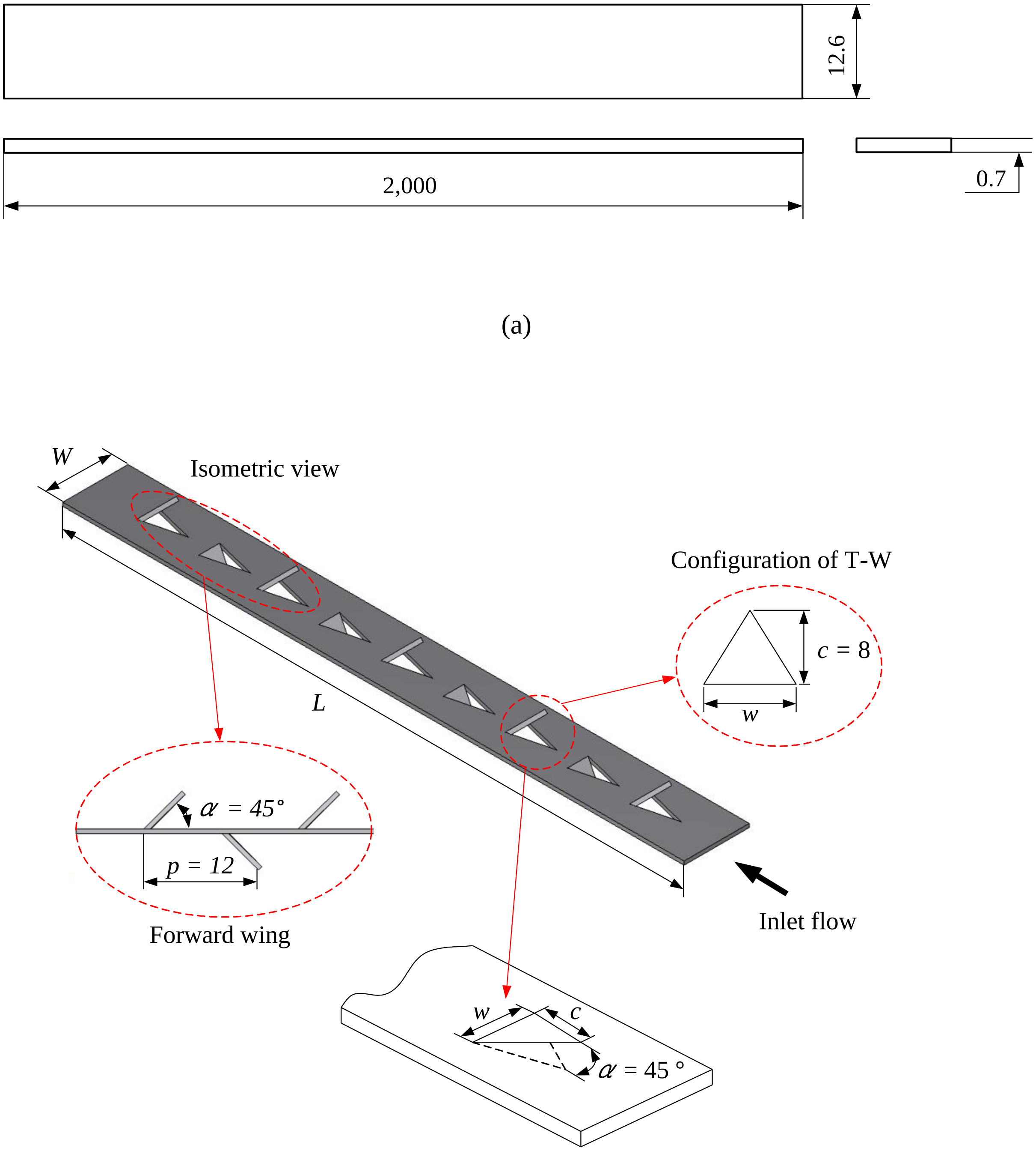

(a)

(b)

Figure 5.3. Geometries of the (a) longitudinal strip (L-S) insert and (b) double-sided delta-wing (T-W) tape insert.

Table 5.2. Geometrical structures and parameters used during experiments.

Geometry of the tube		
Inner tube		
– Inner diameter	d_i, mm	14.3
– Outer diameter	d_o, mm	15.8
– Length of the tube	L_i, mm	2,500
Outer tube		
– Inner diameter	D_i, mm	23.4
– Outer diameter	D_o, mm	25.4
– Length of the tube	L_o, mm	1,950

Working fluid		Cold water	Hot water
Mass flow rate	$\dot{m}$, kg/s	0.103	0.033 - 0.082
Reynolds number	*Re*, -	21,900	5,500 – 14,500

Vortex generator		L-S	T-Ws		
			$w/W = 0.31$	$w/W = 0.47$	$w/W = 0.63$
Thickness	t, mm	0.7	0.7	0.7	0.7
Length	L, mm	2,000	2,000	2,000	2,000
Width	W, mm	12.6	12.6	12.6	12.6
Wing pitch	P, mm	-	12	12	12
Wing width	w, mm	-	4	6	8
Height	c, mm	-	8	8	8
Angle of attack	α, °	-	45	45	45

5.3.2. Experimental Data Analysis

This study is focused on single-phase forced convection flow inside a horizontal heated circular tube fitted with L-S insert and T-W tape inserts. All the data collected from the experiments were obtained under steady-state conditions. Once the flow in the horizontal heated circular tube reached steady-state conditions, the temperature, differential pressure, and mass flow rate of the working fluid were collected over a period of 180 min. The equations for single-phase forced convection flow for both hot and cold water-side surfaces are presented as follows.

The thermo-physical properties of the working fluid were evaluated based on the bulk mean temperature. It was defined as:

For the inner tube (hot water):

$$T_{b,h} = \frac{T_{h,i} + T_{h,o}}{2} \tag{1}$$

For the annulus tube (cold water):

$$T_{b,c} = \frac{T_{c,i} + T_{c,o}}{2} \tag{2}$$

where $T_{b,h}$ is the bulk hot water temperature, and $T_{b,c}$ is the bulk cold water temperature.

The convective heat transfer rate of the cold water in the outer tube was determined using the following equation:

$$Q_c = \dot{m}_c c_{p,c}\left(T_{c,o} - T_{c,i}\right) = h_o A_o\left(\bar{T}_{w,o} - T_{b,c}\right) \tag{3}$$

where Q_c is the convective heat transfer rate of the cold water in the outer tube, and $\bar{T}_{w,o}$ is the mean outer wall temperature of the inner tube. $\bar{T}_{w,o}$ were determined using the following equations:

$$\bar{T}_{w,o} = \frac{\sum T_{w,o}}{10} \tag{4}$$

The convective heat transfer rate of the hot water in the inner tube (Q_h) was approximated using the following equation:

$$Q_h = \dot{m}_h c_{p,h}\left(T_{h,i} - T_{h,o}\right) = U_i A_i \Delta T_{LMTD} \tag{5}$$

where ΔT_{LMTD} represents the logarithmic mean temperature difference, which is given by:

$$\Delta T_{LMTD} = \frac{\left(T_{h,i} - T_{c,o}\right) - \left(T_{h,o} - T_{c,i}\right)}{\ln\left(\left(T_{h,i} - T_{c,o}\right)/\left(T_{h,o} - T_{c,i}\right)\right)} \tag{6}$$

The heat loss (Q_{loss}) through the insulation and average heat transfer rate (Q_{ave}) were estimated based on the convective heat transfer rates of the two fluid streams. Q_{loss} is defined as the difference between Q_h and Q_c, which is expressed mathematically as:

$$Q_{loss} = Q_h - Q_c \tag{7}$$

Based on the experimental data, the heat loss through the insulation was assumed to be negligible because it was found that the magnitude for Q_{loss} was not significant (Q_{loss} < 2.29%). The average heat transfer rate (Q_{ave}) was determined using the following equation:

$$Q_{ave} = \frac{Q_h + Q_c}{2} \tag{8}$$

Once Q_{ave} was known, the overall heat transfer coefficient of the inner tube (U_i) was determined by manipulating the following equation:

$$Q_{ave} = U_i A_i \Delta T_{LMTD} \tag{9}$$

The average convective heat transfer coefficient (h_i) was computed based on the thermal resistance of the system. The thermal resistance of the system consists of three thermal resistances in series. As the heat flows from the hot water to the cold water, it needs to overcome the thermal resistance of the flow associated with the (1) convection in the inner tube, (2) conduction of the inner tube wall, and (3) convection in the outer tube. The thermal resistance of the system can be expressed as:

$$\frac{1}{U_i A_i} = \frac{1}{h_i A_i} + \frac{\ln\left({}^{d_o}/{}_{d_i}\right)}{2\pi k_p L} + \frac{1}{h_o A_o} \tag{10}$$

Once the overall heat transfer coefficient based on the internal surface area of the inner tube (U_i) was determined, and the convective heat transfer coefficient in the inner tube (h_i) was computed using the following equation:

$$h_i = \frac{1}{\left[\frac{1}{U_i} - \frac{d_i \ln(d_o/d_i)}{2k_p} - \frac{d_i}{d_o h_o}\right]} \tag{11}$$

Finally, the average Nusselt number (*Nu*$_i$) along the tube length in the flow direction was determined using the following equation:

$$Nu_i = \frac{h_i d_i}{k_i} \tag{12}$$

The friction factor (*f*) can be determined by calculating the pressure drop (ΔP) across the horizontal heated circular tube based on the pressure values measured from experiments. The friction factor for a fully developed flow in the inner tube was determined using the following equation:

$$f = \frac{\Delta P}{(\rho u^2/2)(L/d_i)} \tag{13}$$

The Reynolds number (*Re*) of the flow in the inner tube under the turbulent flow regime was determined based on the flow velocity (*u*), equivalent tube diameter (*d*$_i$), and the thermo-physical properties of water (specifically density (ρ) and dynamic viscosity (μ)) at the mean bulk water temperature in the inner tube ($T_{b,h}$). The Reynolds number is given by:

$$Re = \frac{\rho u d_i}{\mu} \tag{14}$$

The same experimental conditions were used for the plain tube and tube with T-W tape inserts. Thus, the thermal performance factor of the system (η) at the same pumping power is defined as the ratio between the convective heat transfer coefficients of the tube installed with T-W tape inserts and those of a plain tube (Yakut et al., 2004; Yakut et al., 2004).

Based on the constant pumping power constraint:

$$Re_o = Re_t (f_t/f_o)^3 \tag{15}$$

then, the friction factor and Reynolds number defined from Eq. 14 can be given as:

$$Re_o = Re_t (f_t/f_o)^3 \tag{16}$$

Finally, the thermal performance factor of the system was determined using the following equation:

$$\eta = \left.\frac{h_t}{h_o}\right|_{pp} = \left.\frac{Nu_t}{Nu_o}\right|_{pp} = \left(\frac{Nu_t}{Nu_o}\right)\left(\frac{f_t}{f_o}\right)^{-\frac{1}{3}} \tag{17}$$

5.3.3. Uncertainty Analysis

Uncertainty analysis was conducted to determine the uncertainties of the non-dimensional parameters (Nusselt number, friction factor, and Reynolds number) according to the procedure outlined in the following standard (Measurement Uncertainty: Part 1: Instruments and Apparatus: ANSI/ASME PTC 19. 1–1985) (ANSI/ASME, 1986). The uncertainties of the Nusselt number, friction factor, and Reynolds number were determined based on the uncertainties of the dimensional parameters used in the data reduction equations (Kirkup and Frenkel, 2006). The uncertainties of the Nusselt number, friction factor, and Reynolds number are found to be ±1.53%, ±0.129%, and ±0.223%, respectively.

5.3 Results and Discussion

5.3.1. Validation of the Test Rig

The Nusselt numbers and friction factors determined from the experiments were compared with those predicted by standard correlations for a plain tube in order to validate the test rig and evaluate the measurement uncertainties. The Nusselt numbers determined from experiments were compared with those predicted by Gnielinski's correlation (Cengel, 2008). The Gnielinski's correlation used to predict the Nusselt number is given by:

$$Nu = \frac{(f/8)(Re - 1000)Pr}{1 + 12.7(f/8)^{1/2}(Pr^{2/3} - 1)} \tag{18}$$

for $1(10^3) < Re < 5(10^6)$.

Similarly, the friction factors determined from experiments were compared with those predicted by Blasius's correlation (White, 2011). Blasius's correlation used to predict the friction factor is given by:

$$f = 0.3164Re^{-0.25} \tag{19}$$

for $4(10^3) < Re < 1(10^5)$.

Figures 5.4 and 5.5 show the comparison between the Nusselt numbers and friction factors for a plain tube determined from experiments and those predicted by the standard correlations. The relative errors were determined for Nusselt number and friction factor, which were defined as the percentage difference between the experimental and predicted values.

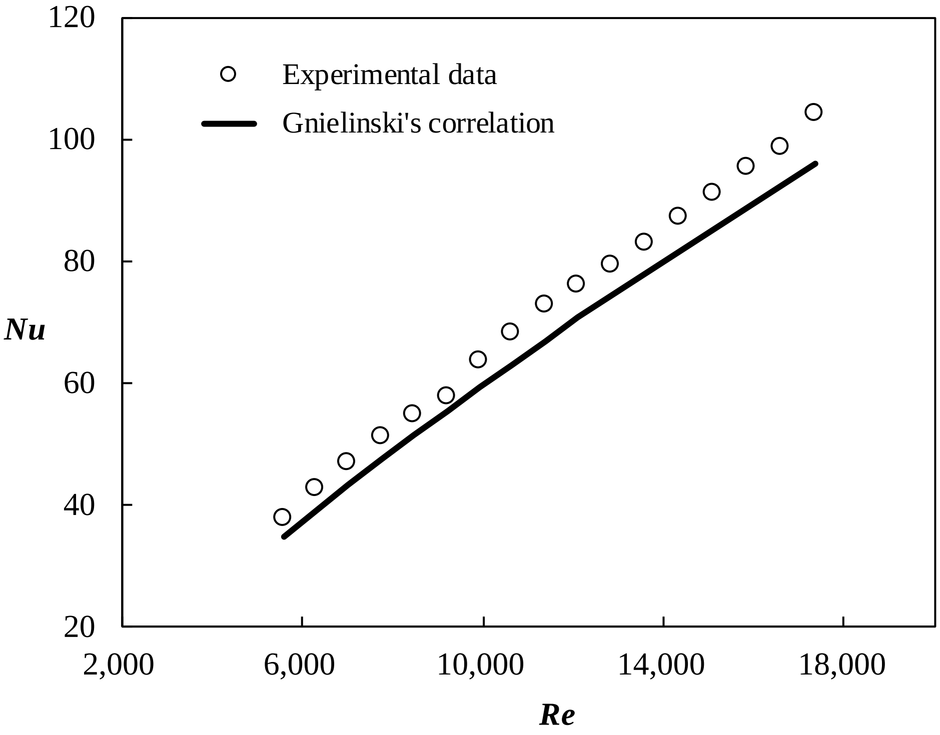

Figure 5.4. Comparison between the Nusselt numbers determined from experiments and those predicted using Gnielinski's correlation for a plain tube.

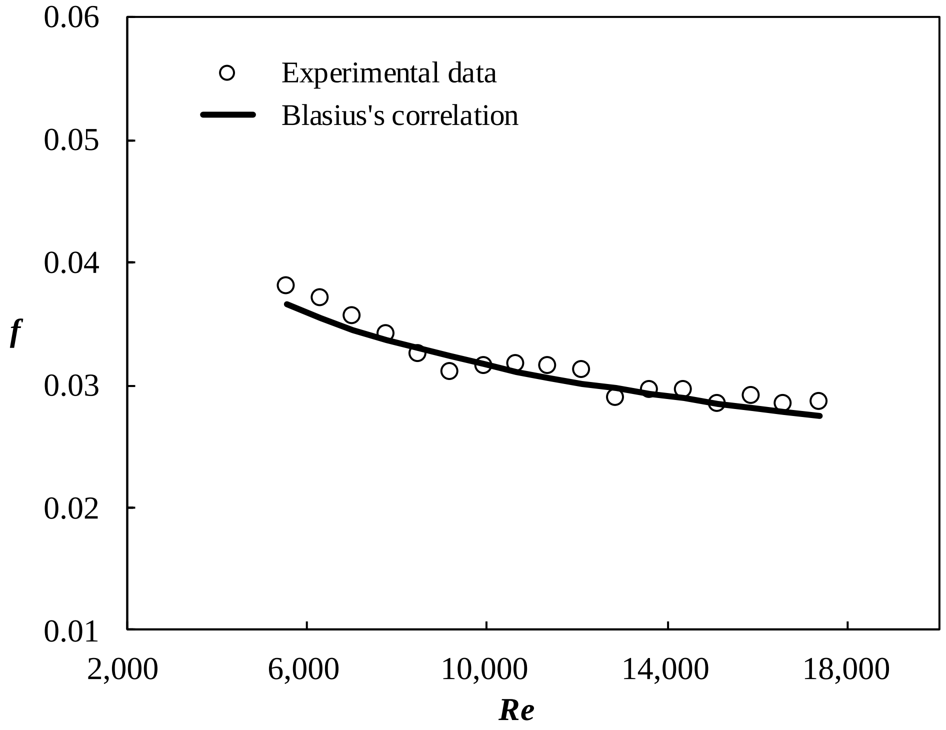

Figure 5.5. Comparison between the friction factors determined from experiments and those predicted using Blasius's correlation for a plain tube.

The percentage difference between the Nusselt numbers determined from experiments and those predicted by Gnielinski's correlation (Eq. 18) is relatively small, with a value of ±7.38%. The percentage difference between the friction factors determined from experiments and those predicted by Blasius's correlation (Eq. 19) is very small, with a value of ±2.42%. In general, the relative errors are small, indicating that there is very good agreement between the experimental data and those predicted by the standard correlations for the plain tube. The results prove the reliability of the test rig for heat transfer and fluid flow measurements.

5.3.2. Effect of the Wing-Width Ratio on the Nusselt number

In order to examine the heat transfer enhancement of the horizontal heated circular tube provided by the L-S insert and T-W tape inserts, the Nusselt numbers of the tube with L-S and T-W inserts (*w/W*: 0.31, 0.47, and 0.63) were compared with those for the plain tube, as shown in Fig. 5.6. It can be seen that there is a similar trend in the heat transfer characteristics for the plain tube and tube with L-S insert and T-W tape inserts, where the Nusselt number increases with an increase in the Reynolds number. This is indeed expected because the higher Reynolds number enhances the turbulence intensity of the flow, which in turn, promotes the rate of heat transfer. Based on the Nusselt numbers, it is evident that the tube with L-S insert and T-W tape inserts have higher convective heat transfer enhancement compared with that for the plain tube. This is likely because the inserts increase the heat transfer surface area, which enhances heat transport. Disruption of the fluid flow (starting from the inlet of the test section) due to the presence of the inserts leads to the development of boundary layer, which induces secondary flow and enhances fluid mixing (Hsieh et al., 2003).

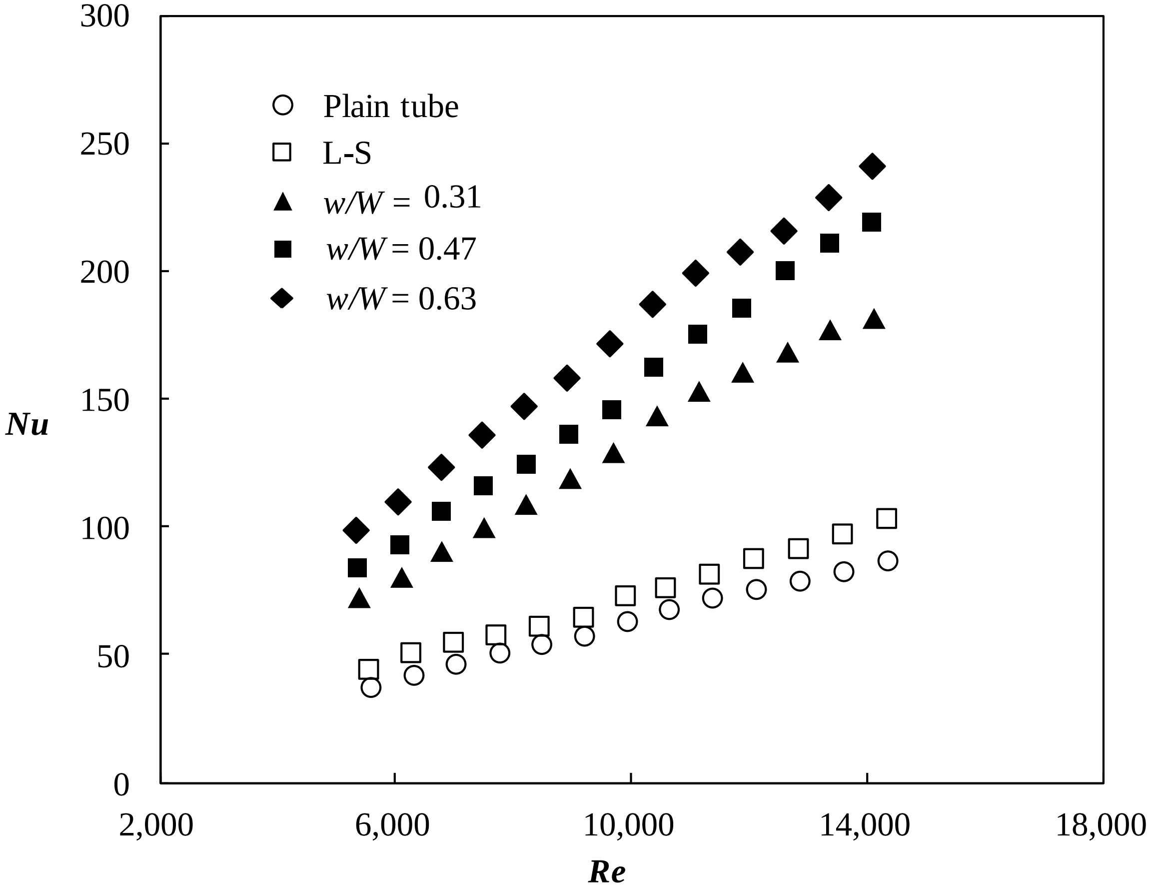

Figure 5.6. Variations of the Nusselt number with the Reynolds number for the plain tube, tube with L-S insert, and tube with T-W tape insert at different wing-width ratios.

It is evident from Fig. 5.6 that the Nusselt numbers are significantly higher for the tube with T-W tape inserts compared with those for the tube with L-S insert. The T-Ws generate longitudinal vortices behind them and the fluid from the underside of the wake swirls to the upper side. These longitudinal vortices entrain the fluid from the periphery toward the center of the vortices (Biswas et al., 1996). This mechanism leads to the growth of the thermal boundary layer. In addition, as the fluid passes through T-Ws, the T-Ws enhance flow mixing between the core and surface. When the fluid within proximity of the T-Ws is replaced by the freestream fluid, the temperature gradients increase near the surface of the T-Ws and channel walls, which promotes heat transfer (Gentry and Jacobi, 2002; Biswas et al., 1996). It is also evident from Fig. 5.6 that the Nusselt number increases with an increase in the wing-width ratio of the T-Ws, which is likely because a higher wing-width ratio promotes flow recirculation and separation, which enhances turbulence intensity of the flow (Promvonge et al., 2014). In general, the convective heat transfer enhancement is superior for the tube installed with T-W tape inserts relative to that for the plain tube. The Nusselt number increases by 21, 114, 159, and 177% for the tube with L-S insert and T-W tape inserts (*w/W*: 0.31, 0.47, and 0.63), respectively, relative to those for the plain tube. The Nusselt number increases by 87, 125, and 145% for the tube with T-W tape inserts (*w/W*: 0.31, 0.47 and 0.63) respectively, relative to those for the tube with L-S insert.

5.3.3. Effect of the Wing-Width Ratio on the Friction Factor

The friction factor was used to evaluate the fluid flow characteristics in this study. Figure 5.7 shows the variations of the friction factor with the Reynolds number for the plain tube and tube with L-S insert and T-W tape inserts. It can be observed that the friction factor decreases with an increase in the Reynolds number. The friction factors are higher for the tube with the L-S insert and T-W tape inserts compared with those for the plain tube, which is likely due to the increase in the contact surface area and reduced free flow, which increases the flow velocity. It is apparent that the friction factors are significantly higher for the tube with T-W inserts (*w*/*W*: 0.31, 0.47, and 0.63) compared with those for the plain tube and tube with L-S insert. This is likely because the flow passage in the tube is blocked by the T-Ws and therefore, the streamwise velocity profiles are different from those in the plain tube. The unbalanced shear forces due to the presence of the T-Ws leads to the generation of secondary flow. The fluid is transported toward the channel walls due to the generation of secondary flow, which distorts the axial velocity profiles along the length of the tube. The fluid is forced outward in order to balance the momentum due to the secondary flow generated by the T-Ws, which increases the flow pressure (Hsieh et al., 2003). The friction factors are higher by a factor of 8.53, 9.93, and 11.6 for the tube installed with T-W inserts (*w/W*: 0.31, 0.47, and 0.63), respectively, compared with those for the plain tube within the range of Reynolds numbers investigated in this study (5,500–14,500). In contrast, the friction factors of the tube with T-W tape inserts (*w/W*: 0.31, 0.47, and 0.63) are only slightly higher than those for the tube with L-S insert by a factor of 1.81, 2.22 and 2.72, respectively. In addition, the friction factor increases with an increase in the wing-width ratio of the T-Ws, which is similar to the trend for the Nusselt number.

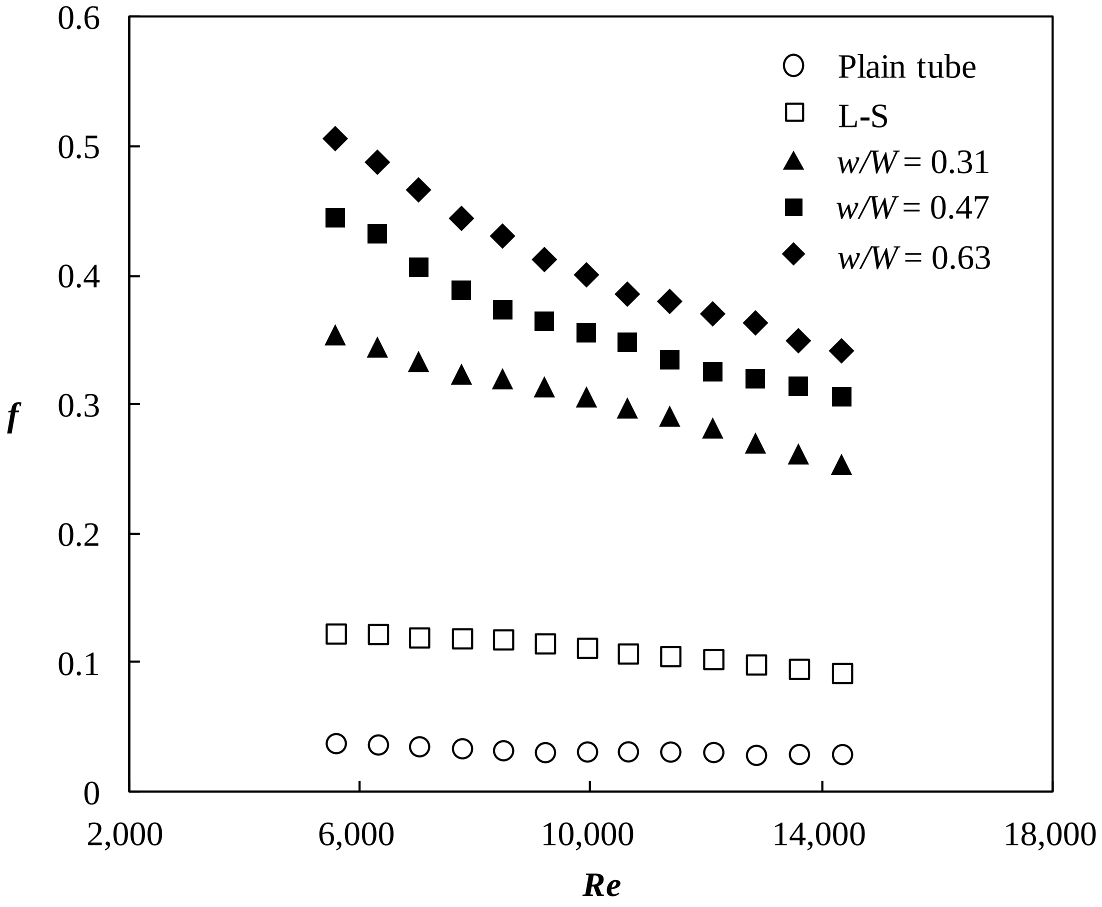

Figure 5.7. Variations of the friction factor with the Reynolds number for the plain tube, tube with L-S insert, and tube with T-W tape insert at different wing-width ratios.

5.3.4. Effect of Wing-Width Ratio on the Thermal Performance

In general, the thermal performance of heat exchangers is evaluated based on the enhancement of convective heat transfer coefficient and reduction of power consumption to pump the fluid through the system (Saha et al., 2016). In this study, the thermal performance was assessed by comparing the convective heat transfer coefficient between the enhanced and reference heat transfer surface areas at the same pumping power, which is given by Eq. 17. The plain tube was used as the baseline case in order to evaluate the thermal performance of the heat exchanger. Figure 5.8 shows the variations of the thermal performance factor with the Reynolds number for the tube with L-S insert and T-W tape inserts (*w/W*: 0.31, 0.47, and 0.63). It can be observed that the thermal performance factor decreases as the Reynolds number increases, which is likely because the thermal boundary layer thickness increases with an increase in the Reynolds number. Thus, the disruption of thermal boundary layer due to the presence of the inserts is more pronounced at lower Reynolds numbers compared with that at higher Reynolds numbers. It can be seen that the thermal performance factor is more than 1.0 up to *Re* = 8,000 for the tube with T-W tape inserts and the thermal performance factor decreases to a value less than 1.0 beyond this point. The thermal performance factor is less than 1.0 for the tube with L-S insert, regardless of the Reynolds number. If $\eta \geq 1.0$, this indicates that the heat transfer for the tube with inserts is higher than that for the plain tube at the same pumping power. Additionally, $\eta \geq 1.0$ implies that the increase of the Nusselt number is more prominent than the rise of the friction losses. Based on the Eq. 13, it shows that the thermal performance factor is defined as the ratio of the heat transfer increment to the friction factor growth. If this values higher than 1, as the friction factor is the denominator, there is the considerable potential to make a concluding remark that the penalty in the form of friction losses is notably insignificant as compared to the heat transfer enhancement. The results show that $\eta \geq 1.0$ for the tube installed with T-W tape inserts up to *Re* = 8,000, indicating the potential of the T-W tape inserts in enhancing convective heat transfer of the double-pipe heat exchanger. Figure 5.8 also shows that the thermal performance factor of the tube with T-W tape inserts increases with an increase in the wing-width ratio. The highest thermal performance factor is obtained for T-Ws with a wing-width ratio of 0.63, followed by T-Ws with a wing-width ratio of 0.47 and 0.31. The lowest thermal performance factor is obtained for the tube with L-S insert. The average thermal performance factors are found to be 0.86, 0.93, 1.03, and 1.15 for the tube with L-S insert and T-W tape inserts (*w/W*: 0.31, 0.47, and 0.63), respectively.

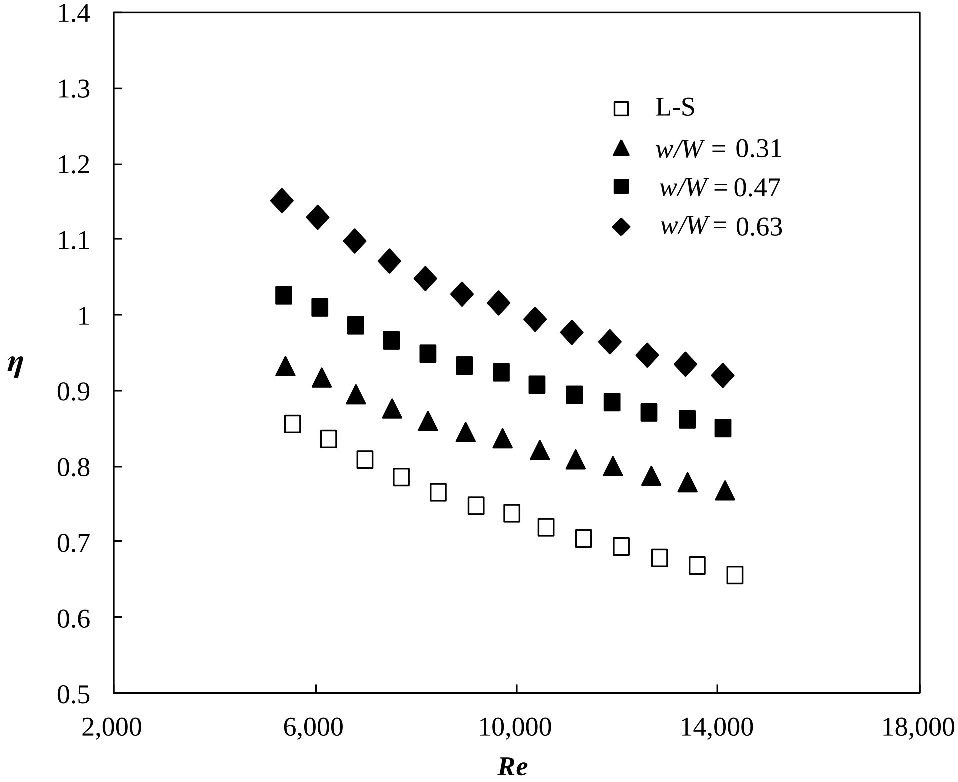

Figure 5.8. Variations of the thermal performance factor with the Reynolds number for the tube with L-S insert and tube with T-W tape insert at different wing-width ratios.

5.3.5. Development of Empirical Correlations

Based on the experimental results, three empirical correlations were developed in order to predict the Nusselt number, friction factor, and thermal performance factor. The empirical correlations were derived based on non-dimensional parameters typically used predict the Nusselt number, friction factor, and thermal performance factor of heat exchangers. The empirical correlations were proposed for the turbulent flow regime based on the experimental conditions in this study: (1) working fluid: water, (2) wing-width ratio of T-Ws (*w/W*): 0.31, 0.47, 0.63, (3) Reynolds number (*Re*): 5,500–14,500, and (4) Prandtl number (*Pr*): 0.3. The empirical correlations proposed in this study to predict the Nusselt number, friction factor, and thermal performance factor are expressed as follows:

$$Nu = 0.017\, Re^{0.985}\, Pr^{0.3}\, (w/W)^{0.396} \tag{20}$$

$$f = 16.172\, Re^{-0.381}\, (w/W)^{0.424} \tag{21}$$

$$\eta = 7.968\, Re^{-0.212}\, (w/W)^{0.274} \tag{22}$$

The Nusselt numbers, friction factors, and thermal performance factors determined from experiments were compared to those predicted by the empirical correlations, as shown in Figs. 5.9, 5.10, and 5.11. It can be seen that there is a minor difference between the experimental and predicted values, where most of the experimental values fall within ±6%, ±5% and ±3% of the predicted Nusselt numbers, friction factors, and thermal performance factors, respectively.

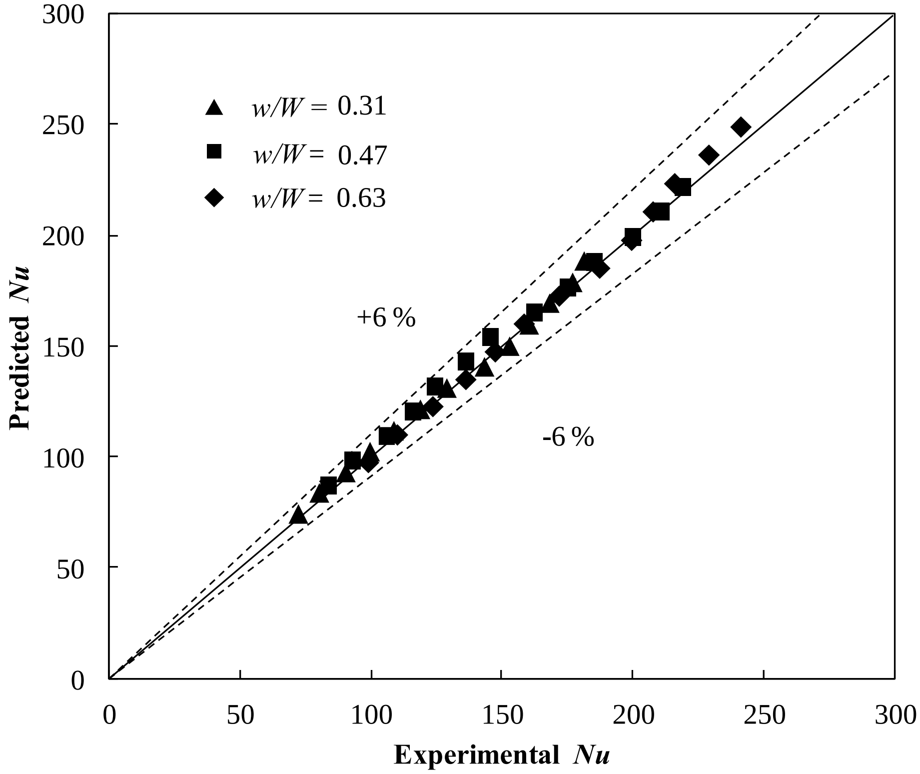

Figure 5.9. Comparison between the *Nu* determined from experiments and those predicted by the empirical correlation.

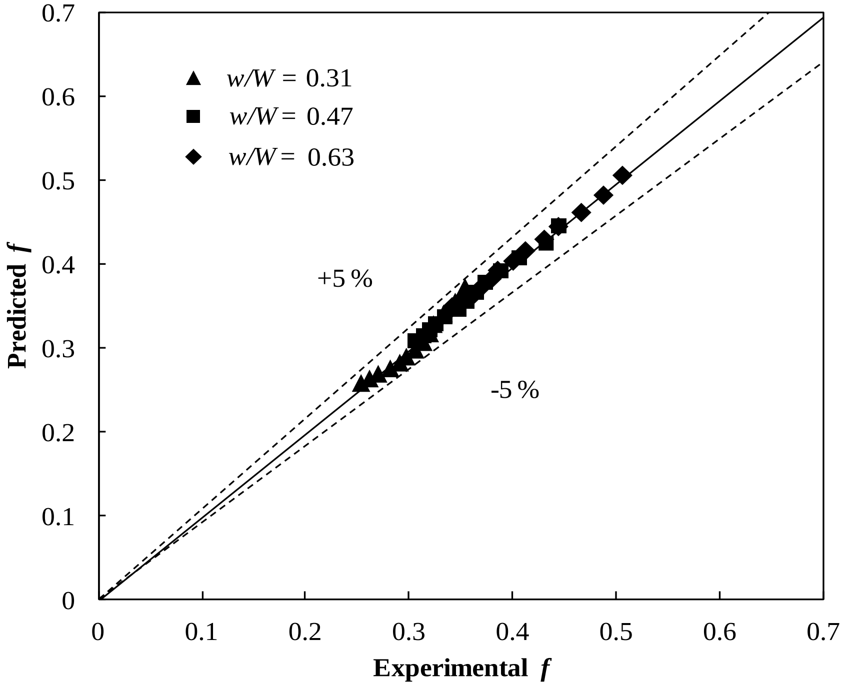

Figure 5.10. Comparison between the *f* determined from experiments and those predicted by the empirical correlation.

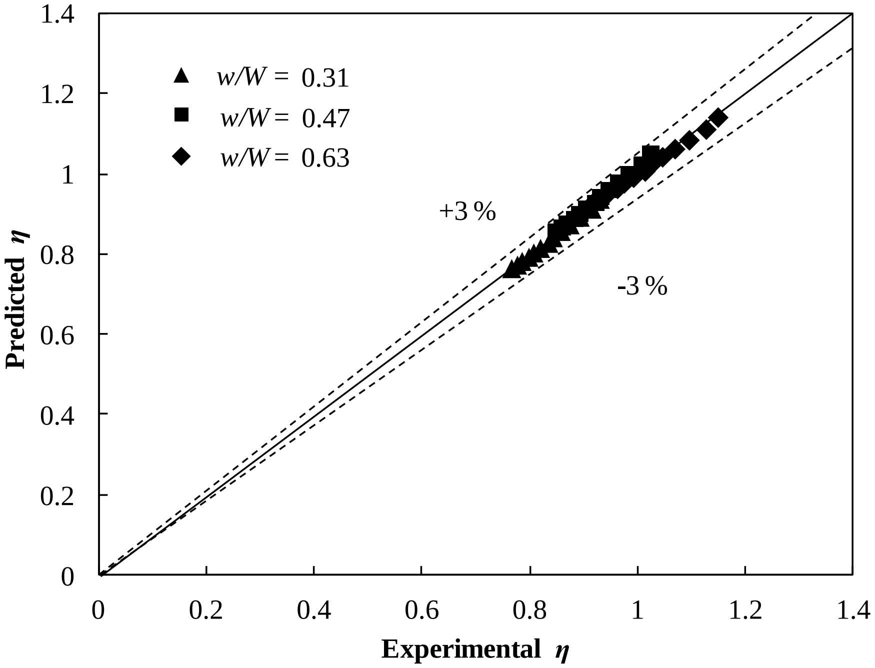

Figure 5.11. Comparison between the η determined from experiments and those predicted by the empirical correlation.

5.4 Conclusions

In this study, the heat transfer and fluid flow characteristics of single-phase turbulent flow in a double-pipe heat exchanger installed with T-W tape inserts (*w/W*: 0.31, 0.47, and 0.63) were investigated and empirical correlations were developed to predict the Nusselt number, friction factor, and thermal performance factor. Based on the experimental results, the T-W tape inserts significantly enhance the average convective heat transfer coefficient and the convective heat transfer increases with an increase in the wing-width ratio of the T-Ws. The T-W tape insert with the highest wing-width ratio (*w/W*: 0.63) results in the highest convective heat transfer enhancement, where the Nusselt number is higher by 177 and 145% compared with those for the plain tube and tube with L-S insert, respectively. The results reveal that the wing-width ratio of the T-Ws significantly affects the flow characteristics and the effect of the wing-width ratio on the friction factor is dependent on the Reynolds number. The friction factor decreases as the Reynolds number increases, but the friction factor increases with an increase in the wing-width ratio of the T-Ws. The T-W tape insert with the highest wing-width ratio (*w/W*: 0.63) also results in the highest friction factor where the friction factor is higher by a factor of 11.6 and 2.72 compared with those for the plain tube and tube with L-S insert, respectively. Despite the higher friction factor, this T-W tape insert also produces the highest thermal performance factor, with a value of 1.15. In general, there is very good agreement between the Nusselt numbers, friction factors, and thermal performance factors determined from experiments and those predicted by the empirical correlations for the double-pipe heat exchanger installed with double-sided delta-wing VGs, with a maximum deviation of ±6%.

Nomenclature

A_i	inner surface area of the inner tube (m^2)
A_o	outer surface area of the inner tube (m^2)
c	chord length of the delta-wing (m)
C_p	specific heat capacity at constant pressure (J/kg·K)
d_i	inner diameter of the inner tube (m)

d_o	outer diameter of the inner tube (m)
D_i	inner diameter of the outer tube (m)
D_o	outer diameter of the outer tube (m)
f	friction factor (dimensionless)
f_t	friction factor of the inner tube with T-Ws (dimensionless)
f_o	friction factor of the plain tube (dimensionless)
h_i	average convective heat transfer coefficient of the inner tube ($W/m^2 \cdot K$)
h_o	average convective heat transfer coefficient of the outer tube ($W/m^2 \cdot K$)
h_p	average convective heat transfer coefficient of the plain tube ($W/m^2 \cdot K$)
h_t	average convective heat transfer coefficient of the inner tube with T-Ws ($W/m^2 \cdot K$)
k_i	thermal conductivity of hot water ($W/m \cdot K$)
k_p	thermal conductivity of the inner tube material ($W/m \cdot K$)
L	length of the inner tube (m)
Nu_o	average Nusselt number of the plain tube (dimensionless)
Nu_i	average Nusselt number of the inner tube (dimensionless)
Nu_t	average Nusselt number of the inner tube with T-Ws (dimensionless)
Nu_p	average Nusselt number of the plain tube (dimensionless)
p	pitch of the delta-wing (m)
Pr	Prandtl number (dimensionless)
Q_h	heat transfer rate of the hot water in the inner tube (W)
Q_c	heat transfer rate of the cold water in the outer tube (W)
Q_{loss}	heat loss (W)
Re	Reynolds number (dimensionless)
t	thickness of the aluminum strip (m)
T_b	mean bulk water temperature in the inner tube (K)
T_c	cold water temperature (K)
T_h	hot water temperature (K)
T_w	outer wall inner tube temperature (K)
u	velocity of hot water in the inner tube (m/s)

U_i	overall heat transfer coefficient based on the internal surface area of the inner tube (W/m^2·K)
$\dot{V}$	volumetric flow rate of fluid (m^3/s)
w	width of the delta-wing (m)
W	width of the aluminum strip (m)

Greek symbols

α	angle of attack (°)
ρ	density of hot water (kg/m^3)
μ	dynamic viscosity of hot water (kg/m.s)
η	thermal performance factor (dimensionless)
ΔP	pressure drop across the inner tube (Pa)
ΔT_{LMTD}	logarithmic mean temperature difference (K)

Subscripts

ave	average
c	cold
h	hot
i	inlet
o	outlet

References

ANSI/ASME, Measurement Uncertainty, PTC 19, 1–1985, Part I, 1986.

Biswas, G., Chattopadhyay, H., Sinha, A., Augmentation of heat transfer by creation of stream wise longitudinal vortices using vortex generators, Heat Transfer Engineering 33 (2012) 406–424.

Biswas, G., Torii, K., Fuji, D., Nishin, K., Numerical and experimental determination of flow structure and heat transfer effects of longitudinal vortices in a channel flow, Int. J. Heat and Mass Trans. 39 (1996) 3441–3451.

Cengel, Y.A., Heat and mass transfer, fifth ed., McGraw-Hill, New York, 2008.

Deshmukh, P. W., Vedula, R. P., Heat transfer and friction factor characteristics of turbulent flow through a circular tube fitted with vortex generator inserts, Int. J. Heat Mass Transf. 79 (2014) 551–560.

Eiamsa-ard, S., Promvonge, P., Influence of double-sided delta-wing tape insert with alternate-axes on flow and heat transfer characteristics in a heat exchanger tube, Chinese J. Chem. Eng. 19 (2011) 410–423.

Fiebig, M., Valencia, A., Mitra, N. K., Local heat transfer and flow losses in fin-tube heat exchangers with vortex generators: a comparison of round and flat tubes, Experimental Heat Transfer, Fluid Mechanics and Thermodynamics 1993: Proceedings of the Third World Conference on Experimental Heat Transfer, Fluid (1), pp. 337-344.

Gentry, M.C., Jacobi, A.M., Heat transfer enhancement by delta-wing-generated tip vortices in flat-plate and developing channel flows, ASME J. Heat Transfer, 124 (6), (2002), 1158-1168 .

Honda, H., Wijayanta, A.T., Takata, N., Condensation of R407C in a horizontal microfin tube, Int. J. Refrig. 28 (2005) 203-211.

Hsieh, S., Wu, F., Tsai, H., Turbulent heat transfer and flow characteristics in a horizontal circular tube with strip-type inserts. Part I. Fluid Mechanics, Int. J. Heat Mass Transf. 46 (2003) 837–849.

Hsieh, S., Liu, M., Tsai, H., Turbulent heat transfer and flow characteristics in a horizontal circular tube with strip-type inserts. Part II. Heat Transfer, Int. J. Heat Mass Transf. 46 (2003) 837–849.

Keklikcioglu, O., Ozceyhan, V., Experimental investigation on heat transfer enhancement of a tube with coiled-wire inserts installed with a separation from the tube wall, Int. Commun. Heat Mass Transf. 78 (2016) 88–94.

Kirkup, L., Frenkel, R. B., An introduction to uncertainty in measurement (Guide to the expression of uncertainty in measurement), Cambridge University Press, New York, 2006.

Lei, Y., Zheng, F., Song, C., Lyu, Y., Improving the thermal hydraulic performance of a circular tube by using punched delta-winglet vortex generators, Int. J. Heat Mass Transf. 111 (2017) 299–311.

Man, C., Xiaogang Lv, Hu, J., Sun, P., Tang, Y., Experimental study on effect of heat transfer enhancement for single phase forced convective flow with twisted tape inserts, Int. J. Heat Mass Transf. 106 (2017) 877–883.

Mohammed, H.A., Hasan, H.A., Wahid, M.A., Heat transfer enhancement of nanofluids in a double pipe heat exchanger with louvered strip inserts, Int. Commun. Heat Mass Transfer 40 (2013) 36–46.

Promvonge, P., Koolnapadol, N., Pimsarn, M., Thianpong, C., Thermal performance enhancement in a heat exchanger tube fitted with inclined vortex rings, Appl. Therm. Eng. 62 (2014) 285–292.

Roy, S., Saha, S.K., Thermal and friction characteristics of laminar flow through a circular duct having helical screw-tape with oblique teeth inserts and wire coil inserts, Exp. Therm. Fluid Sci. 68 (2015) 733–743.

Saha, S.K., Tiwari, M., Sunden, B., Wu, Z., Advances in heat transfer enhancement, Springer, Switzerland 2016. doi: 10.1007/978-3-319-29480-3_1.

Siddique, M., Khaled, A.R.A., Abdulhafiz, N.I., Boukhary, A.Y., Recent advances in heat transfer enhancements: A review report, Int. J. Chem. Eng. 2010 (2010) 1–28.

Skullong, S., Promvonge, P., Thianpong, C., Pimsarn, M., Thermal performance in solar air heater channel with combined wavy-groove and perforated-delta wing vortex generators, Appl. Therm. Eng.100 (2016) 611–620.

Skullong, S., Promvonge, P., Thianpong, C., Jayranaiwachira, N., Thermal behaviors in around tube with quadruple perforated-delta-winglet pairs, Appl. Therm. Eng. 115 (2017) 229–243.

Sundar, L.S., Bhramara, P., Kumar, N.T.R., Singh, M.K., Sousa, A.C.M., Experimental heat transfer, friction factor and effectiveness analysis of Fe_3O_4 nanofluid flow in a horizontal plain tube with return bend and wire coil inserts, Int. J. Heat Mass Transf. 109 (2017) 440–453.

Song, K., Xi, Z., Su, M., Wang, L., Wu, X., Wang, L., Effect of geometry size of curved delta winglet vortex generators and tube pitch on heat transfer characteristics of fin-tube heat exchanger, Exp. Therm. Fluid Sci. 82 (2017) 8–18.

Webb, R.L., Principles of enhanced heat transfer, John Wiley and Sons, Inc, New York, 1994.

White, F.M., Fluid mechanics seventh ed., McGraw-Hill, New York, 2011.

Xu, Y., Islam, M.D., Kharoua, N., Numerical study of winglets vortex generator effects on thermal performance in a circular pipe, Int. J. Therm. Sci. 112 (2017) 304–317.

Yakut, K., Sahin, B., The effects of vortex characteristics on performance of coiled wire turbulators used for heat transfer augmentation, Appl. Therm. Eng. 24 (2004) 2427–2438.

Yakut, K., Sahin, B.., Canbazoglu, S., Performance and flow-induced vibration characteristics for conical ring turbulators, Appl. Energy 79 (2004) 65–76.

Yakut, K., Sahin, B., Celik, C., Alemdaroglu, N., Kurnuc, A., Effects of tapes with double-sided delta-winglets on heat and vortex characteristics, Appl. Energy 80 (2005) 77–95.

Yaningsih, I., Istanto, T., Wijayanta, A.T., Experimental study of heat transfer enhancement in a concentric double pipe heat exchanger with different axial pitch ratio of perforated twisted tape inserts, AIP Conference Proceedings 1717 (2016) 030012, doi: http://dx.doi.org/10.1063/1.4943436.

Yaningsih, I., Wijayanta, A.T., Concentric tube heat exchanger installed by twisted tape using various wings with alternate axis, AIP Conference Proceedings 1788 (2017) 030005, doi: http://doi.org/10.1063/1.4968258.

Yaningsih, I., Wijayanta, A. T., Miyazaki, T., Koyama, S., Thermal hydraulic characteristics of turbulent single-phase flow in an enhanced tube using louvered strip insert with various slant angles, International Journal of Thermal Sciences 134 (2018), 355-362, https://doi.org/10.1016/j.ijthermalsci.2018.08.025.

Zade, N.M., Akar, S., Rashidi, S., Esfahani, J.A., Thermo-hydraulic analysis for a novel eccentric helical screw tape insert in a three-dimensional tube, Appl. Therm. Eng. 124 (2017) 413–421.

CHAPTER 6

Chapter 6

CONCLUSIONS

The study on the heat and mass transfer enhancement of the desiccant dehumidification system was done experimentally. The parameters which affected the performance of the desiccant dehumidification system also was investigated. And their effect into the performance of the system was explained individually. Based on the experimental results, the main findings of the current study can be summarized as:

1. Under parameter studied, experimental results revealed that the Nusselt number (*Nu*) and Sherwood number (*Sh*) of the desiccant dehumidification system did not vary with the variation of switching time. However, the temperature variation showed a significant effect on *Nu* and *Sh*. *Nu* and *Sh* tended to decrease with the increase of adsorption temperature. Switching time is very important to ensure continuous functioning of the system, even though it does not give very different results for *Nu* and *Sh* under the parameters investigated. The highest average *Nu* was 38.02 for T_{ads} of 20 ºC, t_c of 120 min. For the *Sh*, the highest average value was 36.61 for T_{ads} of 20 ºC, t_c of 120 min.

2. The adsorption rate varied slightly with the variation of switching time when the adsorption temperature (T_{ads}) was 20 ºC, whereas for the others, the adsorption values were nearly constant. The adsorption rate is higher when the adsorption temperature is lower. The highest adsorption rate within the desiccant dehumidification system was 0.00809 kg/kg.s for T_{ads} of 20 ºC, t_c of 210 min.

3. The proposed empirical correlations in terms of *Nu* and *Sh* are in good agreement with measurement, with a deviation of less than 15% for each.

4. For the performance of the system, the highest latent heat ratio was found in the value of 0.61 at desorption temperature of 35 ºC, while the highest latent effectiveness was obtained at desorption temperature of 65 ºC. The experimental data and analysis indicate that the reduction of the desorption temperature would increase the latent heat ratio of the desiccant dehumidification system. While the desiccant ability of the system increases with the increase of desorption temperature.

5. The enhancement heat transfer by using delta wing/ winglet vortex generator shows that the highest thermal performance factor was 1.15. It was evaluated by comparing the Nusselt number (*Nu*) and friction factor (*f*) from enhanced tube to the plain tube (tube without insertion). Thermal performance more than one has the meaning that the increase of the heat transfer is more prominent than the increment of friction factor. We found that enhanced tube has a great potential as an effective way to improve the heat transfer due to its ability to increase heat transfer rate up to 177 % with the increase of friction factor by 11.6 times compared to the plain tube.

6. For all the empirical correlations proposed, there is very good agreement between the Nusselt numbers, friction factors, and thermal performance factors determined from experiments and those predicted by the empirical correlations for the heat exchanger installed with double-sided delta-wing vortex generators, with a maximum deviation of ±6%.

7. For adsorption rate measurement, the algorithm for image analysis could semantically segment the adsorption process by creating images which represented the dataset for water level changes inside the evaporator. This result allowed the calculation of the adsorption kinetics. The change of the water level indicates the amount of water vapor uptake by the desiccant material.

APPENDIX

Appendix A

VISUALIZATION AND ANALYSIS OF ADSORPTION KINETICS BY USING IMAGE PROCESSING ALGORITHM

This section highlights a method for determining the adsorption isotherm and kinetics by using an image processing algorithm. Rapid adsorption kinetics is increasingly important because it offers a good mass transfer hence improves the efficiency of the sorption system. For adsorption kinetics, it is required to determine the first stage of the measurement precisely. Therefore, selecting the proper method becomes essential. Simple experimental setup was developed for evaluating adsorption isotherm and adsorption kinetic of Silica gel/ water. The test apparatus comprises of adsorption cell, evaporator/ condenser, piping line, and measurement devices for temperature and pressure. Silica gel types A and RD were employed in the present study as the adsorbent material. A new method is proposed to calculate the adsorption kinetic by using the digital image analyzing. Algorithm for image analysis could semantically segment the adsorption process by creating images which represented the dataset for water level changes inside the evaporator. The results show that the proposed system and method has the ability to determine the water level changes and provide a dataset for analyzing the kinetic rate of the adsorption process.

A.1 Introduction

Recently, the development of an air conditioner by using desiccant material is overgrowing. As it is implemented on the practical application, the understanding of the sorption behavior, including the adsorption isotherm and kinetics is critical to get the optimum design (Wang et al., 2007). Additionally, mass transfer kinetics is also essential because the sorption performance depends on the dynamic behavior of the adsorbed molecules onto the sorbent material (Bourding et al., 1998). Fast adsorption kinetics guiding to the improvement of adsorbent efficiency (Mohammadi et al., 2011, Xia et al. 2016). Many literatures focused on the study of adsorption isotherm and adsorption kinetics of the various adsorption material for different applications, methods, and parameters.

Liapis et al. (1992) and Huang et al. (1995) developed and constructed the system for investigating adsorption and desorption rate by using differential sorption bed. The differential sorption bed system is working based on volumetric methods. The amount of gas adsorbed was calculated by using the change of the volume corresponding to the change of the temperature and pressure. Data during the experiment was collected under isothermal conditions. Their results were considered as the preliminary data for their future work. Bajpai and Bajpai (1995) studied adsorption experiments of the polyacrylamide (PAM) towards iron oxide. The effect of the PH of the adsorption medium was conducted to observe the adsorption rate behavior. The adsorption rate decreased with the increased of the PH. Moreover, the initial rate of adsorption was the foremost concerned of their study. The addition of salt concentrations and molecular weight of PAM was observed to investigate the initial rate. They found that the initial rate decreases with increasing salt concentrations and molecular weight of the PAM. Rutherford and Do (2000a, 2000b) also developed the different methods to obtain the adsorption isotherm and kinetics. They used permeation and batch adsorption and compared the results. In the case of batch adsorption, the material was filled in the batch which contains fluid. The amount of adsorbed was calculated by measuring the change of the concentration in the batch fluid. While for the permeation method, the fluid was penetrated in the permeable material so that the porous barrier will be formed. The results show the consistency data form those two methods.

Gautam et al. (2010) characterized the adsorption isotherm and kinetics of the activated carbon on tartarazine concentration by using batch mode. The effect of the initial concentration, PH, contact time, and temperature was investigated to determine their sorption behavior. Their results show that the rapid adsorption was shown in the first stage then increased until reach the equilibrium. It was required 60 min to reach the equilibrium conditions. The initial concentration affected the speed of tartarazine removal. Increasing the initial concentration will speed up the removal of tartarazine. Al-Jabari (2016) studied the kinetics model for adsorption of mineral particles and compared the result between the Langmuir model and mass transfer.

The model includes the effect of the particle dosage and the ratio between the initial mass of pollutant to the maximum adsorbed mass. They found that faster adsorption can be obtained by decreasing the ratio of initial mass pollutant to the maximum adsorbed mass. Teo et al. (2017) studied the adsorption isotherms and adsorption kinetics of the Aluminium Fumarate and water adsorption. The measurement of the adsorption isotherm and kinetics was done by using gravimetric analyzer under static and dynamic conditions. The adsorption temperature was adjusted from 25 ^{o}C to 60 ^{o}C. They found that water uptake increases with the increase in pressure. Moreover, longer cycle time is required for the highest adsorption temperature to achieve the equilibrium condition. Alshameri et al. (2018) presented the adsorption behavior, including the adsorption isotherm and kinetics by using the experimental batch method. The adsorption of ammonium by different natural clay minerals was investigated by adjusting PH and adsorbent dosage. They found that when the reaction time increased the removal efficiency was also increased, which means that the rapid adsorption kinetics could increase the removal efficiency. Yang et al. (2018) conducted the adsorption behavior and kinetics investigations by using volumetric methods. Activated carbons were employed as the raw material by adjusting their pore structure. They found that increasing the specific surface area will increase the adsorption rate.

Through the literature study above, it is crucial to choose the proper method as it might be affected by the measured sorption rate. Moreover, the value of the initial stage is necessary for data quantification since it is defined as the dynamic sorption before it reaches the steady state conditions. Although there have been many investigations focused on the adsorption behavior measurement, the existing literature is not sufficient provides the studies concerning the initial stage of kinetics part. Therefore, this work provides an experimental study of the adsorption behavior which concerns in the kinetics parts. A new method combined with an algorithm by using digital image processing is proposed to evaluate the sorption rate. Image processing to be more promising due to their flexibility to analyze any object with a complex dimension and shape (Li et al., 2014). The present study utilized the digital image processing which drives an automatic process to discover and collect the dataset of water level changes by detecting the pixel value in the designated point.

A.2 Experimental Methods

A.2.1. Experimental Facility

The schematic diagram and pictorial view of the test apparatus are shown in Figs. A.1 (a) and (b). The test apparatus consists of adsorption cell, evaporator/ condenser, piping line, video camera, and measurement devices for the pressure and temperature. Adsorption cell was stainless-steel cylinder with 70.3 mm inner diameter, 76.3 mm outer diameter and 50 mm height. Evaporator/ condenser was comprised of sight glass which allowed the reading of the water level difference. It has an inner diameter of 6 mm, an outer diameter of 8 mm and a height of 100 mm. The piping line of the system was made of stainless steel tube with 3/8 inches diameter. It is also equipped with the tape heater to keep the pipe temperature higher than the adsorption temperature so that the condensation does not occur. A 4K video camera was employed to record the adsorption process during the experiment. The distance of the lens and observation area was adjusted in the length of 88.45 mm (the maximum distance which could be reached without decreasing the resolution of the video). For all the experiment, the video was saved in the MP4/iFrame format.

Two pressure sensors were employed to measure the pressure within the system. Pirani vacuum gauge with a measurable pressure range from 5×10^{-2} to 1×10^{5} Pa and measurement accuracy of ± 10% from 1×10^{-1} to 1×10^{4} Pa and 20% from 1×10^{4} to 1×10^{5} Pa was used to make sure the system could reach vacuum conditions. While the second pressure transducer has a measuring range of 0 – 0.06 MPa. Three K type thermocouples with an accuracy of ± 0.05 ^{o}C were utilized to measure the temperature of the adsorption cell, adsorbent material, and evaporator/ condenser. For the data arrangement, the initial and final data for pressure and temperature were recorded by using a data acquisition unit (DAQMASTER: MX 100; accuracy = ± 0.01%).

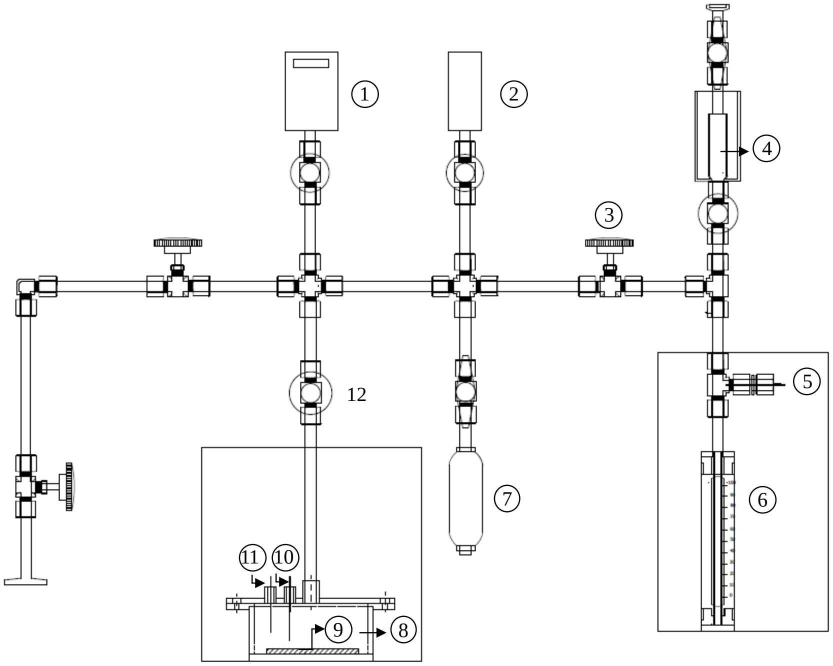

(1) Pirani vacuum gauge, (2) Pressure transducer, (3) Metering valve, (4) Water storage, (5); (10); (11), Thermocouples, (6) Evaporator, (7) Liquid nitrogen vessel, (8) Adsorption cell, (9) Sample, (12) Valve

(a)

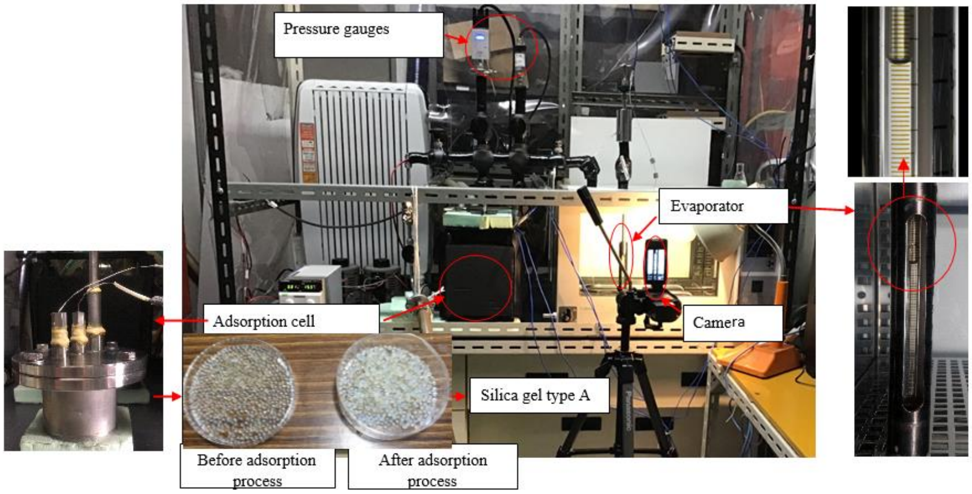

(b)

Figure A.1. Test apparatus for adsorption isotherm and rate; (a) schematic diagram, (b) pictorial view.

A.2.2. Experimental Procedure

This experiment is aimed to investigate the adsorption behavior (isotherm and kinetics) of Silica gel type A and RD towards the water. For preparation, the sample is regenerated in the oven at 120 ^{o}C for 12 hr to remove the excess moisture. After regenerating, the sample is installed in the adsorption cell and continued with heating and vacuuming inside the system at 80 ^{o}C for 12 hr. During the evacuation process, the pressure inside the system could reach until 0.5 Pa. When the heating finished, the temperature of the water bath is adjusted to the desired adsorption temperature while continuing with the evacuation. After reaching the desired temperature, the valve corresponds to the adsorption cell is fully closed. Following that, the metering valve is also closed to prevent the water suction by vacuum pump when adding the distilled water to the evaporator. To avoid the air trapped in the water, the water should be freeze in the water container by using liquid nitrogen.

When the pressure of the evaporator reaches the partial pressure of the designated temperature of the evaporator, the metering valve is opened to allow the vapor filled out the piping line. After the pressure and temperature of the system become steady, the valve which is connected to the adsorption cell is opened, permitting the adsorbent released the heat of adsorption. The data and video recording starting at the same time when opening the adsorption cell valve. During the experiment, the adsorption temperature is adjusted in the value of 20 ^{o}C, 30 ^{o}C, and 40 ^{o}C. While for the evaporator temperature, to get the adsorption step with different relative pressure, the temperature is adjusted by increasing the temperature for every two ^{o}C for adsorption temperature of 20 ^{o}C and every five ^{o}C for adsorption temperature of 30 ^{o}C and 40 ^{o}C. For all variations, the lowest evaporator temperature was adjusted in the value of 12 ^{o}C. The maximum evaporator temperature is adjusted as closely as to the adsorption saturation temperature with the maximum relative pressure of 0.9. The adsorption process finished when the temperature and pressure reach the equilibrium conditions.

A.2.3. Experimental data analysis

1) Image Processing Analysis

The visualization and analysis of the adsorption behavior particularly for adsorption kinetics by using digital image processing are presented in this study. The process during the adsorption was recorded by using the video camera which has a property as shown in Table A.1.

Table A.1. The properties of the video for adsorption process

Property	Values
Frame width	960
Frame height	540
Data rate	12181 kbps
Total bitrate	12435 kbps
Frame rate	29.97 frames/ second
File type	.MP4

The initial image processing performed by converting the video into images based on the total number of frames. Figure A. 2 shows the RGB image while Table A. 2 shows the properties of the raw image.

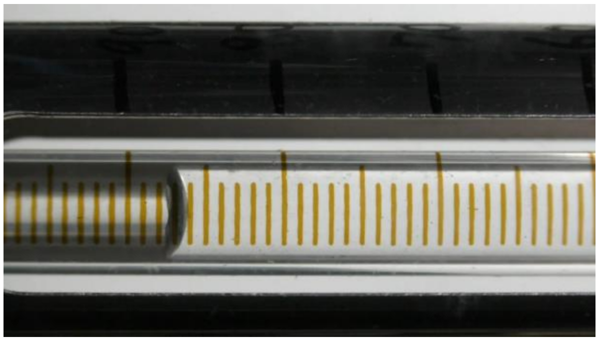

Figure A.2. RGB image after extracting the video.

Table A.2. The properties of the RGB image.

Property	Values
Dimension	960 × 540
Width	960 pixels
Height	540 pixels
Horizontal resolutions	72 dpi
Vertical resolutions	72 dpi
Bit depth	24
File type	.tif

The algorithm for image processing is coded in MATLAB R2018b academic version which is equipped with the image processing toolbox. Image processing algorithm capable of detecting the interface between the water and vapor which later determined as the water level. The raw RGB image was extracted to select one component of the matrix color. Each color channel of the RGB image will appear as a grayscale image. After cropping and rotating processes, the image then processed by using thresholding to get the binary image. In the threshold processed, one matrix component of RGB was selected and converted into a binary image. Transforming the image by using thresholding resulting only black and white intensity image. By choosing the thresholding level value, the algorithm will define all the pixels with the values less than level as black (0) while the other values as white (1). To improve the black and white intensity, the image is processed by transforming the binary image into the negative image. The negative image is aimed to reverse the intensity of the image. Black and white are reversed, so that zeros become ones and vice versa. This procedure allows the program for tracking and selecting the interface which has the light intensity/ white (1).

The binary image then transformed into a label matrix for image sizing. The pixel value of the interface can be determined by searching the minimum intensity in a single component grayscale image. The algorithm could count and get the minimum pixel value along x-columns in each y-rows. The projecting of the interface showing the coordinate according to the pixel numbers of the designated point which represent the pixel height. The process is in sequenced and applied for all the images by using looping function. The determination of water level from pixel into mm is done by dividing each of its pixel values by the total number of pixels in the image. Finally, the generated data was collected into the excel file.

2) Adsorption isotherm and kinetics

To give a better understanding of adsorption uptake calculation, the illustration of the adsorption phenomenon inside the test apparatus is presented in Fig. A.3.

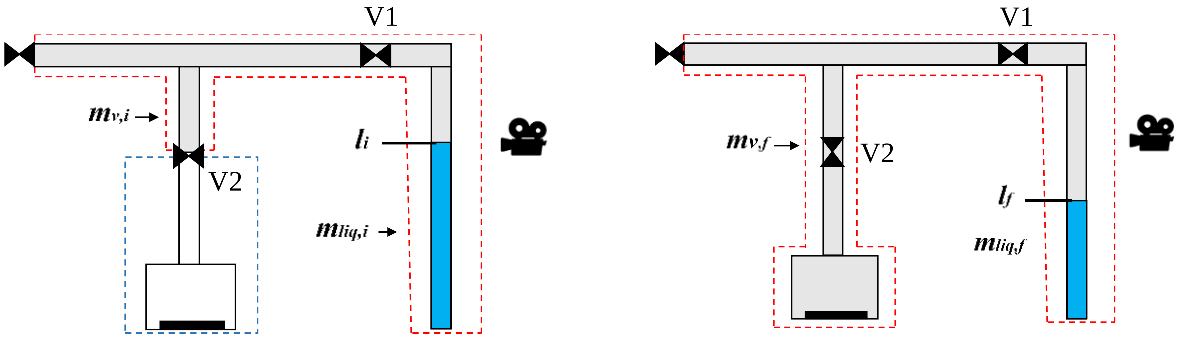

(a)

(b)

Figure A.3. Adsorption phenomenon during the adsorption process; (a) initial condition, (b) equilibrium condition.

Based on Fig. A.3, the step for calculating the adsorption uptake can be explained as follows:

Step 1 (initial condition)

In the initial condition, V1 is opened which permit the vapor flowing through the pipe, while V2 is closed. After the temperature and pressure become steady, the initial condition in step 1 can be calculated by using the following equation:

$$m_1 = m_{v,i} + m_{liq,i} = \rho_v (P_{evap}, T_{evap}) V_p + \rho_{liq} (P_{evap}, T_{evap}) A_{evap} l_i \tag{1}$$

where, *m* stands for mass, ρ for the density, *P* for the pressure, *T* for the temperature, *A* for the area, *V* for the volume and *l* for the height of the water level. While the subscript *v* stands for vapor, *liq* for liquid, *i* for initial, *p* for pipe and *evap* for evaporator.

Step 2 (equilibrium condition)

The adsorption begins when V2 is opened. After several hours, the system will reach equilibrium conditions, and the total mass inside the system is determined as:

$$m_{eq} = m_{v,f} + m_{liq,f} + m_{adsorbed} = \rho_v (P_{eq}, T_{eq}) V_t + \rho_{liq} (P_{eq}, T_{eq}) A_{evap} l_f + m_{adsorbed} \tag{2}$$

where subscript *eq* stands for equilibrium, *f* for final, *adsorbed* defined the mass which adsorbed by the desiccant material.

Based on the conservation of mass, the total mass adsorbed by the adsorbent can be calculated as follows:

$$m_1 = m_{eq} \tag{3}$$

$$m_{v,i} + m_{liq,i} = m_{v,f} + m_{liq,f} + m_{adsorbed} \tag{4}$$

$$m_{adsorbed} = (m_{v,i} + m_{liq,i}) - (m_{v,f} + m_{liq,f}) \tag{5}$$

Then, And the adsorption capacity can be examined by using the following equation:

$$w = \frac{m_{adsorbed}}{m_{ads}} \quad (kg\, vapor / kg\, ads) \tag{6}$$

Finally, the amount of the adsorption uptake in the nth measurement can be determined by:

$$w_n = w_{n-1} + w \tag{7}$$

where w is the adsorption uptake, and subscript n and n-1, is the adsorption uptake in step n and n-1, respectively.

A.3 Results and Discussion

A.2.1. Image Processing Algorithm

The image analysis technique is developed based on the image processing algorithm. The basic operation of the algorithm is performed by the pixels of the image where for each pixel correspond to the elements of the matrices. In this study, the developed algorithm is constructing to detect and calculate the pixel value of the interface between the water and vapor, therefore the dataset of the water level changes can be obtained. First step algorithm used in the present study is the extraction of color channel of the raw RGB image. The RGB image has a dimension of m row, n column and three-layer intensities which represents red, green, and blue. The collective amount of each channel can be extracted based on the following equations:

$$r = \frac{R}{R+G+B} \tag{8}$$

$$g = \frac{G}{R+G+B} \tag{9}$$

$$b = \frac{B}{R+G+B} \tag{10}$$

where r, g, and b represent red, green, and blue, respectively. Applying the algorithm to the raw image (Fig. A.2), resulting in the new images which show the monochrome grayscale array based on individual color channel red, green, and blue. Figures A.4 (a), (b) and (c) shows the image after extracting for each individual color channel.

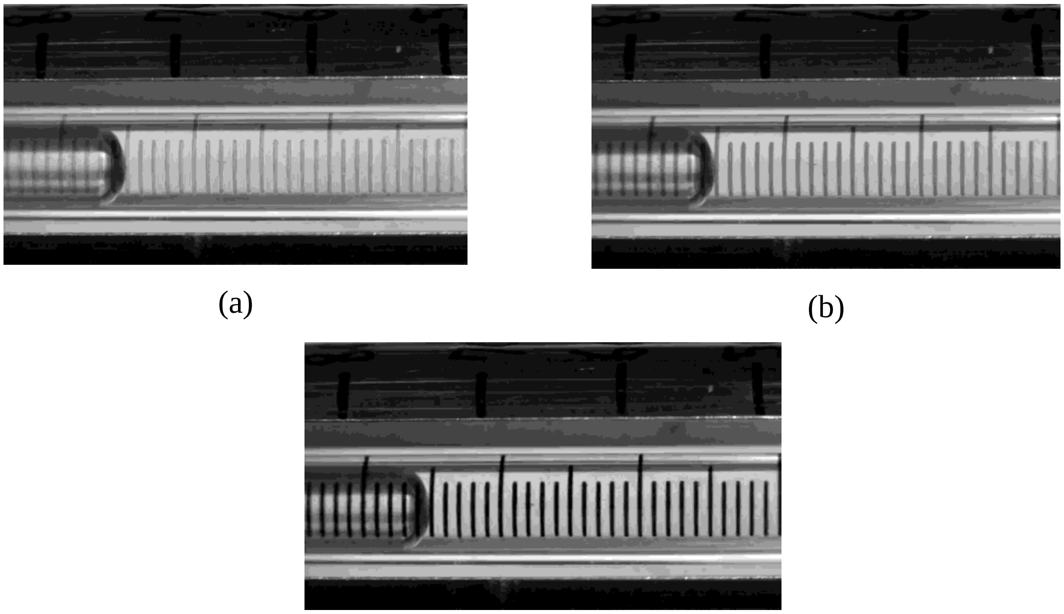

(a) (b)

(c)

Figure A.4. Individual color channel extracted from RGB image; (a) red, (b) green, (c) blue.

The next algorithm will only use one of the color channels to perform the next sequence processes. Considering Fig. A.4, the cropping method was applied to remove the undesirable region. The boundary region of the image was selected by using the rectangular cropping tool. The selection region is taking consideration of the area that includes the interface between the water and vapor. Figure A.5 shows the results after cropping method.

Figure A.5. An image after cropping process.

After the cropping process, it shows that the coordinates of the image for detecting the water level is reversed. Therefore, transformation by rotating the image is required. Not only that, but the transformation of the image also could improve its appearance. The rotation of the image is based on transforming/ mapping the variables of pixel intensity of the input image at the location (x_0, y_0) to the new location of the output image at (x_1, y_1) by an angle of θ. The transformation of the image is based on the following equation.

$$A = \begin{bmatrix} \cos\theta & -\sin\theta \\ \sin\theta & \cos\theta \end{bmatrix}, B = \begin{bmatrix} x_0 \\ y_0 \end{bmatrix} \tag{11}$$

where x_o and y_o are the initial coordinates of the image. Figure A.6 shows the results of the image after rotating process.

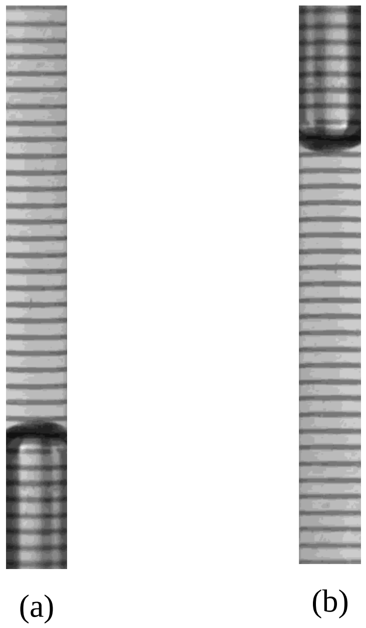
(a) (b)

Figure A.6. Image after rotating process; (a) 90°, (b) 270°.

The detection of interface between the water and vapor is required the algorithm which could be able to detect and count the sudden change of the color intensity. For this purpose, the detection of the differences can be done by thresholding the grayscale level to a binary level. Binary-level has two levels of color (black and white). Black color has an intensity value of 0 while the white color has an intensity of 1. By adjusting the scale of the threshold value, any color which has the value beyond the thresholding value will be detected as 0 (black) while others are 1 (white). The output of the segmented image (*g*) from the transformation input image (*f*) follows the simple thresholding rule of (Kotte et al., 2018):

$$g(i,j) = 1 \text{ for } f(i,j) \geq th. \quad (12)$$

$$g(i,j) = 0 \text{ for } f(i,j) < th. \quad (13)$$

where *th.* is the thresholding value.

After converting into a binary image, enhancing the quality of the image is continued with the transformation into a negative image. This transformation is aimed to improve the white color detail which embedded in the dark regions of the image. The following expression denotes the transformation to the negative image:

$$s = L - 1 - r \quad (14)$$

where *s* is the pixel value after processing, *r* is the pixel value before processing and *L* is the gray level value. Figures A.7 (a), (b), (c) and (d) show the results of the image after transforming by using thresholding and negative image method. Figures A.7 (a) and (b) are images after converting into a binary image by using thresholding method; (a) is the image with 90° rotation, while (b) is the image with 270° rotation. Figures A.7 (c) and (d) are images after transformation from the binary image to negative image; (c) is the image with 90° rotation, while (d) is the image with 270° rotation.

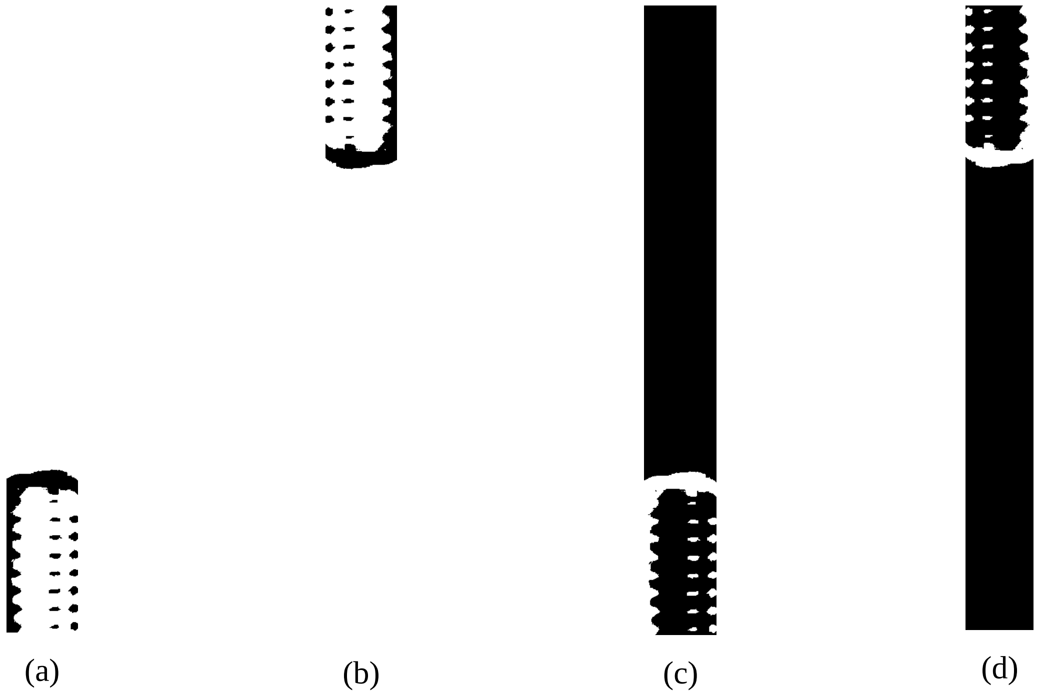

Figure A.7. Transformation of the image; (a) binary image of 90° rotation, (b) binary image of 270° rotation, (c) negative image of 90° rotation, (d) negative image of 270° rotation.

Figure A.7 shows clearly the interface between the water and vapor. The region of the interface can be read by searching for the location which has the pixel value of 1 (white color) from Figs. A.7 (c) and (d). Additionally, the maximum or minimum pixel value of the y-rows along x-columns can be obtained by using a boundary tracing algorithm. The maximum or minimum pixel value of y in the present study depends on the degree of rotation. In the case of the image, y increases downward while x increases to the right. Therefore, if the image rotation is 90° the pixel value in the interface can be detected by using minimum y. While for the image rotation 270°, the pixel value is defined by maximum y. Following code is used for interface detection:

y_{min} = min (find (I (:, y));

y_{max} = max (find (I (:, y));

Figures A.8 (a) and (b) show the results from the boundary tracing algorithm for identifying pixel values. The find commands seek the locations which have non-zero values and stores to the matrix. The coordinates (x, y) are arranged based on the pixel numbers.

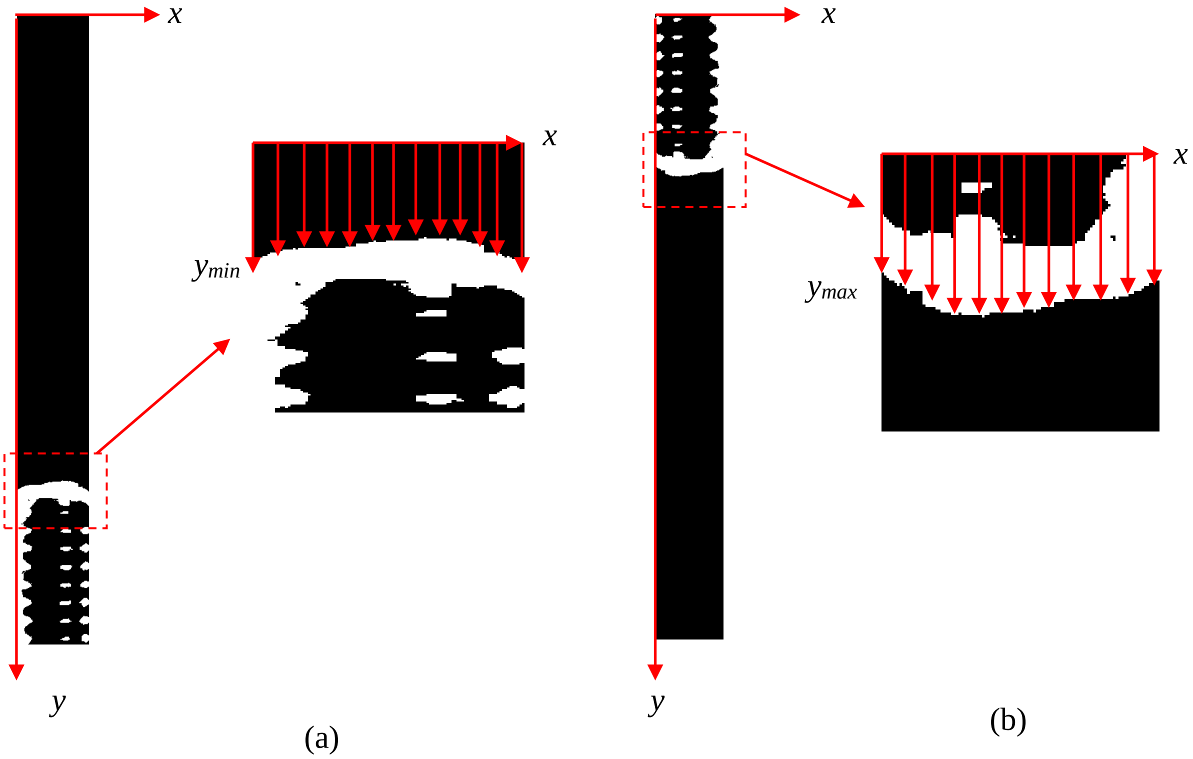

(a)

(b)

Figure A.8. The detection of pixel values in y-column; (a) minimum value, (b) maximum value.

Figures A.9 (a) and (b) show the results of the pixel value detection from the developed algorithm proposed in this study. The original size of the cropped image was 110 × 960 pixels for width and height, respectively. While the results of reading from the proposed algorithm have the same size of 110 pixels of width and 960 pixels of height. Thus, it is proof for the validation of the image size. The size of the image is very important since it used for the calculation of the water level.

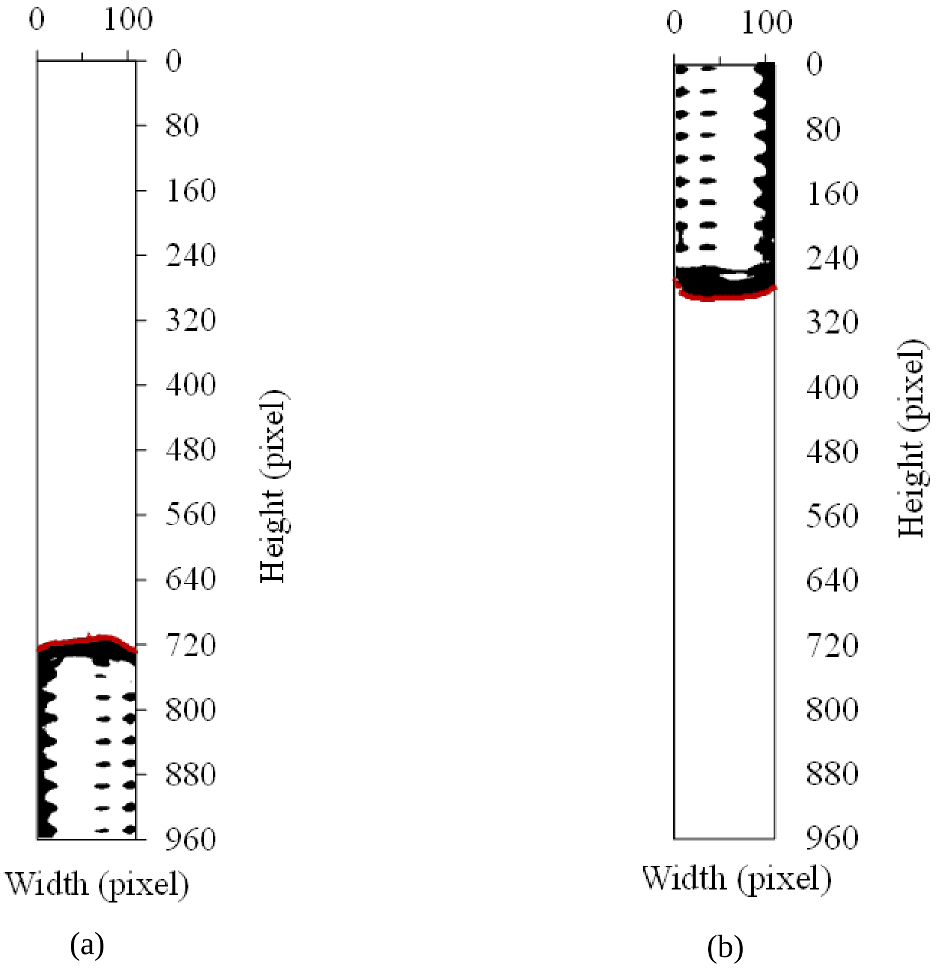

Figure A.9. Pixel value detection for the images with (a) 90° rotation, (d) 270° rotation.

The red line in Figs. A.9 (a) and (b) shows the boundary of the interface which defined water level height. When it plots in the (x, y) coordinates, the y coordinate indicates the pixel value of the water level height. For each image, which represents by each frame, the water level is calculated by the average value of y-column along x-axis. The calculation for pixel value for each image is as follows:

$$\bar{y} = \frac{1}{n}\sum_{i=1}^{i=n} y_i \tag{15}$$

where $\bar{y}$ is the average of pixel value, y_i is the pixel value of y column in i row, n is the total rows. The water level height for each frame is determined by converting the pixel into mm. The conversion is based on extrapolation methods. The calculation is given by:

$$h_k = H - \frac{(H - h_0)(Y - y_k)}{(Y - y_0)}, \text{ for } k = 1 \text{ to } j \qquad (16)$$

where h_k is the water level in frame k, H is the total height within the frame, h_o is the initial water level, Y is the total pixel value within the frame, y_o is the initial pixel value of h_o, y_k is the pixel value in frame k, k is the frame number, j is the total number of frames. Figures A.10 and A.11 show the graph for the pixel value within 600 number of frames and the conversion of pixel value into mm, respectively.

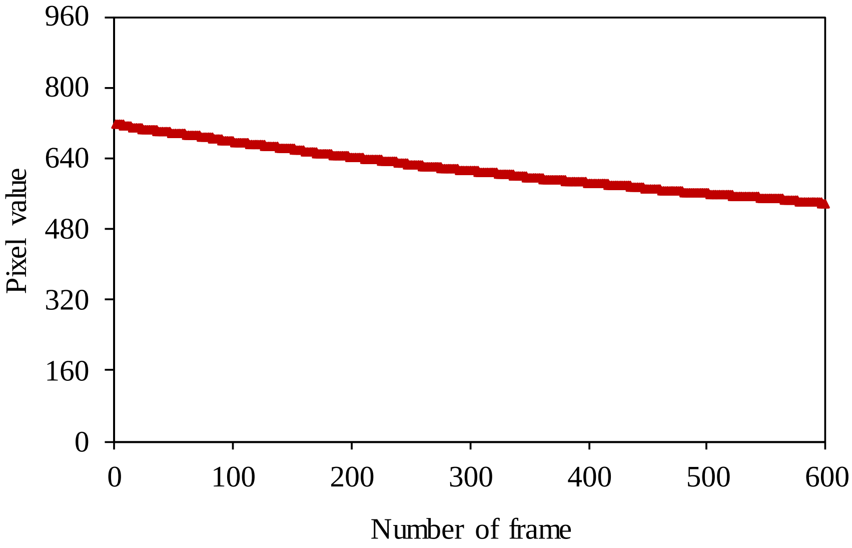

Figure A.10. The pixel value for 600 number of frames.

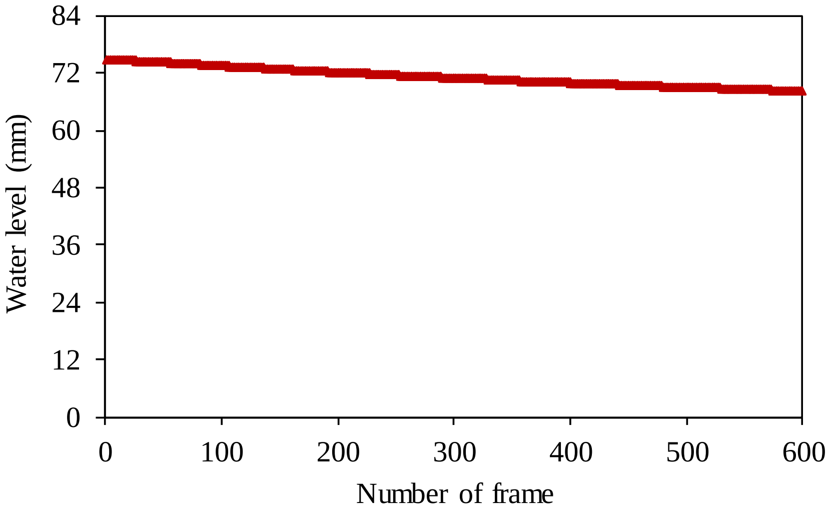

Figure A.11. The water level for 600 number of frames.

The validation results of the image processing algorithm can be done by evaluating the results of water level from the image processing with the real water level changes from the experiment (read by using a microscope). Figures A.12 (a) and (b) show the initial water level at frame no. 1 and water level at frame no. 600.

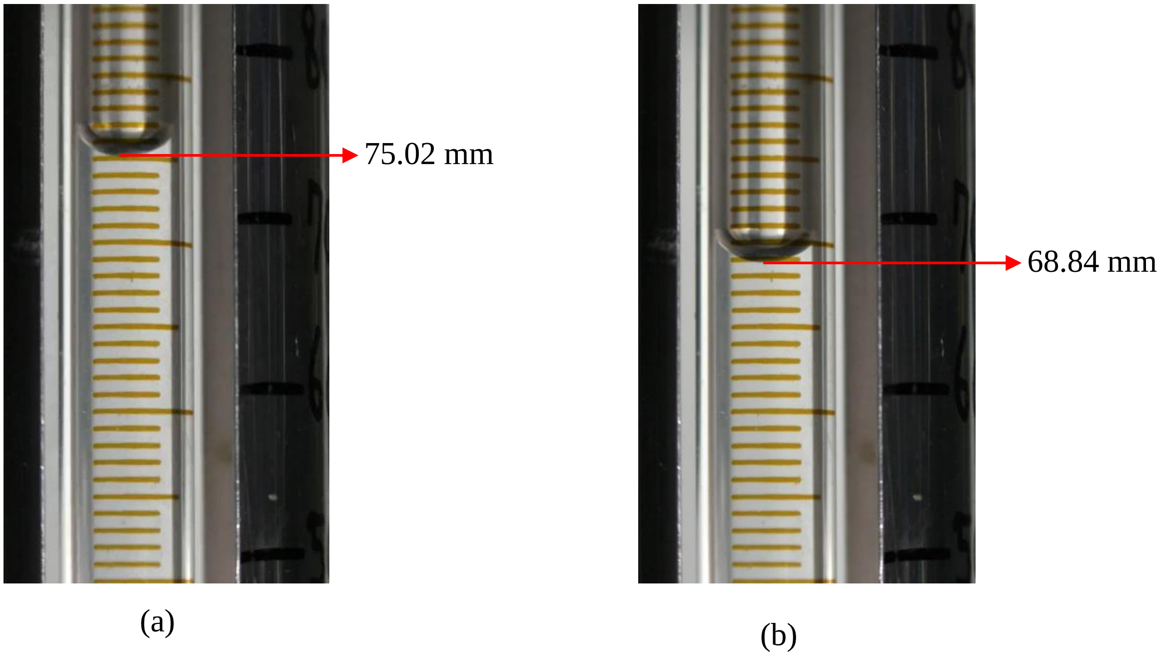

(a) (b)

Figure A.12. The water level at (a) frame no. 1, (b) frame no. 600.

The pixel value of frame no.1 is 717.23 which is equal to 75.02 mm, while the pixel value at frame no. 600 is 540.04 which is equal to 68.32 mm. It has a small discrepancy between the water level reading by the algorithm and real experiment using a microscope. However, the deviation is in the percentage of 0.76%. Therefore it offers a proper validation for the algorithm.

A.2.2. Adsorption Isotherm and Kinetics

The validation of the test apparatus was done by assessing the current data to the data obtained from Chua et al., 2012. Figures A.13 and A.14 show the comparison of both results for Silica type A and RD, respectively. In the case of silica gel type A, the water uptakes were overestimated the value from Chua et al. by the maximum discrepancy of 6%. While for silica type RD, the water uptake values were less than 7% as compared to the reference data. These results offered a good consistency water vapor uptake with the reference.

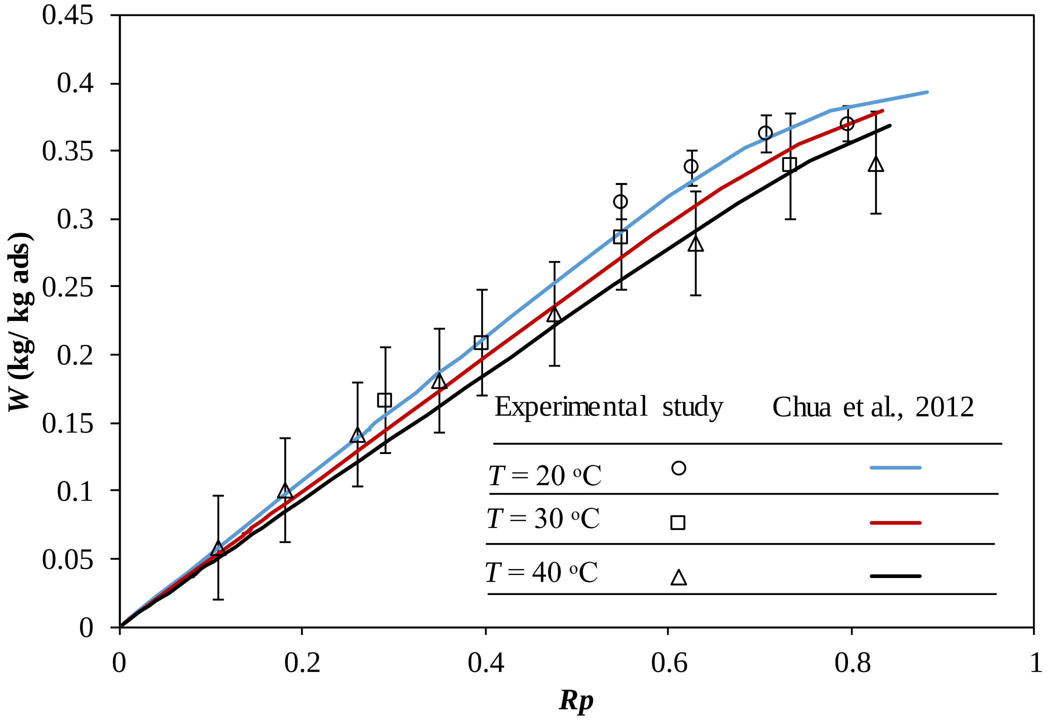

Figure A. 13. Adsorption isotherm for Silica gel type A.

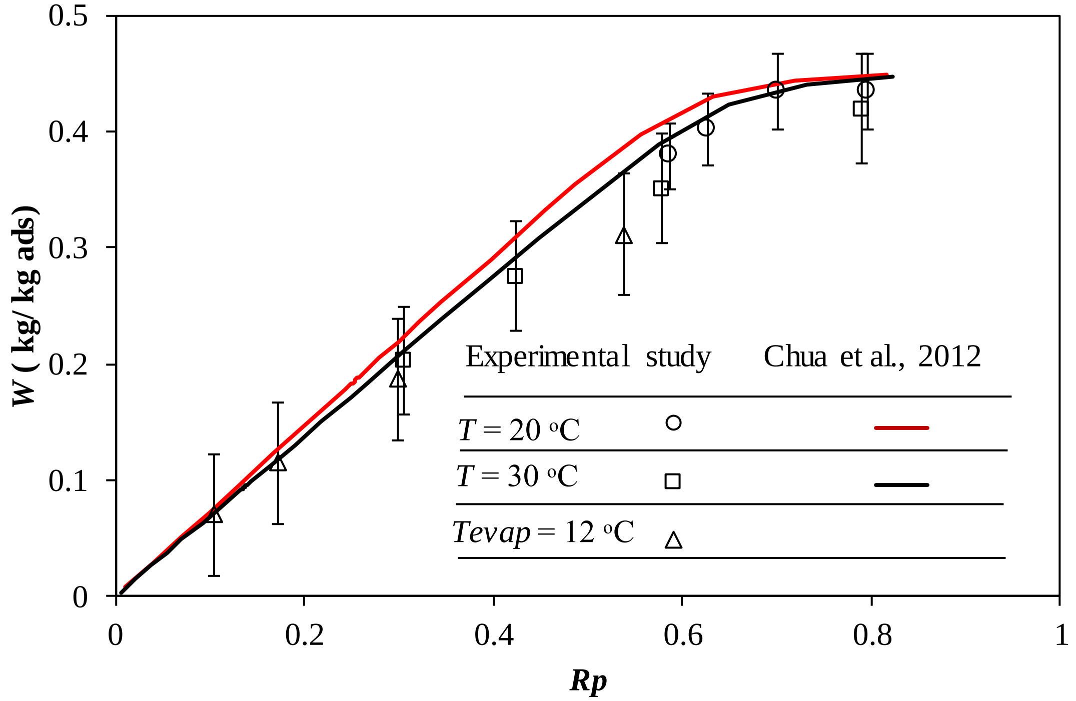

Figure A. 14. Adsorption isotherm for Silica gel type RD.

The adsorption equilibrium of the Silica gel is given by:

$$w^{*} = k\left(P / P_{s}\right)^{1/n} \tag{17}$$

where w^{*} is the water uptake amount in equilibrium conditions, P is the partial pressure, P_s is the saturation pressure, k and n are the constant. The constants for silica type A were found in the value of; k = 0.443 and n = 1.3. For silica type RD, the values of k and n were given as k = 0. 552 and 1.12, respectively.

The adsorption kinetics of the material was fitted by using LDF model. The LDF model equation is given as:

$$\frac{dw}{dt} = k_{s}a_{p}\left(w^{*} - w\right) \tag{20}$$

where the $k_s a_p$ is overall mass transfer coefficient and defined as:

$$k_{s}a_{p} = \frac{15D_{s}}{r_{p}^{\;2}} \tag{19}$$

the surface diffusion, D_s, in Eq. 19 is given by:

$$D_{s} = D_{s0}\exp\left(-\frac{E_{a}}{RT}\right) \tag{18}$$

LDF model fitting parameters are summarized in Table A.3.

Table A.3. LDF fitting parameters.

Parameters	Value	Units
D_{so}	2.22×10^{-4}	m^2/s
E_a	4.2×10^{4}	J/mol
R	8.314	kg/kg
r_p	6.1×10^{-4}	m

The results of the adsorption kinetics for different points of temperature and pressure within the range of the study are depicted in Figs. A.15, A.16 and A.17.

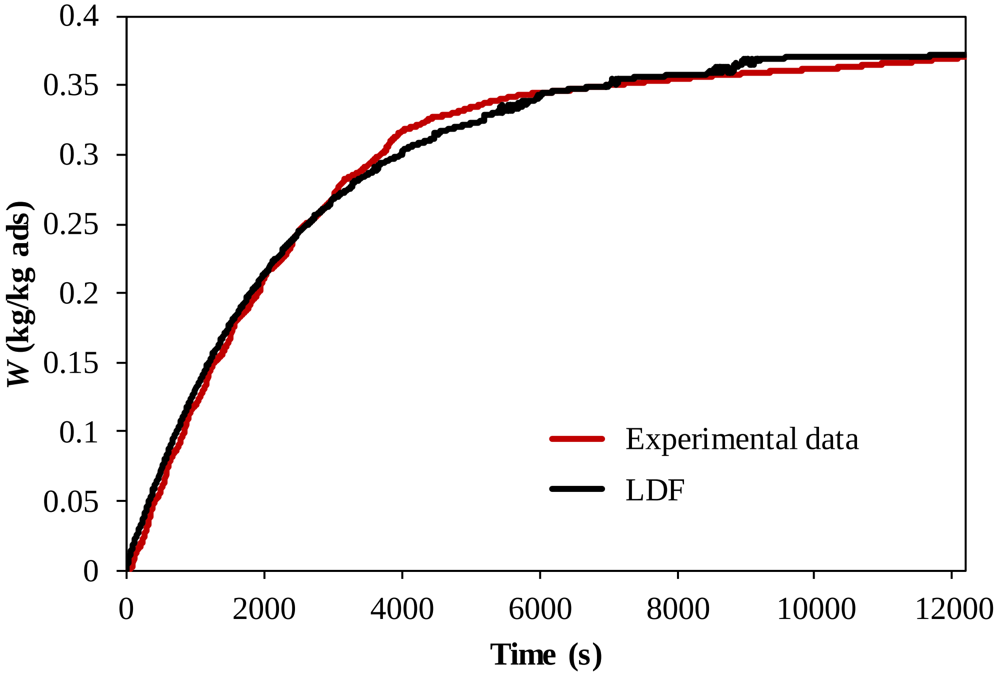

Figure A.15. Adsorption rate for Silica type A at T_{ads} = 20 °C, T_{evap} = 12 °C.

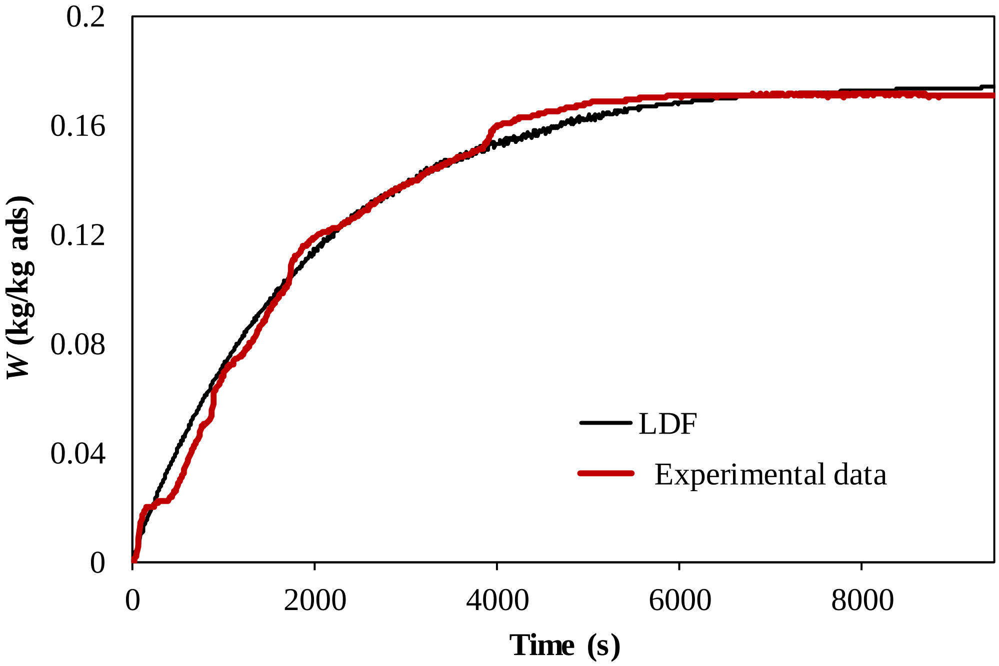

Figure A.16. Adsorption rate for Silica type A at T_{ads} = 30 °C, T_{evap} = 12 °C.

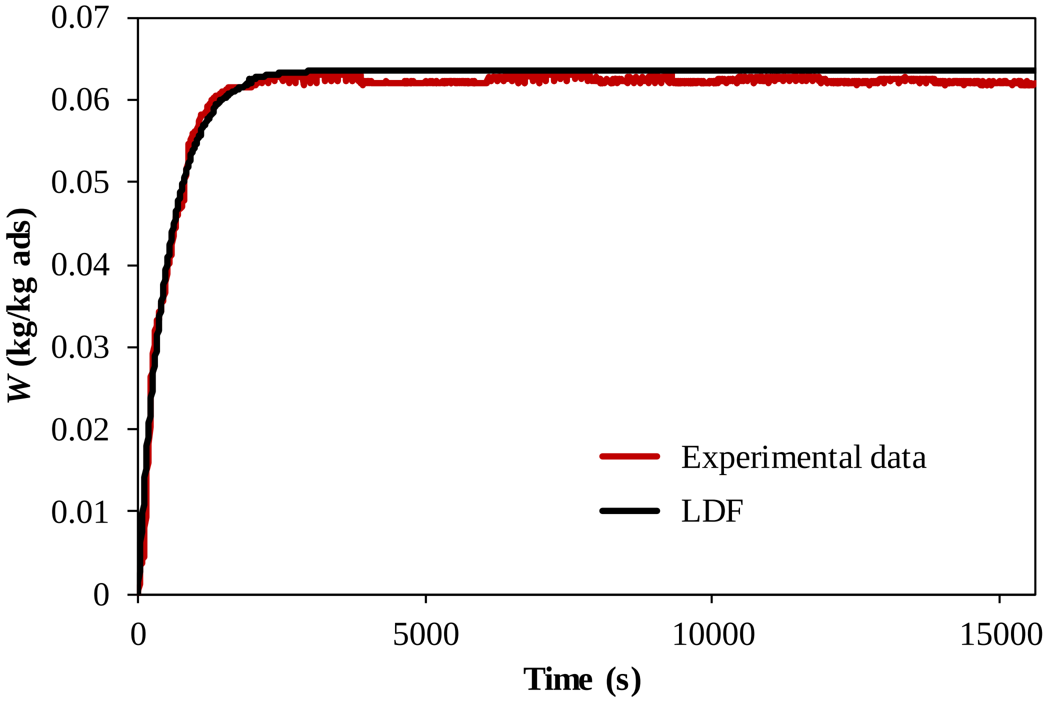

Figure A.17. Adsorption rate for Silica type RD at $T_{ads} = 50\ ^{o}C$, $T_{evap} = 12\ ^{o}C$.

The water level data successfully represents the water uptake amount for the calculation of adsorption rate. The plotted adsorption rate for the experimental data in Figs. A.15-A.17 were shows the dynamic and static region of the adsorption process. The dynamic range of the adsorption process almost for all cases finished at 3000s. The total time of dynamic range is essential to define the mass transfer efficiency. Fast adsorption kinetics guiding to the improvement of adsorbent efficiency (Mohammadi et al., 2011). As compared to the LDF model, the experimental data could provide a similar tendency with small differences. Therefore, the method promises to be useful for studying the kinetics of such adsorption processes.

A.4 Conclusions

The development of the experimental setup for assessing the adsorption behavior through the adsorption isotherm and kinetics was done. Silica gel types A and RD were selected as the adsorbent material. The image processing algorithm was also developed and proposed to find the water level changes during the adsorption process. The conclusion can be drawn based on the experimental results; the method promises to be useful for studying the adsorption behavior for isotherm and kinetics. The proposed image processing algorithm successfully creating the dataset for the water level data indicates by the small discrepancy of less than 1% as compared to the data collected by using the microscope. The calculation of the water uptakes based on the water level data shows a good agreement with the reference for both adsorption isotherm and kinetics.

Nomenclature

A = area (m^2)
l = liquid height (m)
m = mass (kg)
P = Pressure (Pa)
T = Temperature (^oC)
V = volume (m^3)
ρ = density (kg/m^3)
D_s = surface diffusivity (m^2/s)
D_{so} = pre-exponent constant (m^2/s)
E_a = activation energy (J/mol)
$k_s\, a_p$ = overall mass transfer coefficient (1/s)
R = gas constant (J/mol.K)
T = adsorption temperature (^oC)
t = time (s)
w = amount adsorbed (kg vapor/kg ads)
w^* = equilibrium amount adsorbed (kg vapor/kg ads)

Subscripts:

ads = adsorbate

i = initial

eq = equilibrium

evap = evaporator

f = final

liq = liquid

p = pipe

t = total

v = *vapor*

References

Al-Jabari, M., Kinetics model for adsorption on mineral particles comparison between Langmuir kinetics and mass transfer, Environmental Technology & Innovation 6 (2016) 27-37.

Alshameri, A., He, H., Zhu, J., Xi, Y., Zhu, R., Ma, L., Tao, Q., Adsorption of ammonium by different natural clay minerals: Characterization, kinetics and adsorption isotherms, Appl Clay Sci. 158 (2018) 83-93.

Bajpai, A. K., Bajpai, S. K., Kinetics of polyacrylamide adsorption at the iron oxide-solution interface, Colloids Surf. A Physocochem Eng Asp 101 (1995) 21-28.

Bourdin, V., Gray, P. G., Grenier, Ph., Terrier, M. F., An apparatus for adsorption dynamics studies using infrared measurement of the adsorbent temperature, Review of Scientific Instruments 69 (2130) (1998), https://doi.org/10.1063/1.1148911.

Chua, H. T., Ng, K.C., Chakraborty, A., Oo, N. M., Othman, M. A., Adsorption characteristics of silica gel + water systems, J. Chem. Eng. Data 47 (2002) 1177-1181.

Gautam, P. K., Gautam, R. K., Banerjee, S., Lofrano, G., Sanroman, M. A., Chattopadhyaya, M. C., Pandey, J. D., Preparation of activated carbon from Alligator weed (Alternenthera philoxeroids) and its application for tartrazine removal: Isotherm, kinetics and spectroscopic analysis, J. Environ. Chem. Eng. 3 (2015) 2560-2568.

Huang, Y. H., Liapis, A.I., Xu, Y., Crosser, O. K., Johnson, J. W., Binary adsorption and desorption rates of propylene-propane mixtures on 13X molecular sieves, Sep. Technol. 5 (1995) 1-11.

Kotte, S., Kumar, P. R., Injeti, S. K., An efficient approach for optimal multilevel thresholding selection for gray scale images based on improved differential search algorithm, Ain Shams Engineering Journal 9 (2018) 1043-1067.

Liapis, A. I., Findley, M. E., Johnson, J. W., Jetz, S., Finefrock, Q. B., Rates and equilibria of adsorption and desorption of propane and propylene on 13 X molecular sieves determined experimentally using a differential sorption bed system, Sep. Technol. 2 (1992) 141-154.

Li, L., Gong, M., Chui, Y. H., Schneider, M., A MATLAB-based image processing algorithm for analyzing cupping profiles of two-layer laminated wood products, Measurement 53 (2014) 234-239.

Mohammadi, N., Khani, H., Gupta, V.K., Amereh, E., Agarwal, S., Adsorption process of methyl orange dye onto mesoporous carbon material–kinetic and thermodynamic studies, J. Colloid Interface Sci. 362 (2011) 457–462.

Rutherford, S. W., Do, D. D., Adsorption dynamics measured by permeation and batch adsorption methods, Chem. Eng. Sci. 76 (2000a) 23-31.

Rutherford, S. W., Do, D. D., Adsorption dynamics of carbon dioxide on a carbon molecular sieve 5A, Carbon 38 (2000b) 1339-1350.

Teo, H. W. J., Chakraborty, A., Kitagawa, Y., Kayal, S., Experimental study of isotherms and kinetics for adsorption of water on Aluminium Fumarate, Int. J. Heat Mass Transf. 114 (2017) 621-627.

Wang, K., Li, C., San, H., Do, D. D., The importance of finite adsorption kinetics in the sorption of hydrocarbon gases onto a nutshell-derived activated carbon, Chem. Eng. Sci. 62 (2007) 6836-6842.

Xia, P., Wang, X., Wang, X., Song, J., Wang, H., Zhang, J., Zhao, J., Struvite crystallization combined adsorption of phosphate and ammonium from aqueous solutions by mesoporous MgO-loaded diatomite, Colloids Surf. A Physicochem. Eng. Asp. 506 (2016) 220–227.

Yang, X., Yi., H., Tang, X., Zhao, S., Yang, Z., Ma, Y., Feng, T., Cui, X., Behaviors and kinetics of toluene adsorption-desorption in activated carbons with varying pore structure, Journal of Environmental Sciences 67 (2018) 104-114.

Zhou, S., Sheng, W., Wang, Z., Yao, W., Huang, H., Wei, Y., Li, R., Quick image analysis of concrete pore structure based on deep learning, Constr Build Mater 208 (2019) 144-157.

ACKNOWLEDGMENT

I would like to express my deepest appreciation and gratitude to my supervisor **Professor Takahiko Miyazaki** for his guidance, helps, encouragement and invaluable suggestions during my study. His advice and continuous discussion are truly helpful for me, so I could complete my study. A lot of new information regarding adsorption system is difficult to gain without his involvement. I also indebted to **Professor Kyaw Thu** for his valuable assistance, encouragement, and guidance in my research.

The kind attention of reviewers, **Professor Takahiko Miyazaki**, **Professor Kyaw Thu**, **Professor Aya Hagishima**, **Professor Keishi Kariya** in taking time to examine the manuscript in spite of busy academic schedules is appreciated

My deep gratitude and appreciation go to **Professor Agung Tri Wijayanta** for his assistance during my study, valuable comments in many discussions, also constructive suggestion and criticisms, which help to improve the manuscript. **Dr. Nobuo Takata** is appreciated for his help and enthusiasm.

I should sincerely acknowledge the Ministry of Research, Technology, and Higher Education (RISTEKDIKTI) and the Ministry of Finance, Indonesia Endowment Fund for Education (LPDP) of the Republic of Indonesia, for their support of this study within the framework of BUDI-LN.

Thanks are due to all lab members, for their help and time for discussion.

Finally, I would like to express my wholehearted thanks to my family for the generous support they provided me throughout my entire life particularly through the process of my study. Thanks to my parents who have always loved me unconditionally and whose good examples have thought me to work hard for the things that I aspire to achieve.

Indri Yaningsih